Surv Geophys
DOI 10.1007/s10712-014-9304-0

A Review of the Principles and Applications of the NMR Technique for Near-Surface Characterization

Ahmad A. Behroozmand · Kristina Keating · Esben Auken

Received: 13 February 2014 / Accepted: 17 August 2014

Abstract This paper presents a comprehensive review of the recent advances in nuclear magnetic resonance (NMR) measurements for near-surface characterization using laboratory, borehole, and field technologies. During the last decade, NMR has become increasingly popular in near-surface geophysics due to substantial improvements in instrumentation, data processing, forward modeling, inversion, and measurement techniques. This paper starts with a description of the principal theory and applications of NMR. It presents a basic overview of near-surface NMR theory in terms of its physical background and discusses how NMR relaxation times are related to different relaxation processes occurring in porous media. As a next step, the recent and seminal near-surface NMR developments at each scale are discussed, and the limitations and challenges of the measurement are examined. To represent the growth of applications of near-surface NMR, case studies in a variety of different near-surface environments are reviewed and, as examples, two recent case studies are discussed in detail. Finally, this review demonstrates that there is a need for continued research in near-surface NMR and highlights necessary directions for future research. These recommendations include improving the signal-to-noise ratio, reducing the effective measurement dead time, and improving production rate of surface NMR (SNMR), reducing the minimum echo time of borehole NMR (BNMR) measurements, improving petrophysical NMR models of hydraulic conductivity and vadose zone parameters, and understanding the scale dependency of NMR properties.

A. A. Behroozmand (✉) · E. Auken
Department of Geoscience, Aarhus University, Aarhus, Denmark
e-mail: ahmad@geo.au.dk

E. Auken
e-mail: esben.auken@geo.au.dk

A. A. Behroozmand
Department of Geophysics, Stanford University, Stanford, California, USA

K. Keating
Department of Earth and Environmental Sciences, Rutgers University, Newark, NJ, USA
e-mail: kmkeat@andromeda.rutgers.edu

Published online: 07 September 2014

Keywords Nuclear magnetic resonance · NMR · Near surface

1 Introduction

Hydrogeophysical methods supply cost-effective and dense spatial information about groundwater systems when compared with direct hydrogeological characterization, i.e., drilling. Surface-based geophysical methods, such as electrical and electromagnetic (EM) techniques, have improved significantly in the past few decades and have been used to noninvasively determine aquifer properties and to improve hydrogeological models (e.g., Auken et al. 2006; Everett 2012; Slater 2007). However, such methods are limited and their interpretation is non-unique as they are only indirectly sensitive to the hydrogeological parameters of interest, e.g., water content, hydraulic conductivity, transmissivity and porosity. In the last couple of decades, nuclear magnetic resonance (NMR) has emerged as a promising method for characterizing groundwater systems as it is the only geophysical method that provides a direct estimate of the formation water content and pore structure. The goal of this paper is to present a comprehensive review of the recent advances in the technological developments and interpretation of NMR measurements for characterizing groundwater systems in the upper 100 m of the subsurface, which is referred to here as the near surface.

NMR is used in medical and chemical sciences and, to a lesser extent, in geophysics. In medicine, the NMR phenomena are used in magnetic resonance imaging (MRI) to image human tissue. In chemistry, NMR spectroscopy is used intensively to obtain information about the structure and chemical environment of molecules. In geophysics, NMR is applied as surface NMR (SNMR), borehole NMR (BNMR), and laboratory NMR (lab-NMR). SNMR is a noninvasive surface-based method that is used to determine subsurface water content and to estimate the hydraulic conductivity, K, of aquifer materials (e.g., Hertrich 2008; Legchenko et al. 2002; Meju et al. 2002; Yaramanci et al. 1999). Although the SNMR measurement has been around since the 1980s (e.g., Semenov 1987), it has only garnered popularity in the last decade due to significant advances in instrumentation and noise cancelation techniques (e.g., Dalgaard et al. 2012; Larsen et al. 2014; Müller-Petke and Costabel 2014; Walsh 2008), as well as improvements in modeling, inversion and measurement techniques (e.g., Behroozmand et al. 2012a; Grunewald et al. 2014; Irons et al. 2012; Müller-Petke and Yaramanci 2010b; Walbrecker et al. 2011b). The water content and the relaxation time are determined from SNMR data; empirical relations allow these parameters to be used to derive information about the pore structure and hydraulic conductivity of the formation. BNMR is traditionally used in the petroleum industry to detect water and hydrocarbon content and to estimate reservoir porosity and permeability (e.g., Kleinberg et al. 1994). However, the BNMR tools developed for petroleum exploration were of limited use in near-surface environments because the large diameter of the probes prevented them from being used in the much smaller diameter boreholes common in groundwater extraction and monitoring holes. Recently, a new set of slimline BNMR tools, with diameters ranging from 4.1 to 14 cm, have been developed (Sucre et al. 2011; Walsh et al. 2013); recent studies have shown that the measurements from the slimline instruments compare well with petroleum BNMR tools and can be used to detect water content and estimate hydraulic conductivity in aquifers (e.g., Dlubac et al. 2013; Knight et al. 2012). Lab-NMR is used to determine NMR properties of materials and to develop novel applications of NMR such as determining important vadose zone information including the water retention curve (e.g., Costabel and Yaramanci 2011a, b) and mobile and immobile porosity (Swanson et al. 2012).

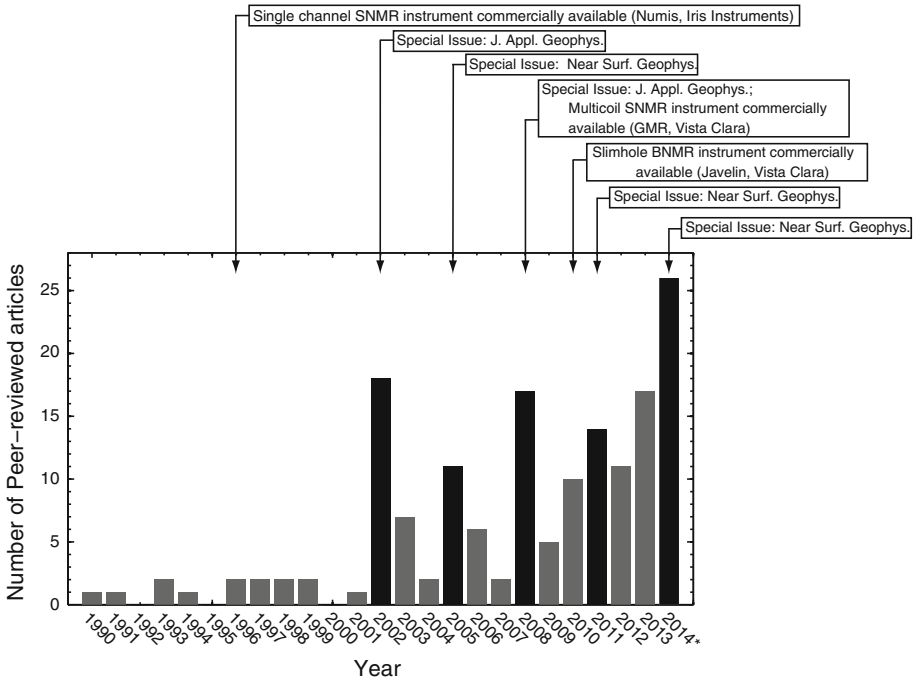

Fig. 1 List of significant events related to near-surface NMR and the number of articles published each year from 1990 to 2014 in the peer-reviewed journals, *Geophysics*, *Journal of Applied Geophysics*, *Water Resources Research*, *Near Surface Geophysics*, *Exploration Geophysics*, *Groundwater*, *Geophysical Research Letters*, *Journal of Hydrology*, *Geophysical Journal International* and *Vadose zone Journal*. The *bars* in *black* indicate years when special issue journals were published. *2014 only includes articles published as of August

The number of articles related to near-surface NMR geophysics published each year over the last 25 years provides evidence of the increasing popularity of SNMR, BNMR, and lab-NMR in near-surface geophysics. Figure 1 illustrates the number of articles on SNMR, BNMR, and lab-NMR that have been published in various peer-reviewed journals related to hydrogeology and near-surface geophysics since 1990. As can be seen in this figure, there are large spikes in the number of publications in 2002, 2005, 2008, 2011, and 2014 due to special issues on near-surface NMR published in the *Journal of Applied Geophysics* and in *Near Surface Geophysics*.

NMR studies have been presented at various international conferences and workshops, most notably the International MRS Workshop, which has been held every 3 years since it began in 1999 (Berlin 1999, Orleans 2003, Madrid 2006, Grenoble 2009 and Hannover 2012; the next workshop is scheduled to be held in Aarhus in 2015). Prior to 2012, the initials MRS in the workshop name stood for 'Magnetic Resonance Sounding' and the presentations were primarily focused on SNMR studies; in 2012, the name was changed to 'Magnetic Resonance in the Subsurface,' to reflect a shift to more general content and the workshop now includes lab-NMR and BNMR studies. The above-mentioned special issue journals were published following each of these workshops.

Despite the increasing popularity of the NMR method, to the best of our knowledge, there are no comprehensive review articles covering the near-surface geophysical applications of NMR technologies at multiple scales, specifically the surface, borehole, and

laboratory scales. These topics were briefly addressed in a recent perspective of magnetic resonance in porous media (Song 2013). A number of articles and textbooks focusing on petroleum applications of NMR have reviewed lab-NMR and/or BNMR (e.g., Coates et al. 1999; Allen et al. 2000; Dunn et al. 2002b; Kleinberg and Jackson 2001). Similarly, two articles have reviewed the SNMR method (Hertrich 2008; Legchenko and Valla 2002). Breakthrough developments that have been published during the past few years including laboratory and borehole studies, instrument developments, processing and inversion schemes, and hydrological parameter determination make this a critical time for a comprehensive review paper.

In addition to a description of NMR properties and measurements at multiple scales, this paper brings together and describes the most notable near-surface NMR advances obtained in the last decade. First, the basic theory of NMR in porous media is presented. Next, numerous studies and concepts relating to lab-NMR, BNMR, and SNMR measurements are reviewed. Finally, two case studies are presented and key aspects for future research activities are highlighted.

2 Theory

In this section, a basic overview of NMR theory as it relates to near-surface NMR measurements is presented. For a comprehensive theoretical discussion, the reader is directed to one of the many textbooks dedicated to NMR theory (e.g., Coates et al. 1999; Dunn et al. 2002b; Levitt 2006).

The physical property used in near-surface geophysics applications of NMR is the spin of the hydrogen protons in water molecules. The magnetic spin is an intrinsic property of an atom that possesses an angular momentum, without physically rotating, and an associated magnetic moment. When the magnetic moments of the hydrogen protons are situated within a static magnetic field ($\boldsymbol{B}_0$), they precess about the static magnetic field at the Larmor frequency $f_{\mathrm{L}} = \frac{\omega_{\mathrm{L}}}{2\pi} = \frac{-\gamma|\boldsymbol{B}_0|}{2\pi}$ where $\gamma = 0.2675 \times 10^9\ \mathrm{s}^{-1}\ \mathrm{T}^{-1}$ is the proton gyromagnetic ratio and ω_{L} denotes the Larmor angular frequency. The Larmor frequency depends on the static field strength, which ranges over multiple orders of magnitude for geophysical NMR measurements. For SNMR measurements, the static field is Earth's magnetic field ($\boldsymbol{B}_{\mathrm{E}}$), which ranges from about 25 to 65 μT, corresponding to Larmor frequencies ranging from about 1.06 to 2.8 kHz (Earth's magnetic field and its implications for SNMR measurements are discussed in more detail in Sect. 5.2.1). For BNMR, the static field is generated by the instrument and the field strength ranges from 5.75 to 47 mT corresponding to Larmor frequencies ranging from 0.245 to 2 MHz. Geophysical lab-NMR studies use instruments with a large range of magnetic field strengths. Measurements can be collected using Earth's magnetic field or using instruments with fields strengths up to ~9.4 T; this corresponds to Larmor frequencies on the order of kHz to ~400 MHz.

At thermal equilibrium in the static magnetic field, the volume of water in the measured sample acquires a small net magnetic moment. This moment is the sum of all the magnetic moments associated with each of the protons in the volume and points in the same direction as the static magnetic field. The net magnetization vector at thermal equilibrium is given by (Curie's law)

$$\boldsymbol{M}_0 = \frac{n\gamma^2\hbar^2}{4K_{\mathrm{B}}T}\boldsymbol{B}_0. \tag{1}$$

Here, n is the number of protons per unit volume; γ is again the proton gyromagnetic ratio; $\hbar$ is the reduced Plank's constant; T is the temperature; and K_B is Boltzmann's constant.

The NMR experiment begins when the protons, initially at thermal equilibrium, are perturbed by an energizing pulse tuned to the Larmor frequency. If this pulse is applied and then removed, the protons move away from and then relax back to thermal equilibrium. As the protons relax, they emit a measurable signal. In porous media, NMR relaxation is well described by the phenomenological Bloch–Torrey equations (Bloch 1946; Torrey 1956). The solution to the Bloch–Torrey equations is a multiple exponential (multi-exponential) decay in the transverse direction with respect to the direction of the static magnetic field, i.e., the xy-plane, and multi-exponential growth in the longitudinal direction, i.e., the z-plane (Brownstein and Tarr 1979)

$$\begin{aligned} E_{xy}(t) &= E_0 \sum_i f_{2i} \mathrm{e}^{-\frac{t}{T_{2i}}} \\ E_z(t) &= E_0 \left(1 - \sum_i f_{1i} \mathrm{e}^{-t/T_{1i}} \right). \end{aligned} \tag{2}$$

Here, $E_{xy}(t)$ and $E_z(t)$ are the transverse and longitudinal components of the NMR signal; E_0 is the initial signal magnitude and is proportional to the number of protons or volume of water in the measured sample. f_{2i} is the proportion of the magnetic field relaxing in the transverse direction with relaxation time T_{2i}, and similarly, f_{1i} is the proportion of the magnetic field relaxing in the longitudinal direction with relaxation time T_{1i}. The values of T_{2i} are often plotted versus f_{2i} to yield the transverse relaxation time distribution or T_2-distribution; similarly, the values of T_{1i} are plotted versus f_{1i} to yield the longitudinal relaxation time distribution or T_1-distribution. Typically, and for Eq. (2), the longitudinal direction is defined to be in the same direction as $\boldsymbol{B}_0$ and the solution is taken from the so-called 'rotating laboratory' reference frame that is from the perspective of a laboratory rotating at the Larmor frequency.

For NMR relaxation in fluid-saturated geologic material, it is often assumed that relaxation occurs in the fast-diffusion, or surface-limited, regime and that there is little or no pore coupling (Brownstein and Tarr 1979; Grunewald and Knight 2009; Senturia and Robinson 1970). The fast diffusion regime is satisfied when the control parameter, κ, is much less than one (Brownstein and Tarr 1979)

$$\kappa = \frac{\rho_{1,2} a}{D}. \tag{3}$$

In this equation, $\rho_{1,2}$ is the surface relaxivity and is a measure of the ability of a pore surface to enhance relaxation. The subscript 1 implies longitudinal relaxation and the subscript 2 implies transverse relaxation. a is the average distance a proton travels before encountering a paramagnetic site, and D is the self-diffusion coefficient of water ($D = 2.46 \times 10^{-9}$ m^2/s at 30° C; Simpson and Carr 1958). The fast-diffusion regime can be thought of as the regime in which a proton can move to and interact with the surface of a pore within the time scale of the NMR measurement. Ryu (2009) suggested that a sufficient condition for fast diffusion is $\kappa < 0.1$.

The assumption that there is no pore coupling is satisfied when the average pore size is greater than the diffusion length scale, ℓ, which is defined by the Einstein equation for self-diffusion

$$\ell = \sqrt{6DT}, \tag{4}$$

where T is the time scale of the NMR experiment. Under these two assumptions, each exponent in Eq. (2) corresponds to a single pore and information about the pore sizes or pore surface geochemistry can be extracted from the T_2- or T_1-distribution (e.g., Arns 2004; Keating et al. 2008). In the interpretation of NMR data for petroleum, hydrogeological, and environmental applications, relaxation is typically assumed to occur in the fast diffusion regime with little to no pore coupling. The impact of violating the fast diffusion regime assumption and the impact of pore coupling on the NMR response of geologic material are discussed in Sect. 3.3.

To obtain the values of E_0, $f_{1,2i}$, and $T_{1,2i}$, the multi-exponential signal from Eq. (2) is inverted. Although the equation for the multi-exponential signal may appear simple, it is an ill-posed problem indicating that the solution is non-unique and/or may not exist. As such, there is a large body of the literature dedicated to the accurate inversion of multi-exponential data (e.g., Istratov and Vyvenko 1999; Whittall et al. 1991). In lab-NMR studies relevant for near-surface geophysics investigations, there are three main approaches that are used to invert multi-exponential data. The first approach is nonnegative least squares (NNLS). In the NNLS algorithm, the multi-exponential signal is linearized and fit to a set of pre-defined relaxation times, while a positivity constraint is applied to the signal amplitude associated with each relaxation time (see Whittall and MacKay 1989 for details). Typically, Tikonov regularization is used to yield a smooth distribution of relaxation times. The advantage of the NNLS approach is that it does not assume a number of relaxation times that fit the data (Whittall et al. 1991). When the NNLS approach is used, an average relaxation time, calculated from the geometric mean, is often used to represent the relaxation time distribution. In the second approach, a specified number of exponential decays are used to fit the data. Typically, 2–4 decays are found to be sufficient to represent the multi-exponential decay (see Kenyon et al. 1988 for details). The third approach is the stretched-exponential fit. In this case, the multi-exponential decay can be fit with a stretched exponential under the assumption that the summations in Eq. (2) can be described by $e^{-\left(\frac{t}{T_{1,2}}\right)^c}$, where c is the stretching exponent that describes the spread of the distribution and $T_{1,2}$ is the average relaxation time of the distribution (see Kenyon et al. 1988 for details). The advantage of the stretched-exponential approach is that it requires fewer parameters to fit the data and is thus a faster and more robust algorithm. However, while the stretched exponential works well for material with a single peak or two overlapping peaks in the distribution, it breaks down when there is a bimodal pore-size distributions with narrow peaks separated by two or more orders of magnitude and must be modified in such cases (Apitz and Johansen 2005; Peyron et al. 1996).

2.1 Transverse Relaxation Times, T_2^* and T_2

The simplest NMR experiment consists of applying a time-varying energizing magnetic field oscillating at the Larmor frequency, $\boldsymbol{B}_1(t)$, for a short duration, τ_p. In a macroscopic sense, applying this energizing pulse causes the magnetization vector to tip away from the longitudinal direction; the angle to which the magnetization is moved away from the z-axis is called the tip angle. The tip angle is varied by changing the duration of time and/or current intensity for which the energizing pulse is applied. When a single pulse is applied with a tip angle of 90°, then the experiment is called a free induction decay (FID). Although FIDs are not commonly used in lab-NMR or BNMR measurements, the FID is the most common measurement collected when using SNMR equipment (e.g., Hertrich 2008). The pulse sequence for an FID is given in Fig. 2a.

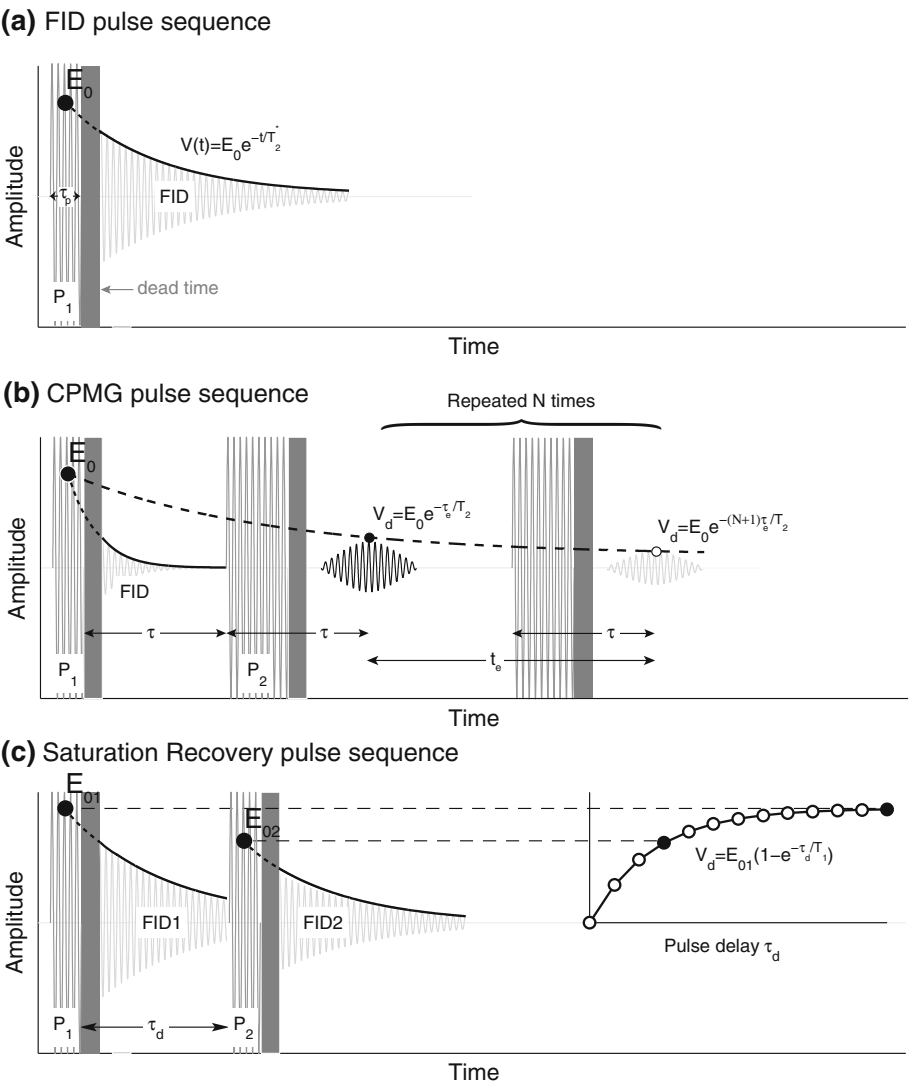

Fig. 2 NMR pulse sequences. **a** FID pulse sequence: the single 90° energizing pulse P_1 is emitted at the local Larmor frequency. After P_1 is switched off and a measurement dead time (*shaded gray box*) has elapsed, a single FID, ideally oscillating at the same frequency as P_1, is recorded. Subsequently, envelope detection of the FID provides the effective transverse relaxation time T_2^* and initial amplitude E_0. In SNMR measurements, the latter is obtained by extrapolating the signal back to the initial time, i.e., $\tau_p/2$. **b** CPMG pulse sequence: the measurement begins with the application of a 90° pulse as in (**a**); a train of N of refocusing pulses P_2, separated by the echo time $t_e = 2\tau$ each with $\tau_{P2} = 2\tau_{P1}$, are applied at a time τ after P_1 with echoes appearing half way between every refocusing pulse. The T_2 exponential decay (*dashed curve*) is formed from the peaks of each of the echoes. The spin echo pulse sequence (not shown here) consists of the first two pulses of the CPMG pulse sequence and can be applied for a series of P_1 and P_2 with different τ to obtain the T_2 decay curve. **c** Saturation recovery pulse sequence: the measurement begins with a single 90° energizing pulse P_1, which has a corresponding FID (FID1). After a delay time, τ_d, a second pulse 90° P_2, is applied and the corresponding FID curve (FID2) is recorded. This sequence is repeated for different delay times, and the initial amplitude of FID2, E_{02}, builds the T_1 recovery curve. **a** and **c** are modified from Hertrich (2008)

As shown in the gray region of Fig. 2a, there is a nonzero time between the end of the energizing pulse and the beginning of the measurement that Walsh et al. (2011) referred to as the "measurement dead time." The nonzero measurement dead time is due to the fact that, once turned off, the excitation field does not decay to zero instantaneously and the signal cannot be recorded until the excitation field has fully decayed. The measurement dead time is caused by induction effects; existing SNMR instruments have measurement dead times of less than or equal to 5 ms for the GMR and 20 ms for the NUMIS system. As the inductive response in moderate to resistive terrains are negligible after a few microseconds, the long dead times are due to instrument limitations. In addition, data processing and inversion techniques can increase the dead time, t_{dead}, leading to a longer "effective dead time" (Dlugosch et al. 2011; Walsh et al. 2011).

The FID is very sensitive to inhomogeneities in the magnetic field caused by large-scale variations in Earth's magnetic field due to magnetic anomalies or small, pore-scale variations due to differences in the magnetic susceptibility between the pore water and the solid-phase material. The presence of magnetic field inhomogeneities enhances the relaxation time. Due to this enhanced relaxation, the effective transverse relaxation time associated with an FID is less than or equal to both T_2 and T_1 and is denoted by T_2^*. In the absence of magnetic field inhomogeneities, T_2 is theoretically equivalent to T_2^*; however, it is rarely the case that the static field is homogeneous. In the presence of magnetic field inhomogeneities, T_2^* is described by three relaxation processes occurring in parallel

$$\frac{1}{T_2^*} = \frac{1}{T_{2\text{B}}} + \frac{1}{T_{2\text{S}}} + \frac{1}{T_{2\text{IH}}}, \tag{5}$$

where $T_{2\text{B}}$ is the transverse bulk fluid relaxation time, $T_{2\text{S}}$ is the transverse surface relaxation time, and $T_{2\text{IH}}$ is the inhomogeneous field dephasing relaxation time and accounts for relaxation in an inhomogeneous magnetic field (Grunewald and Knight 2011b). In Eq. (5), T_2^* is an average value either determined from the mean log average from the relaxation time distribution, a single relaxation time fit to the distribution, or the single relaxation time determined from the stretched-exponential fit.

Due to the effect of magnetic field inhomogeneities, the value of T_2 cannot be determined from an FID. Therefore, T_2 is typically measured with the spin echo pulse sequence or the Carr–Purcell–Meiboom–Gill (CPMG) pulse sequence (Carr and Purcell 1954; Hahn 1950; Meiboom and Gill 1958). The CPMG pulse sequence requires less measurement time than the spin echo pulse sequence and is the most common pulse sequence used to collect near-surface BNMR data. Both pulse sequences were developed to reduce the effect of magnetic field inhomogeneities on the NMR signal. The CPMG pulse sequence is depicted in Fig. 2b. Both pulse sequences start with the application of a 90° pulse followed by a 180° pulse. After the 90° pulse, the spins dephase according to their local magnetic field environment and the NMR signal relaxes as a standard FID with a relaxation rate of T_2^*. The 180° pulse, applied at a time τ after the 90° pulse, acts to refocus the dephased spins, and a so-called echo appears at a time τ following the 180° pulse; this double-pulse sequence is the spin echo pulse sequence. To obtain the T_2 exponential decay curve using the spin echo pulse sequence, a series of 90° and 180° pulses with different separation times, τ, is applied. To apply a CPMG pulse sequence, a train of N 180° pulses separated by the echo time, $t_{\text{e}} = 2\tau$, are applied following the first 180° pulse to refocus the spins with echoes appearing halfway between each of the pulses. The distribution of T_2 values are then determined from the exponential decay formed from the peaks of each of the echoes.

Although the CPMG and spin echo pulse sequences were designed to rephase the spins in the presence of inhomogeneous magnetic fields, due to the self-diffusion of spins in a

liquid, the spins cannot be perfectly rephased. In an inhomogeneous magnetic field, the value for T_2 is, as with T_2^*, described by three relaxation processes occurring in parallel

$$\frac{1}{T_2} = \frac{1}{T_{2B}} + \frac{1}{T_{2S}} + \frac{1}{T_{2D}}. \tag{6}$$

Here, as in Eq. (5), the value of T_2 in Eq. (6) is an average value either determined from the mean log average from the relaxation time distribution, a single relaxation time fit to the distribution, or the single relaxation time determined from the stretched- exponential fit. T_{2B} and T_{2S} are, as previously defined, the transverse bulk fluid and surface relaxation times. The third term in Eq. (6), T_{2D}, is the diffusion relaxation time and accounts for transverse relaxation in an inhomogeneous magnetic field.

The magnitude of the bulk fluid relaxation time, T_{2B} in Eqs. (5) and (6), depends on the properties of the saturating fluid including the viscosity, the concentration of dissolved paramagnetic species, i.e., species with an unpaired electron such as, dissolved oxygen, aqueous manganese(II) or aqueous iron(III), and pH (Bloembergen et al. 1948; Bryar et al. 2000). Typically, it is assumed that T_{2B} is long compared with T_{2S}, T_{2IH}, and T_{2D}, and so its contribution to the overall relaxation time is often neglected. In aquifers, the value of T_{2B} is expected to range from 1.1 to 3.4 s (Dlubac et al. 2014; Stork et al. 2006). The mechanisms contributing to T_{2S}, T_{2IH}, and T_{2D} will be discussed in detail in Sect. 3.

2.2 Longitudinal Relaxation Time, T_1

Since the magnetization cannot be measured in the longitudinal direction, it must be measured in the transverse direction. The two pulse sequences that are typically used to determine T_1, called the inversion recovery pulse sequence and the saturation recovery pulse sequence, consist of an initial pulse that rotates the magnetization and then a second pulse that rotates the magnetization component that has recovered in the *z*-plane into the *xy*-plane to be measured. Although both pulse sequences are common in lab-NMR, the saturation recovery pulse sequence is most relevant for SNMR data and the discussion here is focused on this pulse sequence; for more information about the inversion recovery pulse sequence and other laboratory pulse sequences not covered in this review, the reader is directed to any standard NMR textbook (e.g., Levitt 2006; Nishimura 2010). The saturation recovery pulse sequence consists of applying two 90° pulses separated by a delay time of τ_d, as depicted in Fig. 2c. Once the system has returned to thermal equilibrium, i.e., a recovery time greater than or equal to $3T_1$ has elapsed, the sequence is repeated with a new τ_d. By recording the initial magnitude of the FID following the second 90° pulse (E_{02} in Fig. 2c), the exponential recovery, characterized by T_1, is determined. Because the system needs to return to equilibrium between each set of pulses, determining T_1 requires much longer measurement times than determining T_2 using the CPMG pulse sequence. However, the advantage of T_1 measurements is that they are not affected by inhomogeneities in the magnetic field. T_1 is described by

$$\frac{1}{T_1} = \frac{1}{T_{1B}} + \frac{1}{T_{1S}}, \tag{7}$$

where T_{1B} and T_{1S} are the longitudinal bulk and surface relaxation times. Because there is no diffusion relaxation term in Eq. (7), there is a large focus on developing a pulse sequence that can be used to determine T_1 using SNMR instrumentation (e.g., Legchenko et al. 2004; Müller-Petke et al. 2013; Walbrecker et al. 2011b; Walbrecker and Behroozmand 2012).

3 Laboratory Nuclear Magnetic Resonance (Lab-NMR) and Petrophysical Relations

Laboratory NMR is commonly used in the petroleum industry to evaluate rock cores and to develop petrophysical relations between NMR parameters and parameters of interest for petroleum exploration (e.g., Seevers 1966; Timur 1969). Until recently, it was assumed that the petrophysical relations developed in the petroleum industry could be directly applied to the interpretation of near-surface measurements. In particular, many early studies assumed that T_2^* measured in Earth's magnetic field was approximately equal to T_2 measured in lab-NMR systems (e.g., Mohnke and Yaramanci 2008; Müller et al. 2005); however, recent laboratory studies have shown that these values are equal only under specific conditions (e.g., Grunewald and Knight 2011b). In particular, the presence of magnetic minerals and clay content, which are commonly found in near-surface sediments, can enhance T_2^* relaxation (Grunewald and Knight 2011b; Roy and Lubczynski 2005). Additionally, recent laboratory experiments have focused on expanding the applications of near-surface NMR geophysics to include vadose zone measurements (e.g., Costabel and Yaramanci 2011a, b) and to monitor mineralogic transformations associated with contaminant remediation (e.g., Keating et al. 2008). Although the body of the literature focused on lab-NMR measurements and petrophysical relations is vast, this section primarily focuses on the lab-NMR literature relevant for near-surface applications and only highlights some of the seminal papers from the petroleum literature. For a comprehensive overview of NMR petrophysical relations related to petroleum applications, the reader is directed to Dunn et al. (2002b).

3.1 NMR-Determined Water Content

The strength of the NMR measurement in geophysics, both for near-surface and petroleum applications, stems from the fact that the initial signal amplitude [i.e., E_0 in Eq. (2)] is proportional to the number of protons in the measured sample (e.g., Coates et al. 1999). This in turn means that E_0 is proportional to the volume of water in the measured sample, V_w. Figure 3 clearly shows that this relation holds for bulk water (measurements collected at 2 MHz). Therefore, using an instrument-specific calibration factor, an NMR-estimated water volume can be determined from E_0, to distinguish the NMR-estimated water volume from the true volume of water in the sample; this value is referred to as V_{NMR}. Using V_{NMR} and the volume of the measured sample, V_s, the NMR-estimated water content, θ_{NMR} can be determined from

$$\theta_{NMR} = \frac{V_{NMR}}{V_S}. \tag{8}$$

In saturated geologic media and where there is no signal loss (i.e., $V_{NMR} = V_w$), then $\theta_{NMR} = \phi$ where ϕ is the porosity. Although V_{NMR} should theoretically equal V_w, under certain circumstances, V_{NMR} can overestimate V_w, for example in Earth's field FID measurements with high magnetic field inhomogeneities and non-exponential decay (details in Sect. 3.5) or when the pores are saturated with a mixture of two hydrogen-bearing fluids (see e.g., Hedberg et al. 1993), or underestimate V_w, for example in measurements where there is significant decay during the pulse (details in Sect. 5.4). Additionally, in measurements with a low signal-to-noise ratio, the error associated with the NMR-estimated water content can be very high.

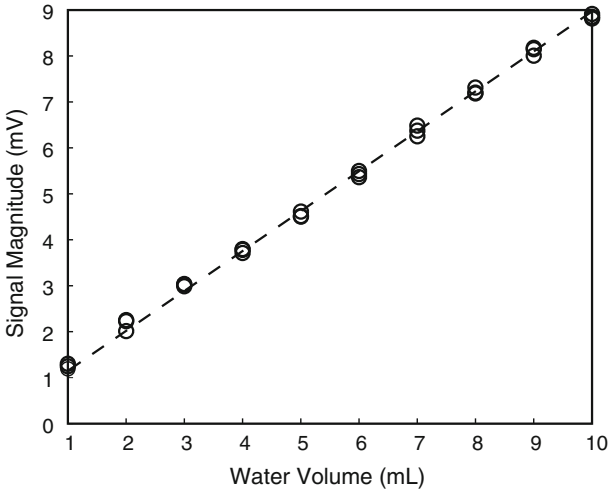

Fig. 3 Calibration curve for a laboratory-NMR instrument showing the linear relation between the NMR signal, E_0, and water volume, V_w. Data were collected on deionized water at 2 MHz

3.2 NMR-Estimated Pore-Size Distributions

As discussed in Sect. 2, in most geologic applications of NMR, it is typically assumed that relaxation occurs in the fast diffusion regime and that there is limited pore coupling. Under these conditions, each pore contributes separately to the overall relaxation time distribution and the surface relaxation time in a single pore is given by (Brownstein and Tarr 1979; Godefroy et al. 2001)

$$\frac{1}{T_{1,2S}} = \rho_{1,2}\frac{\alpha}{r} = \rho_{1,2}S_{por}, \tag{9}$$

where the subscripts 1 and 2 indicate longitudinal and transverse relaxation time, respectively, α is a shape factor accounting for the geometry of the pore ($\alpha = 1$ for planar pores, 2 for cylindrical pores, and 3 for spherical pores), and r is the characteristic size of the pore (i.e., the distance between two planes for planar pores or the radius of a cylindrical or spherical pore). In Eq. (9), S_{por} is the surface area-to-volume ratio of the pore and is equivalent to α/r for ideal pore shapes. It is also assumed that the bulk fluid relaxation time is negligible, and for transverse relaxation, magnetic field inhomogeneities are negligible, i.e., T_{2D} and/or T_{2IH} are equal to zero, then $T_{1,2} \cong T_{1,2S}$.

Under the assumptions that $T_{1,2} \cong T_{1,2S}$ and that the surface relaxivity is constant, it can be seen that the distribution of relaxation times is linearly proportional to the pore-size distribution (e.g., Hinedi et al. 1993). That is, short relaxation times correspond to small pores and long relaxation times correspond to large pores. Figure 4 shows a set of idealized relaxation time distributions and the corresponding pore sizes. These assumptions are generally true for materials with low surface relaxivities and/or small pores, and there is a large body of the literature comparing the T_1- and/or T_2-distributions to the pore-size distribution for a range of water-saturated porous media. Examples of material where the pore (or grain) size distributions compare favorably with the NMR relaxation time distribution include measurements on: sandstone and carbonate rocks (Arns 2004; Straley et al. 1997); mixtures of sands and clays (Stingaciu et al. 2009); silica gels (Valckenborg et al. 2001); fused glass beads (Straley et al. 1987); and unconsolidated sands and glass beads (Bird et al. 2005; Hinedi et al. 1997). The relation between the T_2-distribution and

the pore-size distribution has also led to recent interest in using NMR measurements to estimate parameters affecting contaminant transport, i.e., the mobile and immobile porosity (Swanson et al. 2012), and parameters governing the flow of water in the unsaturated zone, i.e., the characteristic water retention curve (additional details provided in Sect. 3.4, Bird et al. 2005; Costabel and Yaramanci 2011a, b).

When a single relaxation time value, determined from the average relaxation time, the stretched exponential, or a single exponential fit, is used, then r in Eq. (9) represents the average pore size of the measured sample and S_{por} represents the total value taken over the entire pore space. Since S_{por} is related to the permeability or hydraulic conductivity by Kozeny–Carman type relations, Eq. (9) has allowed geophysical NMR measurements to be used to estimate the hydraulic conductivity. NMR estimates of the hydraulic conductivity will be discussed in detail in Sect. 3.4.

The values of T_1, T_2, and T_2^* of water-saturated material relevant for geologic applications range from $\sim$1 ms for samples containing magnetic minerals to >1 s for clean quartz sands (Keating and Knight 2007; Yaramanci et al. 1999). Although some water-saturated geologic materials have a relaxation time less than 1 ms, it is not always possible to measure the NMR response of such samples with very fast relaxation times due to instrument limitations such as a long dead time or long minimum echo time. The upper bound on the measured value of T_1, T_2, and T_2^* is provided by the relaxation time of bulk water.

Table 1 presents a list of relaxation times associated with natural and synthetic geologically relevant materials for a range of Larmor frequencies. In general, as can be seen from the values shown in Table 1, there is a clear dependence of T_1, T_2, and T_2^* on pore size. However, for materials with high concentrations of iron minerals, which have high associated surface relaxivities, or large magnetic susceptibilities (e.g., magnetite), the T_1, T_2, and T_2^* values do not reflect the pore size but instead reflect the paramagnetic content or magnetic field inhomogeneities.

3.3 Violating the Fast Diffusion and Limited Pore Coupling Assumptions

Although fast diffusion and limited pore coupling are often assumed in the interpretation of NMR data, for materials with large pores, such as aquifer materials, and/or large values of surface relaxivity, this assumption can be violated (Bryar et al. 2000; Vogt et al. 2002). A number of recent studies have examined the effect of violating these assumptions on NMR relaxation rates (Dlubac et al. 2014; Grunewald and Knight 2011a; Keating and Falzone 2013; Keating and Knight 2012). In this section, the theory concerning relaxation outside the fast diffusion regime and the effect of pore coupling is presented and the implications on the interpretation of NMR data are discussed.

In their analytical study, Brownstein and Tarr (1979) determined that there were three relaxation regimes in which NMR relaxation in a single pore could occur: the slow diffusion relaxation regime, the intermediate diffusion relaxation regime, and the fast diffusion relaxation regime. The fast diffusion regime is satisfied when $\kappa \ll 1$ [see Eq. (3)], and a single pore is represented by a single relaxation time. Outside the fast diffusion regime, however, the NMR signal from a single pore is no longer represented by a single exponential but is instead described by a sum of exponentials. In the slow diffusion regime, which is defined by $\kappa \gg 10$, the majority, 60–90 % depending on characteristic pore shape, of the relaxation takes place in the slowest mode or occurs with the longest relaxation time. In the intermediate diffusion regime, which is defined by$1 \ll \kappa \ll 10$, the

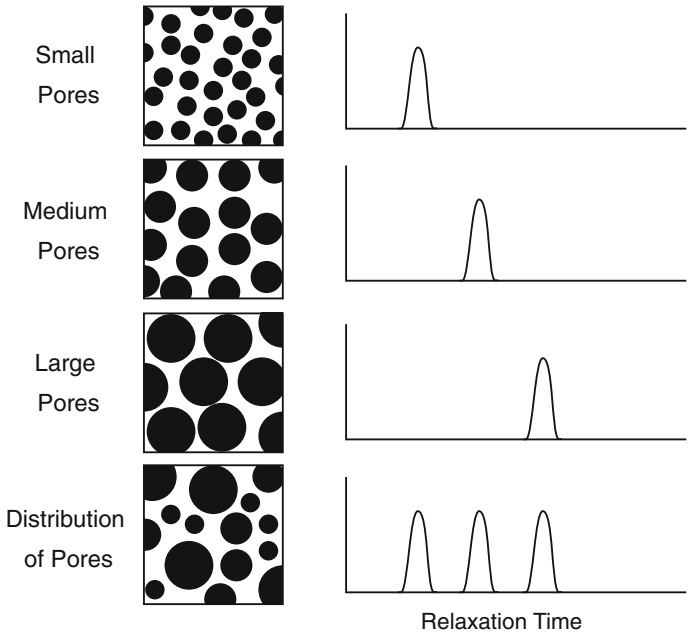

Fig. 4 Theoretical relaxation time distributions for a range of pore sizes. For the square panels, the pores are shown in *black,* whereas the solid matrix is in *white*. Figure modified from Mohnke and Yaramanci (2008)

majority of the relaxation takes place in the slowest mode with only a few percent relaxing with higher modes (Brownstein and Tarr 1979). This multi-exponential decay due to relaxation in a single pore can complicate the interpretation of NMR data.

Outside the fast diffusion regime, $T_{1,2B}$, T_{2D}, and T_{2IH} remain the same. However, $T_{1,2S}$ is no longer described by Eq. (9). The slowest mode surface relaxation time, which is denoted $T_{1,2S-0}$, is instead given by (Godefroy et al. 2001)

$$\frac{1}{T_{1,2S-0}} = \frac{1}{\frac{r}{\alpha\rho_{1,2}} + \frac{r^2}{2\alpha D}}. \tag{10}$$

In the case of slow diffusion, the second term in the denominator dominates the relaxation and $T_{1,2-0}$, simplifies to (Godefroy et al. 2001)

$$\frac{1}{T_{1,2S-0}} = \frac{2\alpha D}{r^2}. \tag{11}$$

Figure 5 shows how the slowest mode relaxation time, normalized by the slowest mode relaxation time at $\kappa = \infty$, changes as a function of κ.

The effect of violating the fast diffusion regime has implications for the relation between NMR relaxation times and the pore-size distribution as well as the NMR estimates of S_{por}. For lab-NMR measurements on near-surface sediments, it has been shown that a linear transformation of the relaxation time distribution using Eq. (9) yields a relative distribution of pore sizes but does not yield the true distribution of pore sizes as estimated from the grain sizes or mercury injection porosimetry (Hinedi et al. 1993; Keating and

Table 1 Literature values T_1, T_2, and T_2^* of synthetic and natural geologic materials for Larmor frequencies ranging from Earth's magnetic field (E.F.) to over 100 MHz. Where necessary, values were extracted from plots

Material	T_1 (ms)				T_2 (ms)[a]					T_2^* (ms)	
	250 kHz–2 MHZ	3–10 MHz	11–100 MHz	>100 MHz	E.F.	250 kHz–2 MHz	3–10 MHz	10–100 MHz	>100 MHz	E.F.	2 MHz
Water	–	1,100[9]		3,000[7]	2,030[14]	–	–	–	2,430[7]	1,300[14]	0.9[6]
Clay	4–5[6]	–	0.44–0.66[12]; 330[1]	–	–	4–6[6]	–	–	–	–	0.4–0.7[6]
Silt	13[6]	–		–	–	12–14[6]	–	–	–	–	13[6]
Fine sand (0.03–0.2 mm)	90–565[6]	100–225[9]	120–1,000[1,2,5]	200–1,053[5]	214–622[8,14]	10–1,615[2,4,6,8]	75–150[9]	–	–	140–300[8,14]	0.4–1.3[6]
Medium sand (0.2–0.63 mm)	540[6]	500[9]	500[5]	199–900[5]	310–1,100[8,14]	200–220[6,8]	225[9]	–	–	90–429[8,14]	0.7[6]
Coarses and (0.63–2.0 mm)	700–760[6]	700–1,050[9]	800[5]	1,200–2,700[5]	460–1,170[8]	300–1,100[6,8]	300–400[9]	–	–	140–280[8]	0.5–0.8[6]
Sand–clay mixtures	20–30[6]	–	–	–	–	30–55[6]	–	–	–	–	0.2–0.8[6]
Sandstone	–	13–581[15,17,18]	–	–	–	–	1.12–33[17]	–	–	–	–
Limestone	–	43–231[15]	–	–	–	2–183[16]	–	–	–	–	–
Glass beads (10–100 μm)	–	–	–	870–2,020[5,7,11]	–	–	–	–	12.5–600[7,11]	–	–
Glass beads (>100 μm–1 mm)	–	–	–	1,000–3,000[7]	–	–	–	–	100–1,600[7]	–	–
Glass beads (>1–10 mm)	–	–	–	3,000[7]	–	–	–	–	1,600[7]	–	–
Iron mineral and quartz sand mixtures (excluding magnetite)	–	–	–	–	–	4–55[3,4,13]	–	–	–	–	–
Magnetite and quartz sand mixtures[b]	–	–	–	–	–	2–300[10]	–	–	–	–	–

[1] Bryar and Knight (2002), [2] Bryar and Knight (2003), [3] Keating and Knight (2007), [4] Grunewald and Knight (2011a), [5] Vogt et al. (2002), [6] Müller et al. (2005), [7] Bray et al. (2006), [8] Costabel and Yaramanci (2011a), [9] Mitreiter et al. (2010), [10] Keating and Knight (2008), [11] Codd et al. (2011), [12] Fleury et al. (2013), [13] Foley et al. (1996), [14] Grunewald and Knight (2011b), [15] Kenyon et al. (1988), [16] Megawati et al. (2012), [17] Weller et al. (2010), [18] Sen et al. (1990)

[a] Results depend on echo time

[b] Results are strongly dependent on iron concentrations

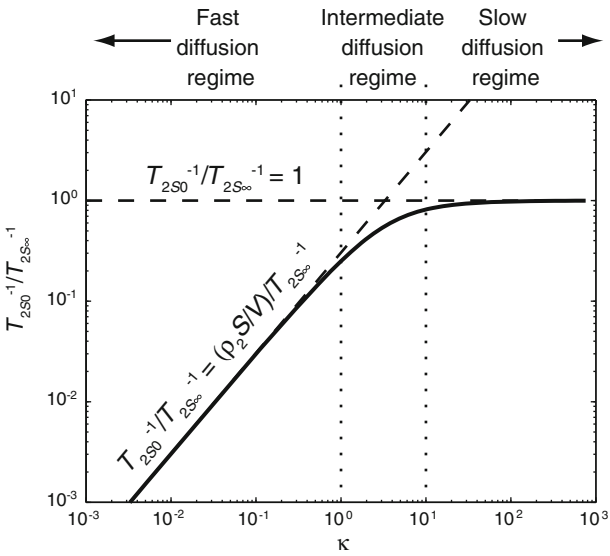

Fig. 5 Behavior of $T_{2S0}^{-1}/T_{2S\infty}^{-1}$ versus κ for the fast, intermediate and slow diffusion regimes. Figure used with permission from Keating and Knight (2012)

Falzone 2013). It has been hypothesized that the reasons for the inability of the relaxation time distribution to accurately estimate the pore-size distribution is because (1) relaxation does not occur in the fast diffusion regime or (2) the estimated value of the measured surface area (determined using Nitrogen BET) is not the same as the water-wetted surface area resulting in inaccurate estimates for the surface relaxivity. Keating and Falzone (2013) showed analytically that for materials in which relaxation occurred near the boundary or outside the fast diffusion regime, i.e., $\kappa > 0.1$, the distribution of relaxation times would be broader than the associated pore-size distribution. However, the laboratory results from Keating and Falzone (2013) did not match the theoretical results; the reason for the difference between the relaxation time distributions and the pore-size distribution is unresolved, and research in this area is ongoing.

As discussed in Sect. 2, pore coupling implies that diffusing spins can move through and sample multiple pores on the time scale of an NMR measurement. If there is pore coupling, then each element in the sum of Eq. (2) does not represent a single pore but instead represents an average across multiple pores. Using silica gels with a bimodal pore-size distribution in a study of T_2 relaxation times, Grunewald and Knight (2009) observed that the degree to which pores are coupled depends on ρ_2. When ρ_2 was lower, pore coupling was stronger and the peaks of the bimodal relaxation time distribution merged. When ρ_2 was higher, pore coupling was weaker and the peaks in the relaxation time distribution were separate. The same observations have been made for T_1 measurements (Bryar et al. 2000; Daughney et al. 2000). The link between pore coupling and surface relaxivity has been modeled analytically, and it was noted that for high surface relaxivity, the diffusion length is reduced because the enhanced relaxation limits both the time and the distance over which a diffusing proton can travel before relaxing (Ramakrishnan et al. 1999). Grunewald and Knight (2009) concluded that in unconsolidated material with well-connected pores, the NMR relaxation time distribution might not accurately represent the underlying pore structure due to pore coupling effects.

3.4 NMR-Estimated Hydraulic Conductivity

Laboratory studies linking NMR relaxation times with fluid flow properties primarily focus on estimating permeability, k, in hydrocarbon reservoirs. Traditional models for estimating k from NMR parameters are derived from capillary tube models that link k to bulk physical properties of a water-saturated porous medium using the Kozeny–Carman (K–C) relation or a variation of this relation (e.g., Seevers 1966)

$$k = \frac{\phi r_{\mathrm{h}}^2}{\alpha \tau_{\mathrm{tor}}}. \tag{12}$$

Here, ϕ is the porosity, r_{h} is the hydraulic radius, typically represented by the inverse of S_{por}, α is a geometric factor, and τ_{tor} is the tortuosity. The permeability estimates can be transformed to estimates of saturated hydraulic conductivity, K, using the conversion

$$K = k\frac{g\rho}{\mu}, \tag{13}$$

where μ is the temperature-dependent dynamic viscosity, $g = 9.8\ \mathrm{m/s^2}$ is the gravitational acceleration, and ρ is the temperature-dependent density. At 30 °C, the operating temperature of many low-field NMR laboratory instruments μ is 0.7978×10^{-3} kg/(s m) and ρ is 995.7 kg/m^3.

Although the body of the literature linking NMR relaxation measurements to k is extensive, the available models were developed for use in the analysis of petroleum reservoirs and only a limited number of studies explicitly consider near-surface sediments. Although most models were developed to estimate k, here, they are presented in terms of K as the primary application here is water resource issues.

The NMR-K models fall into two main categories: (1) Timur–Coates (T–C) models, which use the NMR-determined porosity, ϕ_{NMR}, and the ratio of free fluid to bound fluid in the measured volume to estimate K, and (2) Schlumberger Doll Research (SDR) models, which use ϕ_{NMR} and T_2 to estimate K (Coates and Dumanoir 1974; Seevers 1966; Timur 1969). Both the T–C and SDR models require that relaxation occurs in the fast diffusion regime and assume that $T_{2\mathrm{B}}$ is negligible. A recent study, however, provided evidence for the need to account for $T_{2\mathrm{B}}$ in the hydraulic conductivity estimations (Dlubac et al. 2013). SDR models are more commonly used than T–C models, but as long as the models are properly calibrated for lithology, both have been found to yield comparable estimates of k or K (e.g., Allen et al. 2000).

In the T–C K models, the ratio of free fluid to bound fluid is calculated from the ratio of the Free Fluid Index (FFI) to the Bound Fluid Index (BFI). FFI is the integral of the NMR signal with a relaxation time greater than a predefined cutoff time, calculated from $\sum_{T_2 > T_{2\mathrm{cut\,off}}} f_i$, and the BFI is the integral of the NMR signal with a relaxation time less than the cutoff time, calculated from $\sum_{T_2 < T_{2\mathrm{cut\,off}}} f_i$. For water-saturated sandstones, a 33 ms cutoff time is typically used whereas, for carbonates, the cutoff time is significantly greater (100s of milliseconds; Freedman 2006). To the best of the authors' knowledge, no research has been done on unconsolidated sediments to define an appropriate cutoff time although one recent study showed that a cutoff time of 33 ms was sufficient to distinguish between mobile and immobile pore water in zeolites (Swanson et al. 2012). T–C permeability models are of the form (Coates and Dumanoir 1974; Timur 1969)

$$K = C_{\mathrm{T-C}}\left(\frac{\mathrm{FFI}}{\mathrm{BFI}}\right)^{a_{\mathrm{T-C}}}\phi_{\mathrm{NMR}}^{b_{\mathrm{T-c}}}. \tag{14}$$

Here, $C_{\mathrm{T-C}}$, $a_{\mathrm{T-C}}$ and $b_{\mathrm{T-C}}$ are empirically derived constants; typically, $a_{\mathrm{T-C}}$ is on the order of 2 and $b_{\mathrm{T-C}}$ is on the order of 4. The value of $C_{\mathrm{T-C}}$ depends on lithology.

The SDR models are of the form (e.g., Seevers 1966),

$$K = C_{\mathrm{SDR}}(T_{2\mathrm{ML}})^{a_{\mathrm{SDR}}}\phi_{\mathrm{NMR}}^{b_{\mathrm{SDR}}}, \tag{15}$$

where C_{SDR}, a_{SDR} and b_{SDR} are empirically derived constants. In the original formulation of the equation, a_{SDR} was 1 and b_{SDR} was 2; however, under the assumption of fast diffusion, a_{SDR} should be set to 2. The value of b_{SDR} ranges from 2 to 4 (e.g., Weller et al. 2010). In petroleum well-logging analysis, permeability and NMR data collected from rock cores are used to determine the constants in Eqs. (14) or (15) for each lithologic layer within a well and then used to determine a calibrated NMR estimate of permeability for an entire well log. Numerous lab-NMR studies have attempted to determine universal estimates of the constants with limited success (e.g., Weller et al. 2010). By comparing the value of T_2^* determined from SNMR measurements to estimates of the hydraulic conductivity determined from grain size analysis, a simplified equation to estimate the hydraulic conductivity was proposed by Yaramanci et al. (1999) where it was found that $C_{\mathrm{SDR}} = 1.1$, $a_{\mathrm{SDR}} = 4.14$, and $b_{\mathrm{SDR}} = 0$ for K in cm/s.

The lack of a universal set of coefficients that describes K based on Eqs. (14) and (15) likely stems from two factors. First, both equations assume that K can be estimated from bulk properties of the system rather than the effective properties. However, laboratory experiments have shown that K–C models yield values that correlate well for K within a sedimentary unit, but the accuracy is typically limited to plus or minus one order of magnitude (Thompson et al. 1987). The limitation of K–C models arises from the fact that such models link K to the bulk or total volume properties of the porous medium, e.g., ϕ and S_{por}, whereas the properties controlling fluid flow are the pore throat radius and the interconnected porosity (Katz and Thompson 1986). Second, in samples where the effective properties are equal to the bulk properties, using T_2 to estimate S_{por} may lead to errors due to the non-uniqueness introduced by ρ_2 in Eq. (9). The determination of S_{por} assumes that ρ_2 is known or can be estimated; however, the value of ρ_2 depends on paramagnetic content and mineralogy and can vary over orders of magnitude (Keating and Knight 2007). In order to try and obtain a more accurate estimate of K for aquifer materials, multiple studies have attempted to developed NMR-K models that account for slow diffusion by changing the value of a_{SDR} or by using Eq. (10) to estimate S_{por} rather than Eq. (9) (Dlubac et al. 2014; Dlugosch et al. 2012).

3.5 Effect of Magnetic Field Inhomogeneities on NMR Relaxation Times

One area that has received a lot of attention in near-surface geophysics studies of NMR methods is the effect of magnetic field inhomogeneities on NMR relaxation times. Magnetic field inhomogeneities can enhance the transverse relaxation rate (either T_2 or T_2^*), which in extreme cases can lead to relaxation occurring entirely within the measurement dead time resulting in a complete loss of signal (e.g., Roy et al. 2008). Magnetic field inhomogeneities in lab-NMR or in BNMR are caused by imperfections in the static field, applied gradients, and/or differences in the magnetic susceptibility of the solid-phase

material and the saturating fluid. In SNMR, magnetic field inhomogeneities can also be caused by large-scale magnetic features such as a dyke (Vouillamoz et al. 2011).

As discussed in Sect. 2.1, inhomogeneities in the magnetic field require that a third term be used in the equation for the transverse relaxation time:$T_{2\mathrm{IH}}$ for T_2^* and $T_{2\mathrm{D}}$ for T_2. $T_{2\mathrm{IH}}$, in Eq. (5), is often approximated by

$$\frac{1}{T_{2\mathrm{IH}}} = \frac{\gamma}{2\pi}\Delta B, \tag{16}$$

where ΔB is the total variation in the magnetic field (e.g., Chen et al. 2005; Grunewald and Knight 2011b; Müller et al. 2005); however, the exact form of Eq. (16) depends on the pore-scale properties and the statistical distribution of the magnetic field inhomogeneities (Grunewald and Knight 2011b). In addition, when magnetic field inhomogeneities are present and pores are large, the FID can be non-exponential further complicating the interpretation of NMR data in inhomogeneous fields (Grunewald and Knight 2012).

$T_{2\mathrm{D}}$ is often approximated by (Fantazzini and Brown 2005; Kleinberg and Horsfield 1990)

$$\frac{1}{T_{2\mathrm{D}}} = D\frac{(\gamma G t_{\mathrm{E}})^2}{12}, \tag{17}$$

where D, as previously defined, is the self-diffusion coefficient of water, G represents the average magnetic field gradient, and t_{E} is the echo time. In a study of the effect of the presence of magnetite, a mineral with a high magnetic susceptibility, on the NMR signal, it was found that smaller particles of magnetite had a stronger impact on the relaxation time and that higher concentrations of magnetite led to faster relaxation (Keating and Knight 2008). Since magnetic field inhomogeneities typically result in unreliable estimates of the hydraulic conductivity, a large number of studies have focused on estimating T_1 values in the field (e.g., Legchenko et al. 2004; Müller-Petke et al. 2013; Walbrecker et al. 2011b; Walbrecker and Behroozmand 2012). In the petroleum industry, it has been recognized that a new pulse sequence can be used to take advantage of the inhomogeneities in the magnetic field to improve estimates of pore-size distributions and to differentiate oil-filled porosity from water-filled porosity (e.g., Song 2013).

3.6 Use of NMR for Vadose Zone Applications

While NMR measurements on water-saturated materials are well studied, there have only been a limited number of studies that focus on the interpretation of NMR measurements for applications in the vadose zone. As the relaxation time distribution (Sect. 3.2) has been linked to the pore-size distribution, the relaxation time distribution of a saturated sample has been used to estimate the water retention curve, WRC (e.g., Costabel and Yaramanci 2011a; Jaeger et al. 2009). However, in the vadose zone, soils are typically unsaturated. For unsaturated geologic media, the average relaxation time and relaxation time distribution have been shown to be function of saturation (e.g., Chang and Ioannidis 2002; D'Orazio et al. 1990; Jaeger et al. 2009; Pohlmeier et al. 2009; Stingaciu et al. 2009). Costabel and Yaramanci (2011a) noted that for unsaturated geologic media, unlike saturated geologic media, the T_2-distribution is not a measure of the pore-size distribution, but rather a measure of the distribution of the water within the pore space at a specific degree of saturation. Due to the relation between relaxation time and saturation, a number of studies have focused on estimating the unsaturated hydraulic conductivity, K_{U}, and the WRC from

unsaturated, unconsolidated sediments (e.g., Chen et al. 1994; Costabel and Yaramanci 2011a; Ioannidis et al. 2006).

Costabel and Yaramanci (2011b) introduced a Brooks–Corey parameterization of unsaturated NMR measurements of T_2, although the same approach could be used for T_1,

$$S_{\mathrm{NMR}} = \left(\frac{T_{2\mathrm{S}}}{T_{2\mathrm{S,Sat}}}\right)^{\lambda} = T_{2\mathrm{S,Rel}}^{\lambda}, \tag{18}$$

where $T_{2\mathrm{S}}$ is the relaxation time in an unsaturated state, $T_{2\mathrm{S,Sat}}$ is the surface relaxation time at saturation, $T_{2\mathrm{S,Rel}}$ is the relative value of $T_{2\mathrm{S}}$ calculated from the ratio of $T_{2\mathrm{S}}$ to $T_{2\mathrm{S,Sat}}$, and λ is a fitting parameter. Costabel and Yaramanci (2011b) assumed that λ corresponds to the parameter relating matric potential to saturation in the Brooks–Corey model of the WRC and that it would range from 0.1 for materials with broad pore-size distributions to 2 for materials with narrow pore-size distribution. Laboratory experiments have shown that λ is greater than 1 for the porous glass materials with pore diameters of 4 nm and 1 μm (Mattea et al. 2004), for glass beads with mean diameters of 300 μm (Ioannidis et al. 2006), and for industrial sands with low iron(III) concentrations with mean grain diameters ranging from 0.06 to 2 mm (Costabel and Yaramanci 2011b). However, evidence also exists that the value of λ is a function of the value of κ. In particular, Costabel (2011) presented a model for the relaxation time as a function of saturation for a single pore where at each degree of saturation, the water was distributed as film on the surface of a pore of ideal shape. The results of this model suggest that differences in λ are not only due to the homogeneity of the grain size distribution but also depend on the regime in which the relaxation of the saturated sample occurs. Costabel's model indicated that $\lambda \sim 1$ for samples in the fast diffusion regime and $\lambda < 1$ for samples outside the fast diffusion regime.

In an early paper focused on estimating K_{U} from NMR parameters, Chen et al. (1994) proposed a method for estimating the ratio of K_{U} to K, K_{U}/K, from the ratio of the unsaturated transverse NMR relaxation time, $T_{2-\mathrm{U}}$, to the saturated transverse relaxation time, T_2 and the NMR-estimated water saturation. This approach was later verified by Ioannidis et al. (2006) using a gravity drainage experiment on a column of glass beads. In a laboratory study where measurements were collected on a wide range of natural sediments, Costabel and Yaramanci (2011a) expanded the equation proposed by Chen et al. and showed that the same equation can be used with T_2^* in place of T_2. However, Costabel and Yaramanci note that if NMR measurements are collected using instruments with long dead times, the water content may be underestimated in materials with short relaxation times. This in turn could lead to large errors in estimates of K_{U}. Furthermore, the equation for estimating the K_{U} from NMR measurements requires that the saturated relaxation time be known and depends on an empirically determined constant, which could limit the widespread application of this approach in the vadose zone.

Although no robust model has been developed that can be used to estimate vadose parameters, the direct relation between the initial signal amplitude and water content makes the NMR measurement useful for analysis of the vadose zone. Ongoing research in this area will lead to improved models for estimating vadose zone parameters. Additionally, novel instrumentation that is capable of higher resolution measurements of NMR parameters in the top ~ 1 m of the subsurface has recently been developed, which make an understanding of the link between NMR parameters and vadose zone parameters even more relevant (Walsh et al. 2012).

3.7 NMR In Biogeophysics

Biogeophysics is an emerging area of Earth Sciences concerned with the "geophysical signatures of microbial interactions with geologic media" (Atekwana and Slater 2009). Biogeophysics has primarily been applied to understand the microbial processes associated with the remediation of contaminants (e.g., Naudet et al. 2003); however, understanding geophysical signatures associated with microbes and microbial interactions also has potential applications in monitoring biofilm growth and microbially enhance oil recovery. In this section, the recent lab-NMR studies that are within the area of biogeophysics are discussed; included in this discussion is the effect of geochemical changes on the NMR measurements.

The presence and growth of microbes in porous media can have a strong impact on the NMR relaxation time. As microbes are composed in a large part of hydrogen-bearing molecules, microbes themselves have an NMR response and the growth of microbes in porous media changes the effective pore structure resulting in a change in the NMR response. In a study of natural humus soils, lower relaxation times were associated with soils with higher microbial activity (Jaeger et al. 2006). Additionally, multiple studies have shown that the NMR response of a sample decreases significantly when microbial growth causes biofouling (i.e., the growth of biofilms; Codd et al. 2011; Sanderlin et al. 2013).

As can be seen from Eq. (9), in addition to the pore geometry, the surface relaxivity also impacts the NMR relaxation time. The surface relaxivity is governed by the presence of paramagnetic ions on the surface of a pore; in this context, paramagnetic ions imply ions with an unpaired electron such as iron(III) or manganese(II). Multiple studies have shown that the relaxation time decreases as a function of the concentration of iron(III) or manganese(II) on the surface of a pore (Bryar et al. 2000; Foley et al. 1996) and that the NMR response of a material depends on the mineralogy and the redox state of the iron and/or manganese in the measured sample (Bryar and Knight 2002; Jaeger et al. 2008; Keating and Knight 2007, 2010). Keating et al. (2008) showed that NMR measurements are sensitive to changes in iron mineralogy, and thus, as iron mineralogy often plays an important role in the remediation of contaminants, these results indicate that NMR measurements can be used as a proxy for monitoring important geochemical reactions associated with contaminant remediation. Furthermore, a recent study looked at the effect of uranium, a redox active contaminant, on the NMR response (Vogt et al. 2012). This study demonstrated that the conversion of soluble uranyl ions by microbial reduction to sparingly soluble uraninite, which is used as a method for immobilizing subsurface uranium contamination, impacted both T_2 and T_2^* relaxation implying that NMR measurements have the potential to monitor uranium remediation. While these studies demonstrate the potential of NMR, it is not yet known whether these measurements can be directly transferred to field applications and much research, and testing is still needed before NMR can be fully realized as a tool for monitoring in situ contaminant remediation.

4 Borehole Nuclear Magnetic Resonance (BNMR)

BNMR tools have been available for use in the petroleum industry since the 1960s (Brown and Gamson 1960) and are currently regarded as a mature technology that is used to characterize the pore space and fluids within petroleum reservoirs. However, the tools used for investigating petroleum resources, which were designed to withstand high pressures, are much too large for near-surface investigations; for instance, the MR Scanner (Schlumberger) is 10 m long, 12.1 cm in diameter, and weighs 544 kg. Since near-surface

wells are typically 5–12 cm in diameter, despite interest in using NMR to log near-surface wells, widespread use of this instrument is not possible. In the past few years, new slimline BNMR instruments have been developed specifically for use in near-surface environments (Sucre et al. 2011; Walsh et al. 2013). In this section, an overview of the slimline BNMR instrumentation used for near-surface investigations is presented and the applications for which BNMR tools have been used are discussed. For information about tools developed for petroleum applications, the reader is directed to Freedman (2006) and Allen et al. (2000). Since this is a relatively new technology for near-surface studies, it is anticipated that there will be a large growth in the use of slimline BNMR for hydrogeological and environmental investigations in the near future.

4.1 BNMR Measurements and Instrumentation

The past few years have seen the production of a number of slimline BNMR tools that have been developed for hydrogeologic and environmental investigations. Current slimline BNMR tools all rely on an "inside out" magnetic field as the static field, that is, a magnet is used to generate a static field outside of the tool, and this "stray field" is used to probe the formation outside of the borehole (Sucre et al. 2011; Walsh et al. 2013). The resulting static field is highly inhomogeneous. Since the field strength decreases with distance from the tool, the Larmor frequency can be tuned to detect regions that are different distances away from the center of the tool. In BNMR measurements, the depth of investigation of the instrument is defined as the distance from the center of the tool to the region in the formation probed by the instrument. The geometry of the region in the formation probed by the instrument depends on the design of the detection coil. The existing slimline BNMR instruments are sensitive to a thin cylindrical region around the outside of the borehole, depicted in Fig. 6; this design is similar to the initial BNMR instruments for petroleum applications (Perlo et al. 2013; Walsh et al. 2013). The standard pulse sequence available in slimline BNMR instruments is the CPMG pulse sequence, which is used to determine T_2. Slimline BNMR instrumentation varies greatly in field strength and associated Larmor frequency, probe size, depth of investigation, vertical resolution, and minimum echo time. The largest instrument, the Javelin (Vista Clara Inc.), is the only commercially available slimline BNMR instrument and was designed to detect the undisturbed formation, i.e., the region in the formation that is not impacted by the drilling and installation of a well, in near-surface boreholes (Walsh et al. 2013). The Javelin operates at Larmor frequencies ranging from 245 to 295 kHz and comes in different sizes ranging from 4.4 to 13.3 cm (1.75–5.25 in) in diameter and measures the formation in a thin cylindrical shell of a few millimeters thickness around the borehole; Fig. 6 shows the volume measured with the Javelin instrument. The depth of investigation ranges from 10 to 19 cm (4–7.5 in). The vertical resolution of the Javelin ranges from 50 to 100 cm (20–40 in), and the minimum echo time is 1.3 ms. The non-commercial slimline BNMR tool, the "Slimline logging" (SLL) NMR tool, was developed by researchers from Aachen University (Perlo et al. 2013). The SLL NMR tool operates at a Larmor frequency of 3.32 MHz and is 4.1 cm in diameter. The depth of investigation of the SLL NMR tool is 4.5 cm from the center of the tool, the vertical resolution is 10 cm, and the minimum echo time is 250 μs.

4.2 Overview of BNMR Studies

Both the petroleum BNMR tools and the new generation of slimline BNMR tools have been used to investigate near-surface geological environments for applications including

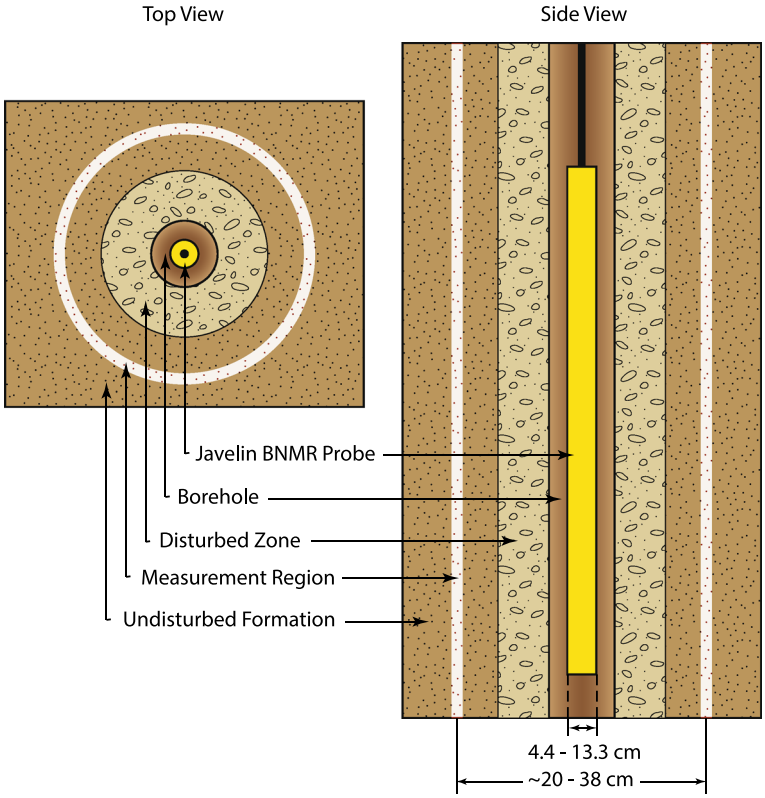

Fig. 6 Overview of the BNMR setup for the Javelin tool. The thin cylindrical measurement region around the borehole is shown in *red*. The figure is not drawn to scale; *dimensions* shown represent the range of dimensions for the Javelin tool. Figure modified from Walsh et al. (2013)

estimating hydraulic parameters (water content, hydraulic conductivity, and pore-size distributions) of aquifers to evaluating groundwater resources and for aquifer storage and recovery projects (Dlubac et al. 2013; Maliva et al. 2009; Walsh et al. 2013) and determining moisture profiles in the vadose zone (Sucre et al. 2010; Walsh et al. 2013). The hydraulic parameters estimated from BNMR logs compare favorably to drilling, geologic, natural gamma, electromagnetic induction, neutron probe and wellbore flow logging, as well as slug tests (Dlubac et al. 2013; Johnson et al. 2012; Walsh et al. 2013). It is important to note, however, that the BNMR-estimated hydraulic conductivity values and pore-size distributions require site-specific calibration to give the true values, and otherwise only represent relative values (Walsh et al. 2013); NMR estimates of hydraulic conductivity are discussed in detail in Sect. 3.4. In a study completed in the High Plains aquifer, Nebraska, USA, NMR estimates of hydraulic conductivity obtained from a petroleum logging tool, the MR Scanner, were compared to measurements of hydraulic conductivity obtained using wellbore flow logging; when a set of site-specific empirical constants were defined for the materials at this site, the NMR hydraulic conductivity estimates were found to be very reliable (Dlubac et al. 2013). Another recent study presented a statistical bootstrapping method for estimating the SDR parameters and for determining uncertainty in NMR-*K* models (Parsekian et al. 2014). The study showed that

uncertainty in the NMR estimates of K was comparable to colocated direct flow-based measurements of K for unconsolidated fluvial aquifer material in a borehole in Lawrence, Kansas, USA. An important consideration when using BNMR, as noted by Dlubac et al. (2013), is that BNMR measurements are strongly affected by the magnetic properties of the drilling mud and washouts within the borehole, suggesting that BNMR logs should be run in wells that have been drilled using sonic logs and/or run in conjunction with calipers to measure the diameter of the well.

5 Surface Nuclear Magnetic Resonance (SNMR)

SNMR has now been successfully adapted as a noninvasive surface-based geophysical method to assess aquifer properties. The SNMR measurement consists of a large wire loop deployed on the surface that typically acts as both a transmitter and a receiver (Fig. 7). Using Earth's magnetic field as the static field, the SNMR measurement samples the large volume of protons in groundwater. The basic principles of the method are reviewed by Legchenko and Valla (2002) and presented in two book chapters by Yaramanci and Hertrich (2006) and Lange et al. (2007). This section starts with historical developments of SNMR followed by the principal theory and applications of the method. An overview of SNMR-related topics and review of the recent advances in measurement techniques, signal processing, forward and inverse modeling, and hydrological parameter estimations are then presented.

5.1 Historical Developments

The original idea for development of SNMR in Earth's magnetic field dates back to the late 1970s. The first instrument, the 'HYDROSCOPE,' was developed in Russia in the 1980s based on the idea that Earth's magnetic field could act as a static magnetic field for NMR measurements. The HYDROSCOPE was the first instrument to detected NMR signals from in situ groundwater (e.g., Semenov et al. 1982; Semenov 1987; Semenov et al. 1988). More recently, a PC-based version of SNMR equipment was developed in Russia (AQUATOM equipment; see, e.g., Schirov and Rojkowski 2002a and Schirov et al. 1999). Based on the success of the HYDROSCOPE system (e.g., Gev et al. 1996; Goldman et al. 1994; Schirov et al. 1991; Shushakov and Legchenko 1994) a collaboration was established between the Russian scientists and researchers at the French Geologic Survey (BRGM) to develop the first commercial SNMR equipment, the NUMIS, in 1995. After a few years, a modular version of this initial system, the NUMIS Plus, which facilitated ease of transportation and supported a larger depth of investigation, was commercialized. In 2003, a reduced power, smaller, and less expensive version of the NUMIS Plus, the NUMIS Lite, which was suitable for shallower targets, was made commercially available (Bernard 2007). However, these single-channel SNMR instruments were highly susceptible to anthropogenic noise (e.g., Schirov et al. 1991).

To expand the applicability of SNMR measurements, in the 2000, instrumentation development was directed toward multi-channel SNMR systems capable of greater noise suppression than single-channel SNMR systems. Vista Clara Inc. developed the first commercially available multi-channel (four to eight channel) SNMR system called the GeoMRI (later reduced to GMR; Walsh 2006). IRIS Instruments subsequently developed a multi-channel (four channel) instrument called the NUMIS Poly, which, in addition to having multiple channels, has reduced measurement dead time over previous NUMIS

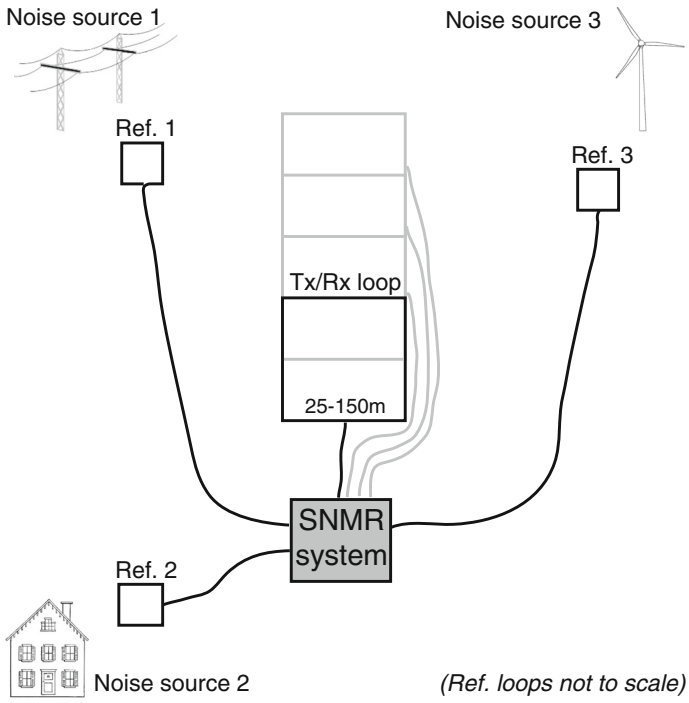

Fig. 7 SNMR field setup. The transmitter and receiver loop(s) can be different shapes and sizes and be laid out in different configurations. With the NUMIS Poly instrument, up to three reference loops, which are typically smaller than the transmitter/receiver loop and contains multiple wire turns can be deployed. With the GMR instrument, the reference loops are typically the same size and shape as the transmitter/receiver loop, and up to seven reference loops can be used. The noise sources shown here represent a subset of all sources that affect the SNMR signal

versions and supplied fulltime series sampling. In addition to the two major SNMR systems, Radic Research developed a multi-channel (seven channel) system, the MRS MIDI II, for shallow investigations up to 10 m (see, e.g., Radic 2005; Walbrecker et al. 2009, 2011a). Additional instruments that are in active development are not covered in this review (e.g., Tingting et al. 2012).

From its inception, researchers have not agreed on a consistent terminology for the surface-based NMR measurement. Some researchers have referred to it as 'proton magnetic resonance' or PMR (e.g., Guillen and Legchenko 2002; Legchenko and Valla 2002; Shushakov and Legchenko 1994); however, this does not distinguish the surface measurements from proton NMR measurements made in the laboratory. Other studies have referred to 'magnetic resonance sounding' or MRS for 1D Earth parameterization (e.g., Behroozmand et al. 2012b; Hertrich et al. 2005; Müller-Petke and Yaramanci 2008), and to 'surface NMR tomography' for 2D/3D parameterization (e.g., Hertrich et al. 2007). In this review, the convention 'surface nuclear magnetic resonance' is used to encompass 1D, 2D, and 3D surveys; this terminology is consistent with studies where the method is abbreviated as surface NMR or SNMR (e.g., Irons et al. 2010; Knight et al. 2012; Walbrecker et al. 2011a).

5.2 Methodology

In this section, the basic theory of the SNMR method is described. For a comprehensive derivation of the SNMR signal, valid for arbitrary transmitter and receiver loop geometry, the reader is directed to Weichman et al. (2000) and Hertrich (2008).

As mentioned in Sect. 2, the physical property used in SNMR applications is the spin of hydrogen protons in water molecules. For the SNMR measurement, the magnetic moments of the hydrogen nuclei of the subsurface water molecules are situated within Earth's magnetic field, $\boldsymbol{B}_{\mathrm{E}}$, which acts as the static magnetic field, and the protons precess about Earth's magnetic field. At thermal equilibrium, each small volume of water in the subsurface acquires a small net magnetic moment, which results from the sum of the magnetic moments associated with the protons in that volume. The net magnetic moment points in the same direction as Earth's magnetic field [see Eq. (1)]. In the following sections, Earth's magnetic field and the evolution of magnetic moments during SNMR excitation are discussed.

5.2.1 Earth's Magnetic Field

As mentioned in Sect. 2, the intensity of Earth's magnetic field at the surface ranges from less than 25 μT to more than 65 μT, depending on geographical location. This corresponds to Larmor frequencies in the range 1.06–2.8 kHz (a map of Earth's magnetic field can be found at www.ngdc.noaa.gov/geomag). The SNMR signal depends not only on the field strength, but also on the inclination of Earth's magnetic field; the effective (i.e., perpendicular) component of the energizing magnetic field to Earth's magnetic field scales with the inclination (Sect. 5.2.2). Earth's magnetic field is typically considered homogeneous within the SNMR investigated volume under the assumption that there are no strongly magnetic materials. However, temporal variation in Earth's magnetic field (due to diurnal variation or solar activity) may affect the local resonance conditions. Earth's magnetic field has a diurnal variation of about 0.2–0.5 μT, corresponding to Larmor frequency variations on the order of a few Hertz. If Earth's magnetic field is continuously measured during SNMR data acquisition, then the frequency offset can be accounted for in the forward model (e.g., Legchenko 2004; Walbrecker et al. 2011a).

5.2.2 SNMR Forward Response

In SNMR applications, the static and energizing magnetic fields are relatively weak, compared with most lab-NMR and BNMR experiments. Since the signal strength scales as $\boldsymbol{B}_{\mathrm{E}}^2$ [see Eqs. (1) and (20)], the SNMR signal is very small, on the order of nanovolts. To gain sufficient signal, large subsurface volumes must be energized and the noise reduced by advanced signal processing algorithms (Sect. 5.4).

The excitation pulse is generated, and subsurface spins are excited, by passing a current pulse, tuned to the local Larmor frequency, and through the transmitter loop. The current pulse is characterized by the pulse moment, q, defined as the product of the current amplitude and the pulse duration, $q = I_0 \cdot \tau_{\mathrm{p}}$. The applied pulse generates a corresponding energizing magnetic field, $\boldsymbol{B}_{\mathrm{T}}(\boldsymbol{r})$, whose intensity and direction depend on the subsurface electrical resistivity structure and the measurement configuration. The energizing magnetic field is weak, which necessitates the use of long pulse durations of 20–40 ms. The penetration depth of $\boldsymbol{B}_{\mathrm{T}}(\boldsymbol{r})$ typically falls within the top 100 m of the subsurface. In electrically conductive material, however, the signal attenuates and the field becomes elliptically

polarized as it propagates through the subsurface limiting the depth penetration (Hertrich 2008; Weichman et al. 2000).

To model the forward response of the SNMR signal, in each elementary volume in the subsurface, $\boldsymbol{B}_{\mathrm{T}}(\boldsymbol{r})$ is considered to be homogeneous; the component of $\boldsymbol{B}_{\mathrm{T}}(\boldsymbol{r})$ perpendicular to $\boldsymbol{B}_{\mathrm{E}}$, $\boldsymbol{B}_{\mathrm{T}}^{\perp}(\boldsymbol{r})$, then interacts with the spins and tips their magnetization away from the equilibrium state, as discussed in Sect. 2. $\boldsymbol{B}_{\mathrm{T}}^{\perp}(\boldsymbol{r})$ can be decomposed into the sum of two components circularly polarized relative to the spin precession, $\boldsymbol{B}_{\mathrm{T}}^{\perp}(\boldsymbol{r}) = \boldsymbol{B}_{\mathrm{T}}^{+}(\boldsymbol{r}) + \boldsymbol{B}_{\mathrm{T}}^{-}(\boldsymbol{r})$, where $\boldsymbol{B}_{\mathrm{T}}^{+}(\boldsymbol{r})$ is the corotating component and $\boldsymbol{B}_{\mathrm{T}}^{-}(\boldsymbol{r})$ is the counter-rotating component. $\boldsymbol{B}_{\mathrm{T}}^{+}(\boldsymbol{r})$ is the component of the transmitted field that acts on the spins to tip them out of alignment with $\boldsymbol{B}_{\mathrm{E}}$. In SNMR, the tip angle is defined as $\theta_{\mathrm{T}}(\boldsymbol{r}, \tau_{\mathrm{p}}) = \omega_{\mathrm{T}}(\boldsymbol{r})\tau_{\mathrm{p}} = \gamma\left|\boldsymbol{B}_{\mathrm{T}}^{+}(\boldsymbol{r})\right|\tau_{\mathrm{p}}$, where $\omega_{\mathrm{T}}(\boldsymbol{r})$ is the transmitter pulse angular frequency and is theoretically equal to the Larmor angular frequency. The tip angle varies throughout the volume, and its value at a given location depends on the both the pulse duration and the magnitude of $\boldsymbol{B}_{\mathrm{T}}^{+}(\boldsymbol{r})$ (see Fig. 8 and details in Sect. 5.2.3). Because the energizing field is rapidly weakened with distance, spins located far from the transmitter loop are not energized and it is only necessary to include spins within a distance of 2–3 times the loop size in the numerical forward calculation.

After the energizing pulse is turned off, the precessional motion of the decaying transverse component of the magnetization, the FID, produces a weak oscillating magnetic field. This signal propagates in the subsurface and can be measured inductively using a receiver loop on the surface. The measured signal is a superposition of the signals arising from all the precessing nuclear spins within the excited Earth volume. To provide depth information, the signal is measured with a series of pulse moments exciting different Earth volumes.

The general expression for the induced SNMR voltage in the receiver loop is (e.g., Müller-Petke and Yaramanci 2010b)

$$V(q,t) = \int K(q,\boldsymbol{r}) \int W(\boldsymbol{r}, T_2^*) \cdot \mathrm{e}^{-\frac{t}{T_2^*}} \mathrm{d}T_2^* d^3\boldsymbol{r}. \tag{19}$$

This model is referred to as the QT SNMR signal as $V(q, t)$, which denotes the measured SNMR signal, is dependent on both q and time, t. T_2^*, as mentioned earlier, is the effective transverse relaxation time, $\boldsymbol{r}$ is the position, $W(\boldsymbol{r}, T_2^*)$ is the partial water content (i.e., water content distribution in space and at different relaxation time values), and $K(q,\boldsymbol{r})$ is the kernel function. The decay curve starts at the time zero, which is defined as the center of transmitter pulse as discussed in detail in Sect. 5.3. Under on-resonance conditions, $K(q,\boldsymbol{r})$ becomes (Hertrich 2008; Weichman et al. 2000)

$$\begin{aligned} K(q,\boldsymbol{r}) = {} & \omega_{\mathrm{L}} M_0 \sin\left(-\gamma \frac{q}{I_0}\left|\boldsymbol{B}_{\mathrm{T}}^{+}(\boldsymbol{r})\right|\right) \\ & \times \frac{2}{I_0}\left|\boldsymbol{B}_{\mathrm{R}}^{-}(\boldsymbol{r})\right| \cdot e^{i[\zeta_{\mathrm{T}}(\boldsymbol{r},\omega_{\mathrm{L}}) + \zeta_{\mathrm{R}}(\boldsymbol{r},\omega_{\mathrm{L}})]} \\ & \times \left[\hat{\boldsymbol{b}}_{\mathrm{R}}^{\perp}(\boldsymbol{r},\omega_{\mathrm{L}}) \cdot \hat{\boldsymbol{b}}_{\mathrm{T}}^{\perp}(\boldsymbol{r},\omega_{\mathrm{L}}) + i\hat{\boldsymbol{b}}_0 \cdot \hat{\boldsymbol{b}}_{\mathrm{R}}^{\perp}(\boldsymbol{r},\omega_{\mathrm{L}}) \times \hat{\boldsymbol{b}}_{T}^{\perp}(\boldsymbol{r},\omega_{\mathrm{L}})\right] \end{aligned}, \tag{20}$$

where ω_{L} is the angular Larmor frequency and I_0 is transmitter loop current. As mentioned above, $\boldsymbol{B}_{\mathrm{T}}^{+}(\boldsymbol{r})$ is the corotating component of the projected transmitter field into the plane perpendicular to $\boldsymbol{B}_{\mathrm{E}}$. Similarly, $\boldsymbol{B}_{\mathrm{R}}$ denotes a virtual magnetic field from a unit current in the receiver loop, and the counter-rotating component of its projection into the plane perpendicular to $\boldsymbol{B}_{\mathrm{E}}$ is denoted by $\boldsymbol{B}_{\mathrm{R}}^{-}(\boldsymbol{r})$. $\hat{\boldsymbol{b}}_0$, $\hat{\boldsymbol{b}}_{\mathrm{T}}^{\perp}$ and $\hat{\boldsymbol{b}}_{\mathrm{R}}^{\perp}$ are unit vectors, $\hat{\boldsymbol{b}}_0$ points in the

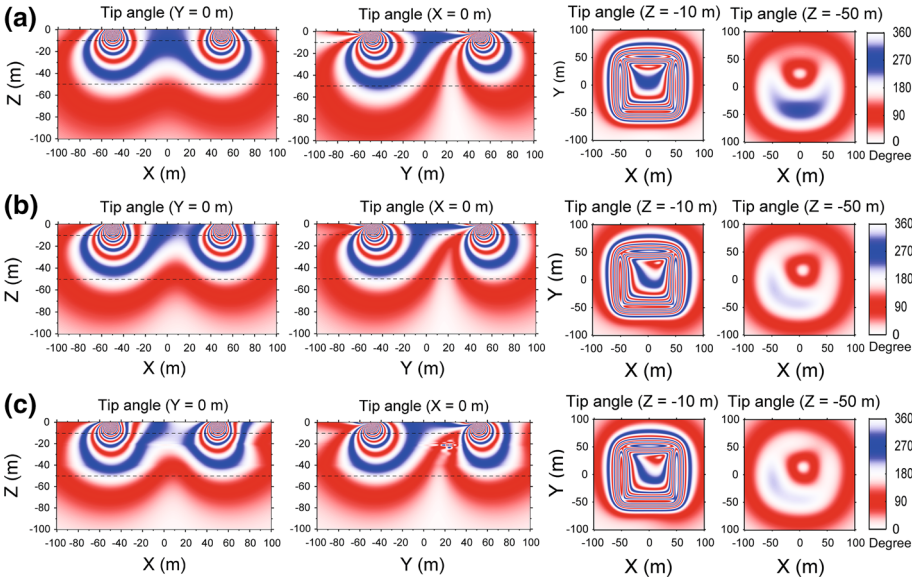

Fig. 8 Numerical simulations of the SNMR tip angle for different geologic models: **a** a homogeneous 10,000 Ωm half-space, **b** a homogeneous 20 Ωm half-space, **c** a three-layer model with resistivity values of 10, 100 and 10 Ωm and thicknesses of 20 and 20 m, respectively. Column 1: vertical x–z ($y = 0$) slice of the 3D tip angle; column 2: vertical y–z ($x = 0$) slice of the 3D tip angle; columns 3 and 4: horizontal x–y slices of the 3D tip angle at depths 10 and 50 m. The color shows the tip angle values oscillating between 0 and 360°. The simulations were carried out for a 10 As pulse moment

direction of $\boldsymbol{B}_{\mathrm{E}}$, $\hat{\boldsymbol{b}}_{\mathrm{T}}^{\perp}$ points in the direction of the component of the transmitter field perpendicular to $\boldsymbol{B}_{\mathrm{E}}$, and similarly $\hat{\boldsymbol{b}}_{\mathrm{R}}^{\perp}$ points in the direction of the component of the receiver field perpendicular to $\boldsymbol{B}_{\mathrm{E}}$. ζ_{T} and ζ_{R} are the phase lags from transmitter to the sample (observation point) and from the sample to the receiver. The rest of the variables in Eq. (20) are as previously defined.

To calculate the energizing magnetic field, the resistivity structure of the subsurface is needed. In some cases, it is assumed that the subsurface is a resistive half-space; however, this assumption is often invalid, and so it is recommended that the resistivity structure be obtained from a complementary geophysical method such as transient electromagnetic (TEM) or DC resistivity.

In typical SNMR surveys, a coincident transmitter/receiver loop configuration is used, that is, the same loop is used to transmit the energizing pulse and receive the NMR signal, and a 1D Earth structure, i.e., a horizontally stratified subsurface, is considered. In this case, Eq. (20) simplifies to

$$K(q,\boldsymbol{r}) = \omega_{\mathrm{L}} M_0 \sin\left(-\gamma \frac{q}{I_0}\left|\boldsymbol{B}_{\mathrm{T}}^{+}(\boldsymbol{r})\right|\right) \times \frac{2}{I_0}\left|\boldsymbol{B}_{\mathrm{T}}^{-}(\boldsymbol{r})\right| \cdot \mathrm{e}^{2i\zeta_{\mathrm{T}}(\boldsymbol{r},\omega_{\mathrm{L}})}. \tag{21}$$

The response is obtained by integrating Eq. (19) over x and y

$$V(q,t) = \int K(q,z) \int W(z,T_2^*) \cdot e^{-\frac{t}{T_2^*}} \mathrm{d}T_2^* \mathrm{d}z. \tag{22}$$

Due to the long effective dead time, standard SNMR measurements do not provide the total water content as information of the very fast decaying signals disappear before the measurement starts. The SNMR-estimated water content, i.e., the partial water content defined as W in Eq. (22), is the portion of the total water content that is not bound to the grain surface or located in very fine pores.

5.2.3 Tip Angle and SNMR Sensitivity Function

As with other geophysical methods, SNMR measures an average of the physical parameters to which it is sensitive over a given volume. However, not all parts of the subsurface contribute equally to this average. For a given field setting, both the tip angle and the kernel, also called the sensitivity function, express how a change in the physical parameters at a point in the subsurface will change the SNMR data. Both the tip angle and kernel depend on Earth's magnetic field (both magnitude and inclination), transmitted field, pulse moment, loop configuration, and resistivity structure of the subsurface.

First, consider the behavior of the tip angle. Figure 8 shows an example of the variation of the tip angle in the subsurface. In Fig. 8, the SNMR tip angle was determined for three geologic models: (a) a homogeneous 10,000 Ωm half-space (b) a homogeneous 20 Ωm half-space and (c) a three-layer horizontally stratified model with resistivities of 10, 100, and 10 Ωm and thicknesses of 20 and 20 m, respectively. The simulations were carried out for a coincident square loop with loop-side length of 100 m, centered at the origin, $(x, y, z) = (0, 0, 0)$. A pulse moment of 10 As was used. Earth's magnetic field intensity, inclination, and declination were set to 50,030 nT, 70° and 0°, respectively. The columns of Fig. 8 represent vertical (x–z, columns 1; y–z, column 2) and horizontal (x–y, columns 3 and 4) slices of the 3D tip angle. The depths at which columns 3 and 4 are sliced are marked with dashed lines in the panels of columns 1 and 2. The tip angle values oscillate between 0° and 360° degrees; most of the oscillations occur in the shallow subsurface (compare columns 3 and 4). The regions with 90° (red) and 270° or −90° (blue) tip angles contribute most to the SNMR kernel because the tip angle is in a sine function, as shown in Eq. (20). The effect of the resistivity structure on the tip angle can be seen by comparing the rows of Fig. 8. In a resistive medium (row 1), the tip angle structure penetrates deeper than in a conductive medium (rows 2 and 3). Moreover, an asymmetrical pattern, with respect to the $x = 0$ axis, is apparent (see columns 1, 3 and 4), which is due to spatial distribution of $\boldsymbol{B}_T^+(\boldsymbol{r})$ in conductive media. For the layered resistivity model (row 3), a deformation of the tip angle structure appears, compared with the structure from a homogeneous half-space model. Finally, comparing columns 3 and 4 for all resistivity structures shows that in the shallow regions of the subsurface, the tip angle structure has a square-shaped pattern, while in deeper regions, a circular pattern is observed. The change in the shape of the tip angle distribution is due to the loop shape; in shallow regions the energizing field of a square loop will be different from that of a circular loop of similar size, whereas in deeper regions, the energizing fields from a square or a circular loop will look the same (compare columns 3 and 4 with Fig. 4 in Weichman et al. 2000).

To explore the different components of the SNMR sensitivity function, 3D numerical simulations of the SNMR kernel are displayed in Fig. 9a. The simulations were carried out for a homogeneous 20 Ωm half-space with site specifications as for Fig. 8. The columns of Fig. 9a represent vertical (x–z, column 1; y–z, column 2) and horizontal (x–y, columns 3 and 4) slices through the 3D SNMR kernel; the rows of Fig. 9a represent the real and imaginary components of the 3D SNMR kernel. The kernel is normalized by the value

displayed in the bottom left hand corner of each panel. As with Fig. 8, the panels of Fig. 9a display the complexities of the kernel in the subsurface and demonstrate the need for accurately discretizing the subsurface when forward modeling SNMR data. The kernel shows an oscillatory feature (due to the tip angle contribution) in shallow regions with larger values than at depth, as expected. A notable feature shown in Fig. 9a is the depth of the information obtained from the imaginary component of the kernel in the presence of conductive medium. This demonstrates that there is an advantage to using the imaginary component of the SNMR signal (see sections 5.5 and 7). As in Fig. 8, comparing columns 3 and 4 shows that the shallow regions of the kernel structure have a square-shaped pattern due to the shape of the transmitter/receiver loop, while a circular pattern is observed at depth (compare columns 3 and 4 with Figs. 8 and 9 in Weichman et al. 2000).

The SNMR kernel is often simplified by integrating over the horizontal plane (x and y), which leads to a 1D function with depth. Depending on the pulse moment, different parts of the 3D kernel might cancel each other out when integrating over x and y. Figure 9b shows an example of a 1D SNMR kernel as a function of depth and pulse moment for different subsurface resistivity structures; homogeneous half-space models with resistivity values of 10,000, 100, 10 and 1 Ωm and a three-layer horizontally stratified model with resistivities of 10, 100, and 10 Ωm and thicknesses of 20 and 20 m, respectively. Using the same site specifications as in Figs. 8 and 9a, 1D kernels were calculated for pulse moment values ranging from 1 to 15 As. The rows in Fig. 9b show the real and imaginary components of the 1D kernel. As can been seen from the figure, the sensitivity varies substantially across the range of pulse moments and resistivity structures; however, for all resistivity structures, the depth penetration of the sensitivity function increases when higher pulse moments are applied. For the 10,000 Ωm homogeneous half-space model (column 1), the kernel is real-valued and the zone of sensitivity reaches depths of 100 m. For the 100 Ωm homogeneous half-space (column 2), the real component shows the same behavior as in column 1 with slightly shallower depth penetration; however, at this resistivity, a nonzero imaginary component emerges with depth. For the conductive models in columns 3 and 4, both the real and imaginary components of the kernel attenuate significantly with depth and the imaginary component is much larger than in columns 1 or 2. For the three-layer model in column 5, both the real and imaginary components of the kernel show a similar pattern to column 3. However, the kernel penetrates deeper due to the presence of the 100-Ωm layer. For more details about the behavior of the SNMR sensitivity function, the reader is directed to Weichman et al. (2000), Hertrich (2008), Braun et al. (2009), Lehmann-Horn et al. (2011a; 2012) and Behroozmand et al. (2013a).

Next, consider the effect of Earth's magnetic field on the NMR signal. From Eqs. (1) and (20), it is clear that the sensitivity function depends on the magnitude of Earth's magnetic field. An increase in the magnitude of Earth's magnetic field will increase the spin magnetization and thereby increase the SNMR signal. However, a change in the magnetic field also changes the Larmor frequency. An increase in the magnitude of Earth's magnetic field increases the Larmor frequency, which leads to a lower penetration depth of the transmitted B-field. Finally, the inclination of Earth's magnetic field scales the effective (perpendicular) components of the transmitter and receiver magnetic fields, i.e., $\boldsymbol{B}_{\mathrm{T}}^{+}(\boldsymbol{r})$ and $\boldsymbol{B}_{\mathrm{R}}^{-}(\boldsymbol{r})$, which both affect the kernel [see Eq. (20)].

Finally, let us consider the effect of the loop configuration on the sensitivity function. SNMR data are conventionally collected using square (Fig. 7), circular, square figure-eight and circular figure-eight coincident loops with loop-side lengths and diameters ranging from $\sim$25 to 150 m. For the coincident loop configuration, if excitation is on-resonance

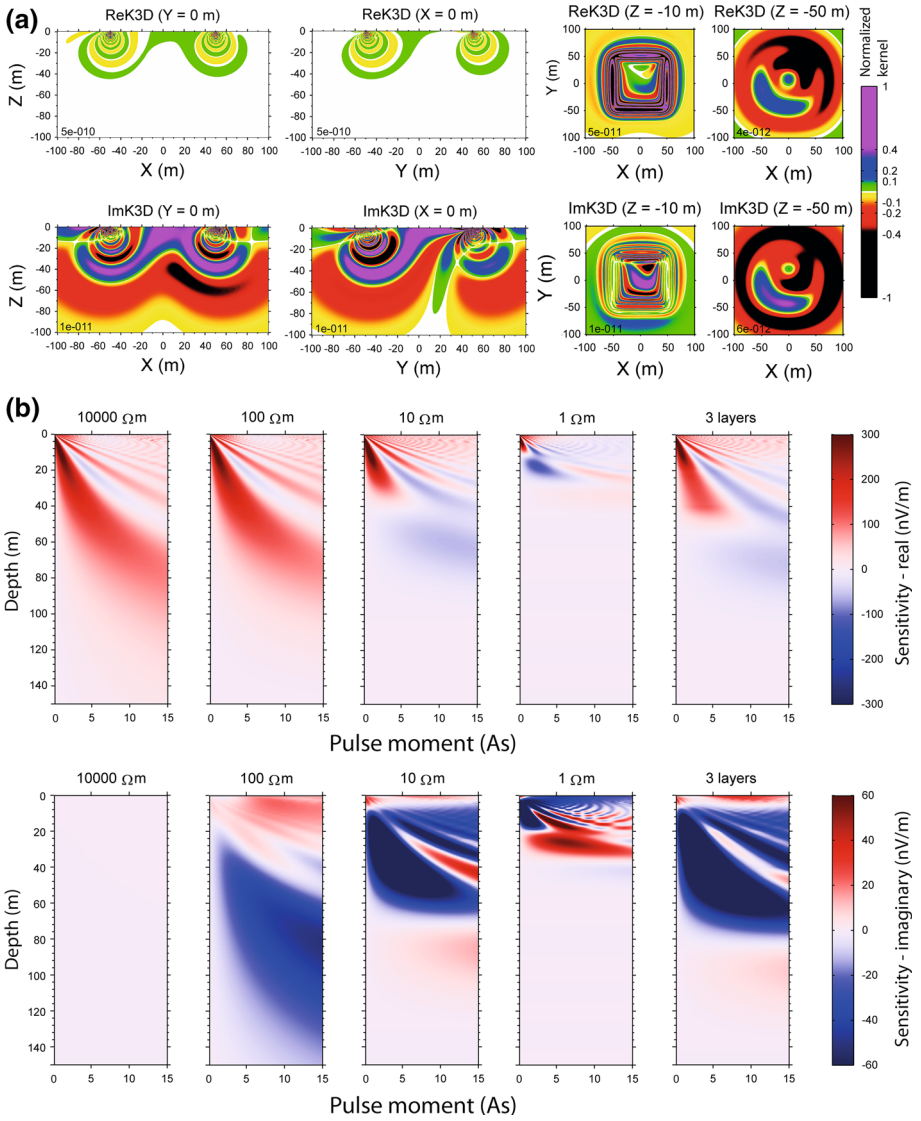

Fig. 9 **a** Numerical simulations of the 3D SNMR kernel for a homogeneous 20 Ωm half-space. Rows 1 and 2 display the real and imaginary parts of the kernel, respectively. Column 1: vertical x–z ($y = 0$) slice of the 3D kernel; column 2: vertical y–z ($x = 0$) slice of the 3D kernel; columns 3 and 4: horizontal x–y slices of the 3D kernel at depths 10 and 50 m. The color shows the kernel values normalized by the value displayed in the *bottom left hand corner* of each panel. The simulations were carried out for a 10 As pulse moment. **b** The 1D SNMR kernel as a function of depth and pulse moment for different homogeneous half-space resistivity models with resistivities of 10,000 Ωm (column 1), 100 Ωm (column 2), 10 Ωm (column 3) and 1 Ωm (column 4), and a three-layer model (column 5) with resistivity values of 10, 100 and 10 Ωm and thicknesses of 20 and 20 m, respectively. Rows 1 and 2 display real and imaginary parts of the kernel, respectively (note the difference in scale). The 1D kernels are simulated for pulse moment values ranging from 1 to 15 As

and instrument phase is neglected, then the kernel function is real-valued for a resistive ground and complex-valued for a conductive ground (see Fig. 9b). Although less common, a separated loop configuration has also been used to acquire SNMR data (e.g., Behroozmand et al. 2013a; Hertrich 2008; Müller-Petke 2013). The third line in Eq. (20) accounts for separate transmitter and receiver loops and can be neglected, i.e., set to one, when coincident loops are used. However, in the separated loop configuration, the third line in Eq. (20) contributes to the imaginary component of the kernel. This means that in the separated loop configuration, even in the case where the ground is resistive, excitation is on-resonance, and the instrument phase is neglected, the kernel function is complex.

In a recent study, Davis and Macnae (2012) considered the impact of using compact receivers (z-axis oriented dipole) for both dB/dt and B-field measurements on the SNMR sensitivity function. Subsequently, Davis et al. (2014), in a novel study, showed that the secondary magnetic field (on the order of femtoTesla) can be directly measured using a compact B-field sensor located at the center of the transmitter loop. Davis and Macnae (2012) and Behroozmand et al. (2013a) found that when central loop configuration was used to collect SNMR data, the 1D SNMR kernel displays oscillatory behavior with respect to pulse moment (research in this area is ongoing).

5.3 SNMR Pulse Sequences

Although SNMR data are typically collected using an FID, a variety of different pulse sequences have been developed for SNMR. Due to the long pulse durations, collecting SNMR measurements is significantly more challenging than collecting lab-NMR or BNMR measurements. In this section, the differences between theoretical FID measurements and FID measurements collected using SNMR instrumentation are presented. Additionally, the pulse sequences that have been developed for SNMR, including those developed to determine T_1 and T_2, will be presented. Finally, the effect of pulsing off resonance will be discussed.

5.3.1 SNMR FID Measurements

As shown in Fig. 2a, the FID is measured using a single-pulse acquisition scheme and the measured signal is an exponential decay characterized by T_2^*. The measured signal oscillates at the Larmor frequency, which is ideally equal to the frequency of the energizing pulse. In SNMR, the signal is not measured in the rotating laboratory frame, and so envelope detection of the FID is needed to provide both T_2^* and E_0. In lab-NMR and BNMR, it is commonly assumed that relaxation processes do not occur until the transmitted pulse has turned off; however, in SNMR measurements, because both τ_p and t_{dead} are long ($\sim$10–40 ms) compared to the measured relaxation time, significant relaxation can occur during the pulse, referred to as relaxation during pulse or RDP. Consequently, to obtain accurate estimates of T_2^* and E_0, the signal must be extrapolated back before the end of the energizing pulse to the point in time where the relaxation processes originate.

Walbrecker et al. (2009) performed a comprehensive study on the influence of RDP based on numerical simulations and sample-scale Earth's field NMR experiments with conditions closely matching those of SNMR applications. This study demonstrated that ignoring RDP can introduce errors in E_0 and the associated water content up to 25 % and errors in T_2^* up to 50 %. The RDP effect is significant for τ_p greater than 20 % of the measured T_2^*. The numerical simulations confirmed earlier results that extrapolating the

signal back to $\tau_p/2$ (assuming time zero at the beginning of transmitted pulse; see Fig. 2) provides a much better estimate of both T_2^* and E_0 and can reduce RDP-related errors to less than 2 % (Walbrecker et al. 2009; Weichman et al. 2000).

5.3.2 SNMR T_2 Measurements

In SNMR studies, it is difficult to collect T_2 data due to practical limitations such as long measurement dead time and imperfect transmit pulses. However, driven by the impact of magnetic minerals on T_2^* [Eq. (5)], attempts have been made to estimate T_2 using the spin echo pulse sequence (Grunewald et al. 2014; Legchenko et al. 2010; Shushakov 1996; Vouillamoz et al. 2011). The spin echo pulse sequence is described in Sect. 2.1 and shown as the first two pulses of Fig. 2b. One complicating factor in the measurement of spin echo data with SNMR is that the application of the second refocusing pulses generates FID signals that may bias the measurement (these signals are not shown in Fig. 2b). These interfering FID's are generated because the applied pulses are not perfect; the initial pulse is not simultaneously 90° everywhere in the subsurface, and similarly, the second pulse is not simultaneously 180° everywhere in the subsurface. To eliminate the effects of the interfering FIDs, Grunewald et al. (2014) incorporated phase cycling, i.e., collecting pairs of measurements with alternated pulse phases, into the application of the spin echo pulses. Phase cycling is an approach that is commonly used in lab-NMR and BNMR to remove unwanted signals that are phase coherent with one or more pulses.

In addition to spin echo pulse sequences, two other pulse sequences have been developed to estimate T_2 with SNMR data. Grunewald and Walsh (2013) showed that the CPMG pulse sequence could be used with SNMR instrumentation; this pulse sequence has recently been introduced for use in the GMR (Fig. 2b; Grunewald and Walsh 2013). Grombacher et al. (2012) proposed SNMR-compatible composite pulses to quantify background magnetic field inhomogeneities and to estimate T_2 from T_2^* data. In this approach, a suite of composite pulses is applied and then the background magnetic field inhomogeneity is characterized through the inversion process. This information is then used to quantify and remove the component of static dephasing present in the measured FID.

5.3.3 SNMR T_1 Measurements

Although T_1 takes longer to measure than T_2 or T_2^* and is more difficult to measure than T_2^*, there is significant interest in measuring T_1 with SNMR because it is not influenced by magnetic field inhomogeneities and is thus a more reliable indicator of pore structure. A double-pulse acquisition scheme, called a pseudo-saturation recovery (PSR) pulse sequence (also called the quasi 90°–90° pulse sequence), is typically used to estimate T_1. In the PSR pulse sequence, the first excitation pulse is applied followed by a second pulse of opposite polarity applied after a delay time, τ_d (Fig. 2c; e.g., Chalikakis et al. 2009; Legchenko et al. 2002, 2004). A minimum of two delay times are required for a T_1 estimate; however, it is recommended that at least three delay times be used (e.g., Müller-Petke et al. 2013).

In the simplest case, where only one delay time is used, T_1 can be estimated for each pulse moment from

$$V_d(\tau_d) = E_{01}\left(1 - e^{-\tau_d/T_1}\right), \tag{23}$$

by fitting to the (τ_d, V_d) data. As shown in Fig. 2c, E_{01} is the recovery curve's asymptotic value, i.e., $V_d(\tau_d \rightarrow \infty) = E_{01}$. This equation assumes that $V_d = 0$ at $\tau_d = 0$; however, as with FID data, there can be significant RDP during the collection of T_1 data. Walbrecker et al. (2009) considered a modified version of Eq. (23) to account for possible offset of the initial value at $\tau_d = 0$ due to RDP

$$V_d(\tau_d) = V_0\left(1 - \theta e^{-\tau_d/T_1}\right), \tag{24}$$

where θ is a factor that accounts for the nonzero value of to the V_d at $\tau_d = 0$.

There are two shortcomings of the conventional scheme to obtain T_1. (1) As with the spin echo pulse sequence, if the pulses are not perfectly 90°, then there is a contribution from spins with flip angles other than 90° to the measured signal. (2) Due to instrumental power limitations, the amplitudes of the first and second transmitter excitation pulses are not equal. Walbrecker et al. (2011b) showed that these shortcomings result in biased estimates of T_1 because both T_1 and T_2^* components contributed to the measured signal that is mapped into the transverse plane, i.e.,V_d is not only a function of T_1. Walbrecker et al. used phase cycling to eliminate these effects, and the phase-cycled pseudosaturation recovery pulse sequence is referred to as pcPSR. In the pcPSR pulse sequence, two double-pulse sequences are applied: in the first, the two pulses are in phase, in the second, the two pulses are 180° out of phase. The voltage responses after each of the experiments are then subtracted, leaving V_d as a function of T_1 alone (Fig. 10a). In a field study, Walbrecker and Behroozmand (2012) confirmed that the pcPSR pulse sequence yields improved estimates of T_1 (Fig. 10b).

In a very different approach from that of Walbrecker et al., Grunewald and Walsh (2012) implemented the 'crush-recovery' pulse sequence to improve estimates of T_1. As with the PSR and pcPSR pulse sequences, the crush-recovery pulse sequences use a series of two pulses separated by different delay times; however, unlike the PSR and pcPSR pulse sequences, the first pulse is fixed with a high pulse moment and then followed by a pulse with a weaker pulse moment. The advantage of this pulse sequence is that it ensures identical resonance condition after the first excitation pulse and results in a simplified inversion algorithm.

5.3.4 Off-Resonance Effects on SNMR Measurements

In SNMR modeling, it is presumed that the experiment is carried out under on-resonance condition (i.e., the difference between the Larmor frequency and the transmitter frequency is zero; $\Delta\omega = \omega_L - \omega_T = 0$), and thus, all protons are excited at the Larmor frequency. However, this condition is not always met due to temporal and spatial variations in Earth's magnetic field leading to variations in the local Larmor frequencies and associated deviations from the transmitter frequency. Moreover, instrumental imperfections associated with the tuning of the energizing pulse may cause off-resonance effects or phase shifts (e.g., Legchenko 2004; Walbrecker et al. 2011a). Even in perfect conditions, a minimum frequency offset of $\sim$1–2 Hz is inevitable in SNMR experiments (e.g., Legchenko 2004; Walbrecker et al. 2011a).

The sources of off-resonance effects in SNMR are beyond user control and may introduce a phase shift on the signal that could be mistakenly interpreted as a variation in the electrical resistivity or as a deep aquifer. Several studies have considered the effects of off-resonance pulses on SNMR data (e.g., Girard et al. 2005; Hunter and Kepic 2005; Legchenko and Valla 1998; Trushkin et al. 1993). Comprehensive studies of the effects of

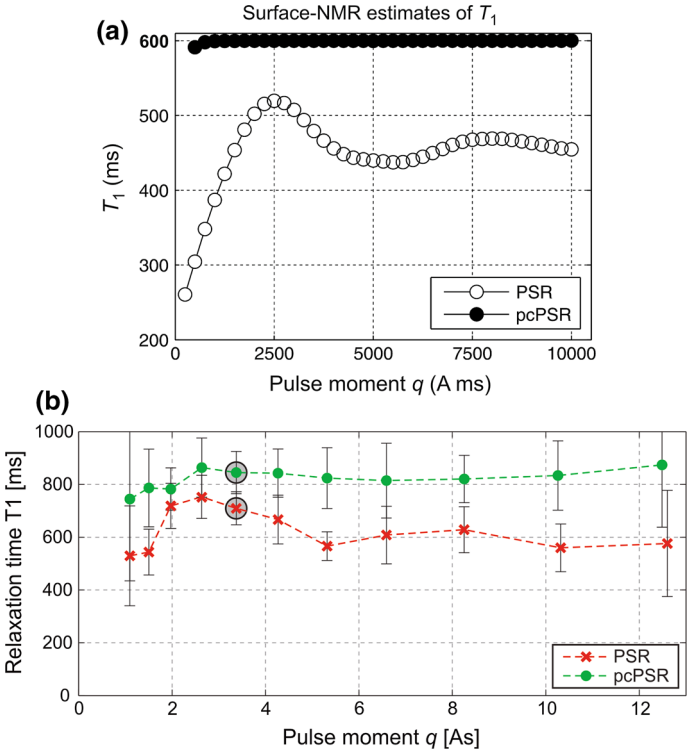

Fig. 10 **a** SNMR $T_1(q)$ estimates from exponential fits to three synthetic data points at different delay times of 200, 600 and 3,000 ms. A constant value of $T_1 = 600$ ms is considered throughout the geologic model. *Open circles* show the data obtained from PSR experiment which vary and differ from the constant model value of 600 ms, and *solid circles* correspond to the data obtained from pcPSR (figure used with permission from Walbrecker et al. 2011b). **b** A field experiment on a homogeneous sandy aquifer in Denmark provides empirical evidence for improved T_1 estimate when using pcPSR (*green circles*) over PSR (*red crosses*) to collect SNMR measurements (figure used with permission from Walbrecker and Behroozmand 2012)

off-resonance pulses on water content and relaxation time determinations through numerical simulations and experiments were done by Legchenko (2004) and Walbrecker et al. (2011a). They found that, for frequency offsets of up to 5 Hz, the single-pulse SNMR measurement produces reliable water content estimates provided that the pulse moments are small to moderate or the aquifer is relatively deep. However, for strong pulse moments or for shallow aquifers, the off-resonance effect is prominent and, as a result, an anomalous increase in recorded signal amplitudes can be mistakenly interpreted as a deep aquifer. The effect of pulsing off-resonance is enhanced in the double-pulse SNMR measurements, even for commonly encountered small frequency offsets (Walbrecker et al. 2011a).

Due to the effect of pulsing off-resonance on SNMR data, it is important to account for frequency offset effects in the forward modeling of SNMR data. Continuous measurements of Earth's magnetic field during SNMR data collection can be used to account for temporal variation in $\boldsymbol{B}_{\mathrm{E}}$ and the frequency offset can then be determined for each pulse moment. The frequency offset effect due to spatial inhomogeneities in the static magnetic field can be corrected by directly measuring the magnetic field variations with depth in the borehole (Grunewald et al. 2014; Knight et al. 2012). To account for variations in the Larmor

frequency, an effective tip angle is introduced, given by $\theta_{\text{eff}} = \omega_{\text{eff}}\tau_{\text{p}}$, where $\omega_{\text{eff}}^2 = \omega_1^2 + \Delta\omega^2$, in which $\omega_1 = \gamma\left|\boldsymbol{B}_{\text{T}}^{+}\right|$ (e.g., Walbrecker et al. 2011a).

5.4 Signal Processing

As mentioned in Sect. 5.2.2, the measured NMR signal from water in the subsurface is very small (on the order of hundreds of nanovolts). The raw SNMR signal is a combination of both the NMR signal from the groundwater and the signal from ambient EM noise sources. EM noise includes spikes (either natural, e.g., from lightning, or man-made, e.g., from electric fences), coherent signals from powerlines, and background random noise. Generally, the magnitude of the noise is much higher than the magnitude of the NMR signal, and the NMR signal of interest is masked by the noise. To obtain the NMR signal, the noise imposed on the measured signal must therefore be removed with appropriate hardware- and software-based signal processing. Signal processing is one of the primary research activities in the SNMR community (see, e.g., Baofeng et al. 2012; Costabel and Müller-Petke 2012a, b, 2014; Dalgaard et al. 2012; Larsen et al. 2014; Müller-Petke and Costabel 2012, 2014; Soltani and Xiao 2012; Walsh 2008).

The first noise-reducing scheme was to use a figure-eight-shaped loop, either a square or circular eight, for data acquisition (Trushkin et al. 1994). With this configuration, the current flows in opposite directions in each of the two loops formed by the figure-eight shape. Provided that the noise is stationary and equal in both loops, the ambient EM noise induced in the first loop is compensated by the noise induced in the second loop. Although it has been shown that the figure-eight-shaped loop configuration can be used to successfully collect data in noisy areas, this loop geometry reduces depth penetration when compared to similar sized square or circular loops.

Before the generation of multi-channel SNMR instruments, SNMR data were measured using a single channel, typically in the coincident loop configuration, and various processing schemes have been developed to suppress noise from single-channel-instrument data (e.g., Legchenko and Valla 1998, 2003; Strehl 2006). However, the efficiency of these processing schemes was limited due to the absence of real-time information about the noise imposed on the data. The development of multi-channel SNMR instrumentation changed the way in which noise is canceled. In multi-channel instruments, a number of reference loops are used in addition to the primary loop used for transmitting and receiving the NMR signal. An example of the primary and noise loop setup is shown in Fig. 7. Although these loops are commonly used to measure noise, they can also be used to record NMR signal. Since part of the noise recorded by the reference loops will be correlated with the noise in the primary loop, recording the signal in multiple loops enables the implementation of advanced processing schemes. Using signal processing, the noise recorded in the reference loops can be subtracted from the equivalent noise recorded in the primary loop and used to obtain the desired NMR signal (e.g., Dalgaard et al. 2012; Larsen et al. 2014; Müller-Petke and Yaramanci 2010a; Walsh 2008).

When using multiple loops for noise cancelation, a general SNMR-processing workflow contains the following steps. (1) *despiking*: Spikes in the raw SNMR data, which arise due to electrical discharges that are random in time, intense and often originate from different sources, are removed from all data records (Costabel and Müller-Petke 2014; Dalgaard et al. 2012; Jiang et al. 2011; Neyer et al. 2010; Strehl 2006); (2) *coherent noise cancelation*: coherent noise from sources such as power lines, which accounts for the majority of the noise in the raw SNMR signal, is filtered from the raw data using the noise recorded

in the reference channels. Filtering methods include Wiener filtering and adaptive noise cancelation (Dalgaard et al. 2012; Müller-Petke and Yaramanci 2011); (3) *stacking*: incoherent noise that remains in the data, after despiking and coherent noise cancelation, is suppressed by the appropriate averaging of multiple recordings; (4) *envelope detection*: finally, the desired signal, i.e., the envelope of the FID, is extracted by envelope detection and standard peak finding and fitting methods (e.g., Dalgaard et al. 2012; Neyer 2010). Envelope detection is done in multiple steps that consist of determining the true Larmor frequency, down converting the signal, determining and correcting for the phase offset, and low-pass filtering. It is noteworthy that often, the preprocessing of SNMR data involves band-pass filtering the signal from the receiver channels to a band of few hundred Hz centered around the Larmor frequency.

Larsen et al. (2014) presented an alternate workflow for removing noise from the SNMR signal. In this study, they combined model-based removal of powerline harmonics and multi-channel Wiener filtering. Larsen et al. suggested that the workflow be changed to include a second despiking after the model-based removal of powerline harmonics to eliminate minor spikes that might be masked by the powerline signal. This would expand step one in the workflow as follows: (1a) despiking (1b) model-based removal of powerline harmonics (1c) despiking.

5.5 Forward Modeling and Inversion

In this section, an overview of the different forward modeling and inversion approaches that are used in the analysis of SNMR data is presented. In Sect. 5.2.2, the full forward response of SNMR data was given; however, to simplify the forward modeling and inversion algorithms, the full forward response is not always used. Analysis approaches differ in terms of: (1) the data used, e.g., the initial signal amplitude or the full exponential decay, which is referred to here as data usage, (2) the SNMR decay characteristics, e.g., multi-exponential versus single exponential behavior, and (3) the full complex signal versus the signal amplitude. In addition, other forward modeling and inversion approaches include the sequential or joint inversion of SNMR data with other geophysical data, or inversion of $T_2^*/T_2/T_1$ data. Finally, as with other geophysical methods, the dimensionality of the inverse problem and the parameter determination of the inversion approach can vary. A flowchart of SNMR inversion schemes is shown in Fig. 11. In this section, the forward modeling and inversion algorithms for SNMR data associated with each of these approaches are reviewed.

Data usage. The SNMR data set is measured as a function of time and pulse moment, $V(q, t)$ [see Eqs. (19) and (22) and Fig. 12]. From the data space point of view, three major inversion schemes exist: (1) initial amplitude inversion (IAI), (2) time step inversion (TSI), and (3) QT, as it accounts for both q and t, inversion (QTI); see Table 2. In IAI, it is assumed that the relaxation is mono-exponential. The distribution of water content with depth is obtained by inverting the sounding curve (see Figs. 11, 12b), $E_0(q)$, which is the initial amplitude (extrapolated from the early-time data in the FID) versus the pulse moment (Legchenko and Shushakov 1998). In TSI, the data set is separated into different sounding curves (see Figs. 11, 12c) to determine the water content distribution at different time steps t_n; $W(z, t)$. $W(z, t)$ is then fit with either a mono-exponential decay curve (Legchenko and Valla 2002), which is used to determine the water content ($W(z)$) and relaxation times ($T_2^*(z)$) distribution with depth, or a multi-exponential fit (Mohnke and Yaramanci 2005), which is used to determine the partial water content and T_2^*-

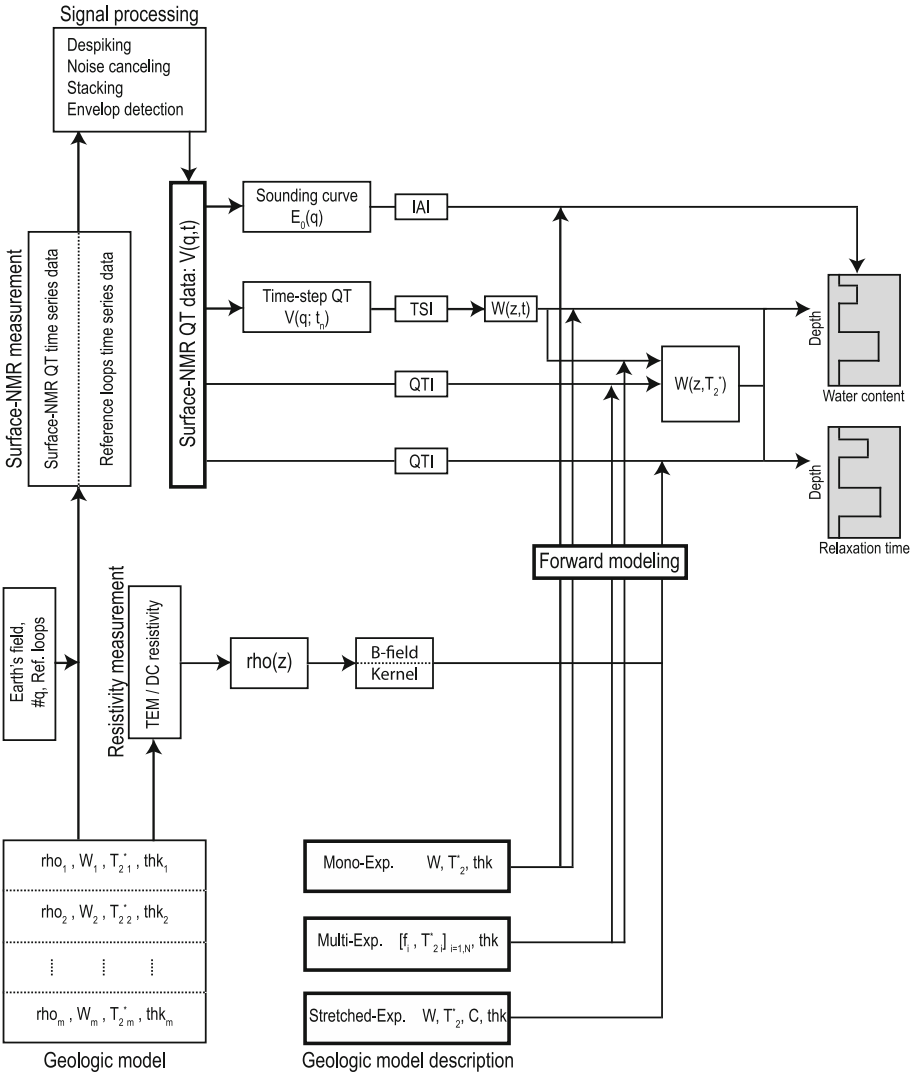

Fig. 11 Flowchart of SNMR inversion schemes. *Gray boxes* represent geologic model of the subsurface from inversion. For definition of the terms see Appendices 1 and 2, and Fig. 12

distributions, $W(z, T_2^*)$. In QTI, the entire data set is considered and is used to directly invert for $W(z, T_2^*)$; see Figs. 11 and 12b. Müller-Petke and Yaramanci (2010b) showed that the QTI approach led to improved determination of the inverted parameters compared with both IAI and TSI. Using field examples, Dlugosch et al. (2014) and Behroozmand et al. (2012a) also showed that including the complete data set led to improved discrimination of layers with different water contents and relaxation times. However, the entire data set consists of $\sim$15–20 pulse moments with 1 s of data measured at a sampling frequency of 19,200 Hz for the NUMIS and 50,000 Hz for the GMR resulting in a very large inverse problem. Therefore, the individual QT time series is commonly demodulated

through quadrature detection and down-sampling (Müller-Petke et al. 2011a) or, following Behroozmand et al. (2012b), integrated over time gates, which increases the signal-to-noise ratio and considerably reduces the size of the data space while maintaining the decay characteristics of FIDs. A recent study by Irons et al. (2012) suggested that the demodulation of the signal be done in the Fourier domain. The effective dead time then consists of half transmitter pulse length, instrument dead time, and the post-processing time interval before the first data point (Walsh et al. 2011).

SNMR decay characteristics. It is often assumed that the recorded SNMR signal is multi-exponential, due to the fact that it is a superposition of the signal arising from multiple layers of porous media with different relaxation behaviors. Additionally, even for a single horizontal layer, following Eq. (2), the relaxation behavior of each layer can exhibit multi-exponential behavior due to the pore-size distribution of the geologic material in the layer (Dunn et al. 2002a). As with the inversion of lab-NMR and BNMR

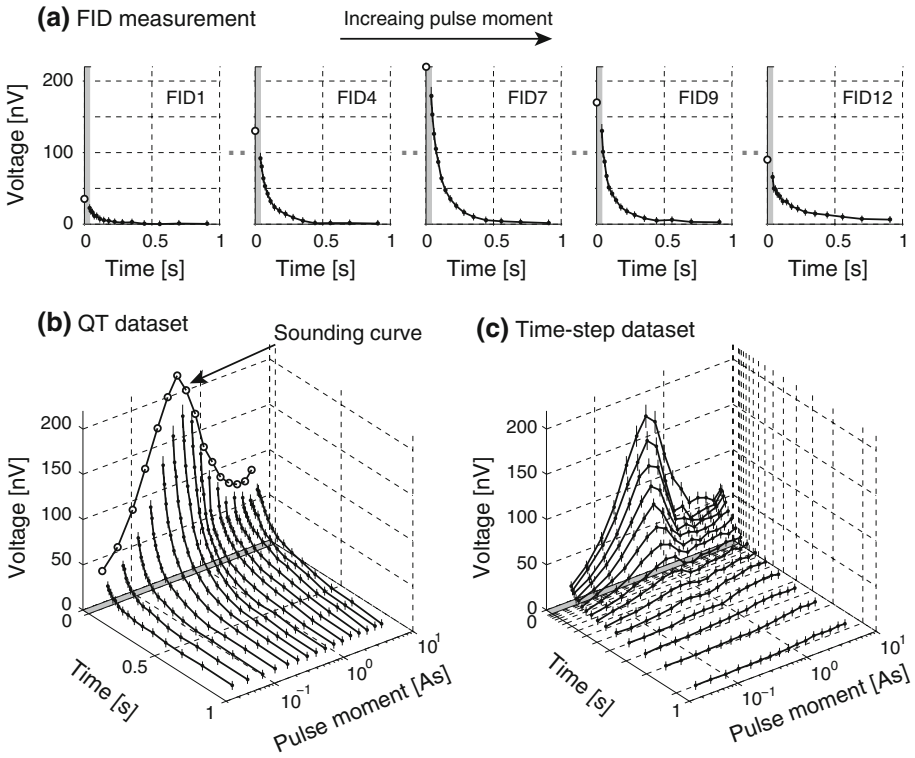

Fig. 12 SNMR data measurement. **a** FIDs are measured for a number of increasing pulse moment values (few of them are shown here). *Black dots* show data point at different time gate values and *vertical lines* represent associated errors on the data. The initial amplitudes (*open circles*) are obtained by extrapolating the curves back to the initial time, i.e., $\tau_p/2$. *Gray* regions show the effective dead time. **b** The entire SNMR data cube used for QTI consisting of the measured SNMR signal as a function of time and pulse moment. The sounding curve data consist of the initial amplitudes (*open circles*), obtained from the FIDs, as a function of pulse moment. **c** The same data set shown in (**b**) shown as the time step data set, which separates QT data into different sounding curves at each time steps. For (**b**) and (**c**) the lines connecting data points are shown to guide the eye. In the case of T_2/T_1 measurements, the data set shown in (**b**) and (**c**) is measured after each energizing pulse

Table 2 SNMR inversion methods and associated data usage; compare to Figs. 11 and 12

Inversion method	Data used	Description	References
IAI	Sounding curve; FID initial amplitudes versus the pulse moment ($E_o(q)$)	Inverts the initial amplitudes and returns water content distribution with depth ($W(z)$)	Legchenko and Shushakov (1998)
TSI	Sounding curves at different time steps ($V(q, t_n)$)	Inverts individual curves and returns water content with depth at different time steps ($W(z, t)$). A mono- or multi-exponential fit to $W(z, t)$ provides the water content and relaxation time distributions with depth $\left(W(z)\&T_2^*(z)\right)$ or the partial water content distribution ($W(z, T_2^*)$)	Legchenko and Valla (2002), Mohnke and Yaramanci (2005)
QTI	Full data cube (consist of exponential decays (FIDs) at different pulse moments; $V(q, t)$)	Inverts the entire data cube at once and returns ($W(z, T_2^*)$) directly	Müller-Petke and Yaramanci (2010b)

For definitions of the terms, see Appendices 1 and 2

data, the multi-exponential behavior can be represented using a set of log-spaced relaxation times assuming a smooth relaxation time distribution, a sum of a discrete number of exponential decays, or using a stretched exponential approach.

Mohnke and Yaramanci (2005) and Müller-Petke and Yaramanci (2010b) showed that SNMR data can be inverted using a smooth distribution of relaxation times; however, this approach is computationally expensive. Other studies have reduced the complexity of the physics of relaxation by fitting the data with a mono-exponential model (Günther and Müller-Petke 2012; Hertrich 2008). In studies using the HYDROSCOPE, the multi-exponential SNMR signal decay was simplified and approximated as the sum of three exponents with preset relaxation time constants corresponding to small, medium, and large pores (e.g., Goldman et al. 1994; Schirov and Rojkowski 2002b). The accuracy of this specific scheme depends on the possibility of representing a multi-exponential decay as a sum of the fixed exponents. A more recent approach for simplifying the inversion of the multi-exponential decay was presented by Behroozmand et al. (2012b) where the decay was modeled as a stretched exponential; as with lab-NMR and BNMR data, the stretched exponential approximation is valid when the pore-size distribution consists of either a single peak or two overlapping peaks. We note, however, that although it is typically assumed that the SNMR signal is multi-exponential, care must be taken in the interpretation of SNMR since, as shown by Grunewald and Knight (2012), under certain circumstances, i.e., in the presence of strongly inhomogeneous background field and large pores, the FID may be non-exponential in form.

Complex versus amplitude data. As discussed in Sect. 5.2, the measured SNMR signal is complex-valued. Although the full complex dataset is used during data processing for unbiased estimates of the NMR parameters, the imaginary or phase data often shows unreliable behavior and are not commonly used in the inversion of SNMR data. To simplify the inversion algorithm, most studies only consider either the amplitude of the dataset (e.g., Behroozmand et al. 2012b; Hertrich 2008; Legchenko et al. 2006, 2011; Müller-Petke and Yaramanci 2010b) or, in the case of QTI, the rotated amplitude data (Müller-Petke et al. 2011a) for inversion. The latter uses the results of the complex fit to rotate the signal, which corrects for the phase and frequency offset, into the real plane.

Various attempts have been made to develop a full complex inversion of SNMR data (e.g., Braun et al. 2005; Legchenko et al. 2008). As discussed in Sect. 5.2, the phase data originate from different sources, including the subsurface conductivity structure and the instrumental phase shifts. In theory, inverting the complex dataset could lead to improved inverted images, especially when deep conductive structures are present (e.g., Braun et al. 2005). However, the phase changes that arise due to instrument shifts are not easy to explain and complicate the inversion approach. If accurate knowledge of the instrument phase is provided and the impact of frequency offsets can be modeled, a complex inversion approach could provide a better estimation of NMR parameters due to the information contained in the imaginary component of the SNMR dataset.

Inversion methods. As mentioned in Sect. 5.2.2, the subsurface resistivity structure affects the transmitted magnetic field values and the SNMR kernel [Eq. (20)]. Therefore, information about the deep resistivity structure is required to accurately invert SNMR data; this information is particularly important when conductive structures exist (Behroozmand et al. 2012a). The resistivity data are typically obtained using independent geophysical measurements such as TEM or DC resistivity. Two approaches have been taken to include the resistivity structure in SNMR data. The first is a conventional stepwise inversion of SNMR data (e.g., Hertrich 2008; Legchenko and Shushakov 1998; Mohnke and Yaramanci 2002). In this method, the resistivity structure is obtained directly from the inversion of the resistivity data and is assumed to be

correct. The kernel is developed from the inverted resistivity structure and remains constant, and only the SNMR parameters are updated during the inversion. Recently, Behroozmand et al. (2012a) and Günther and Müller-Petke (2012) presented schemes for the joint inversion of SNMR and TEM or DC resistivity data, in which the resistivity structure is inverted simultaneously with the SNMR parameters. In the joint inversion method, the resistivity values are updated and, correspondingly, the kernel is updated, for each calculation of the SNMR forward response. The joint inversion approach leads to a more reliable and robust determination of aquifer characteristics when highly conductive layers exist.

The inversion algorithms discussed to this point were developed to invert for water content and T_2^*; however, due to the different pulse acquisition schemes necessary to collect the data, different algorithms are necessary to invert for water content and either T_1 or T_2. Inversion algorithms have been developed to invert SNMR data for T_1, using the double-pulse acquisition scheme (e.g., Chalikakis et al. 2009; Legchenko et al. 2004) or the pcPSR acquisition scheme (Müller-Petke and Walbrecker 2012 and Walbrecker et al. 2012), and for T_2 (e.g., Grunewald et al. 2014; Legchenko et al. 2010; Shushakov 1996). In contrast to T_2^* estimates, inversion of SNMR T_2/T_1 data helps distinguish whether fast decaying signals are due to the presence of magnetic material or if they are due to an impermeable material such as clay; see e.g., Grunewald et al. (2014).

Dimensionality of the inverse problem. The previous discussion of the forward modeling and inversion algorithms focused on 1D models, as a 1D Earth model is commonly assumed in the inversion of SNMR data. Weichman et al. (2000) and Hertrich (2008) presented a comprehensive and general derivation of SNMR signal. As such, inversion algorithms have been developed for 2D Earth models (e.g., Hertrich et al. 2007, Lehmann-Horn et al. 2011b and Dlugosch et al. 2013) and 3D Earth models (Legchenko et al. 2011 and Chevalier et al. 2011).

Parameter determination. To understand the limitations of the SNMR measurement, it is essential to assess the resolution and accuracy of the SNMR parameters in the inverted model, irrespective of the inversion method. A large number of studies regarding the accuracy of SNMR parameter determination have been published; for additional studies not covered in this review the reader is directed to Günther and Müller-Petke (2012), Müller-Petke et al. (2011a), Lehmann-Horn et al. (2012), Schirov and Rojkowski (2002a), and Müller-Petke (2013).

The depth of investigation of SNMR data varies as a function of loop size, maximum pulse moment, and the subsurface resistivity. Using singular value decomposition of the SNMR forward operator, Müller-Petke and Yaramanci (2008) determined that, for a half-space resistivity model, increasing loop diameter alone does not necessarily increase the depth of investigation due to the scalability of the noise with the loop area. However, they found that increasing the maximum pulse moment does increase penetration depth. Furthermore, they found that, to some extent, a more resistive half-space corresponds to deeper penetration (see Fig. 9b). Additional research has shown that the presence of a low-resistivity layer on top of an aquifer will significantly decrease the depth of investigation (Behroozmand et al. 2013b).

In a joint SNMR and TEM data analysis scheme, Behroozmand et al. (2013b) studied the effect of resistivity, water content, relaxation time, loop-side length, number of pulse moments, measurement dead time, and noise level on the SNMR-determined water content. They considered a range of different layered Earth models with an aquifer located at different depths and found that water content determination is not affected by size of the transmitter/receiver loop or the number of pulse moments but that it is limited by the noise levels. Decreasing the measurement dead time, particularly when there are geologic units

with relatively short relaxation times, improved water content determination; similarly, increasing the relaxation time of the signal in the aquifer improved the water content determination. These results are consistent with previous claims that short dead times must be used to obtain early-time SNMR signal information (Dlugosch et al. 2011;Walsh et al. 2011). Behroozmand et al. (2013a) compared parameter determination of separated loop with the conventional coincident loop SNMR data and suggested that separated loop configurations may have equivalent sensitivity as the coincident loop data.

Dalgaard et al. (2013) analyzed the influence of the number and distribution of pulse moments and the number of stacks (i.e., number of records) on the model parameter determination. The results from the study showed that there is an upper limit on the number of pulse moments required to obtain a reasonable parameter determination; the specific value of this limit depends on the geologic model. Above the limit the data acquired using a higher number of pulse moments and lower number of stacks provide the same parameter determination as the data acquired using a lower number of pulse moments and higher number of stacks. Furthermore, Dalgaard et al. determined an optimal q distribution that gives an improved determination of model parameters when compared with a logarithmic q distribution.

5.6 Estimating Hydrological Parameters

As with BNMR, one of the most appealing aspects of SNMR is the associated noninvasive estimates of K. In the interpretation of SNMR data, the empirical relation between the relaxation time (either T_2^*, T_2 or T_1), the NMR-estimated water content and K as mentioned in Sect. 3.4, can be calibrated using estimates of K from locally conducted aquifer tests where available. Based on that, a number of studies have dealt with estimating hydrogeological parameters and found a good correlation between the results of borehole aquifer tests and estimates from SNMR measurements (e.g., Boucher et al. 2009; Chalikakis et al. 2008, 2009; Lachassagne et al. 2005; Legchenko et al. 2002; Lubczynski and Roy 2003; Plata and Rubio 2008). Due to the large scale of SNMR measurements, Legchenko et al. (2002) recommend using the transmissivity to estimate hydrogeological parameters of aquifers. Recently, Vilhelmsen et al. (2014) proposed two methods for full joint hydrogeophysical inversion of SNMR, TEM and aquifer test data in which they apply, as a part of the inversion, an empirical petrophysical relation between SNMR-estimated parameters and hydraulic conductivity.

6 Case Studies

The application of NMR in near-surface geophysics is quickly growing. Numerous case studies have been published showing that NMR geophysics can be used in a variety of different near-surface environments including permafrost environments (e.g., Parsekian et al. 2013), the vadose zone (e.g., Costabel and Günther 2012; Costabel and Yaramanci 2011a, b; Roy and Lubczynski 2005; Walsh et al. 2012, 2014), hard rock aquifers (e.g., Legchenko et al. 2006), karst (e.g., Chalikakis et al. 2011; Vouillamoz et al. 2003) and arid regions (e.g., Schirov et al. 1991; Vouillamoz et al. 2008). Other studies have been published showing that results from SNMR studies are complementary to results obtained from other geophysical measurements including ground penetrating radar (e.g., Yaramanci et al. 2002), vertical electrical soundings (e.g., Perttu et al. 2011; Wattanasen and Elming 2008), EM methods (e.g., Auken et al. 2014; Behroozmand et al. 2012a; Irons et al. 2014) and BNMR measurements (Knight et al. 2012; Müller-Petke et al. 2011b). In this section, two

case studies in areas of emerging scientific importance in near-surface geophysics are considered. The first is a case study to address the capability of SNMR to assess permafrost environments, and the second is a case study comparing the reliability and scale of the SNMR measurements compared to BNMR measurements.

6.1 SNMR in Permafrost Environments

Understanding the extent of permafrost in northern environments is becoming increasingly important as global warming leads to increases in ground temperature and affects precipitation patterns. As permafrost thaws, it can change the structure of soils causing them to become unstable and it can also release subsurface stores of methane, acting as a positive feedback in the global carbon cycle. Therefore, using noninvasive methods to characterize the extent of permafrost has become an emerging area of interest in near-surface geophysics (e.g., Minsley et al. 2012). Among geophysical methods, SNMR is a promising method for the delineation of unfrozen structures in permafrost environments because the NMR measurement is directly sensitive to the unfrozen water content in soils (Callaghan et al. 1999; Kleinberg and Griffin 2005; Watanabe and Wake 2009). A few studies have been published recently showing that SNMR can be used to delineate unfrozen sediments from frozen sediments (Lehmann-Horn et al. 2011b; Parsekian et al. 2013; Turu 2012; Vincent et al. 2012; Yoshikawa et al. 2006). Here, the focus is on one study that investigated the capability of SNMR to detect unfrozen sediments below thermokarst lakes and to measure the depth of permafrost in Alaska (Parsekian et al. 2013).

In the study by Parsekian et al. (2013), SNMR data were collected at three sites. At two of the sites, the depth and extent of 'taliks,' i.e., unfrozen regions within a permafrost environment, below a frozen thermokarst lake were measured. Understanding talik geometry is important for understanding regional surface water and ground water interactions as well as subsurface methane production. At the third site, the depth to the bottom of the permafrost was measured. The authors used the SNMR initial amplitude data in a blocky inversion scheme to obtain a 1D water content depth profile; the inversion results for the three sites are shown in Fig. 13. This approach is suitable for geologic layers with sharp water content transitions, the results of which indicate the detection of unfrozen water. By constraining the SNMR data using the known lake depth and associated water content (i.e., 100 %), Parsekian et al. successfully obtained depth soundings of the unfrozen region beneath the lakes. At one lake (Ace Lake), the SNMR results showed that the depth of the talik was either open or connected to the groundwater system and that the talik extended deeper than the SNMR depth of investigation. At the second lake (Caribou Lake), the SNMR results showed that the talik was closed, i.e., underlain with permafrost. At the permafrost site (Bonanza Creek), the SNMR results revealed an unfrozen region beneath the permafrost layer. The SNMR results were in good agreement with available data, including TEM results and with borehole data at the permafrost site (see Fig. 13).

To validate the findings of the paper, Parsekian et al. developed synthetic SNMR sounding curves for the range of expected permafrost settings. These settings are shown in Fig. 14 and include a permafrost setting with groundwater located beyond the detection limit of the SNMR measurement, an isolated talik in a permafrost setting, a closed talik below a thermokarst lake, a permafrost setting with groundwater within the detection limit of the SNMR measurement, and an open talik below a thermokarst lake. In the forward modeling, it was assumed that permafrost had a water content of 4 % and that a talik had water content of 33 %. These models will help future researchers evaluate SNMR data in permafrost settings.

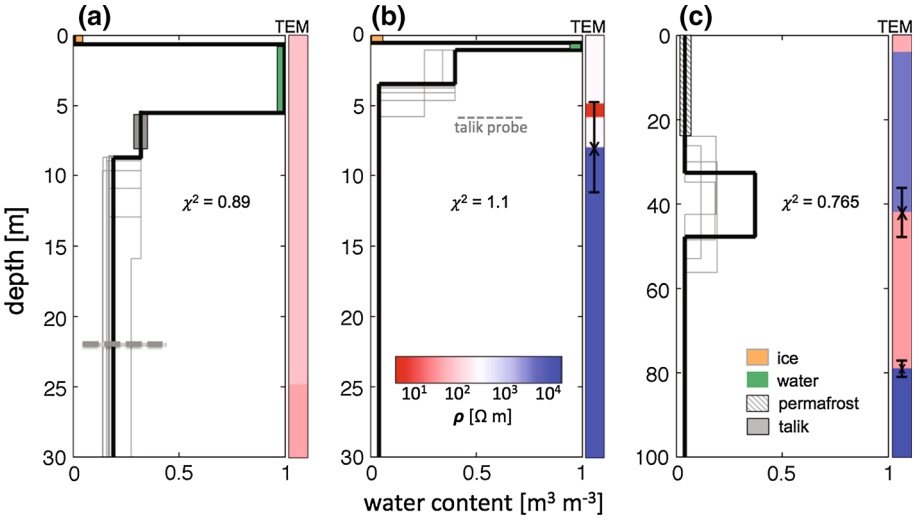

Fig. 13 Blocky inversion results from surface NMR soundings at the two thermokarst lakes, Ace Lake with an open talik or deep-closed talik (**a**) and Caribou Lake with a closed talik (**b**), and the permafrost site, Bonanza Creek (**c**). The *black line* for in each *graph* represents the best-fit model; the *gray lines* represent the range of models that fit the data nearly as well. The *dashed gray line* shows the maximum depth sensitivity for each sounding. The *colored boxes* plotted on the *black line* show the inversion constraints for layer thickness and water content, which were obtained from direct measurements. The TEM resistivity soundings are plotted as color bars. This figure was reproduced with permission from Parsekian et al. (2013)

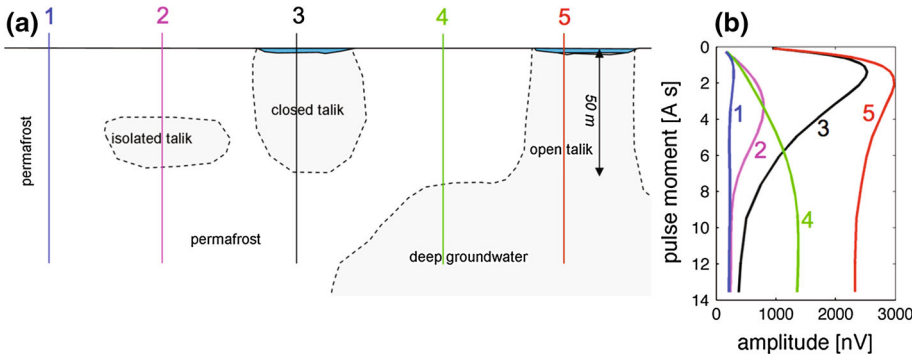

Fig. 14 Five potential scenarios in permafrost settings (**a**) and their associated synthetic NMR soundings (**b**). Scenario 1 is permafrost with groundwater beyond the detection limit of the SNMR measurement. Scenario 2 is an isolated talik in a permafrost setting. Scenario 3 is a closed talik below a thermokarst lake. Scenario 4 is permafrost with deep groundwater within the detection limit of the SNMR measurement. Scenario 5 is an open talik below a thermokarst lake. The soundings were modeled assuming 4 % water content in permafrost and 33 % water content in talik. This figure was reproduced with permission from Parsekian et al. (2013)

6.2 Comparison of SNMR and BNMR Data

Until recently, SNMR measurements were compared to lab-NMR measurements to 'ground truth' SNMR data. However, such comparisons are of limited use because of a number of

factors including sample size and magnetic field strength. However, in more recent studies, SNMR data have been compared to BNMR data, which is sensitive to a larger sample volume than lab-NMR. With some modification of the BNMR relaxation times, such work has shown that SNMR relaxation times compare favorably with BNMR relaxation measurements and ultimately provide estimates of hydraulic conductivity. For instance, by taking into account variation in the background magnetic field, Grunewald et al. (2014) found that SNMR measurements of T_2 were comparable to BNMR measurements of T_2. In an earlier study, Müller-Petke et al. (2011b) also compared SNMR and BNMR data; by simplifying the BNMR water content models presented in this study, i.e., clipping the early-recorded part of the BNMR data and averaging vertical resolution of BNMR to obtain a blocky structure, they found that the SNMR QT-inverted model was in good agreement with the BNMR data. Here, we present a study by Knight et al. (2012) in which SNMR measurements were compared to BNMR measurements to characterize the High Plains Aquifer in the central USA.

Knight et al. (2012) presented a field experiment to develop an understanding of the physics underlying the SNMR relaxation parameter T_2^* and to improve the link between T_2^* and hydraulic conductivity of the geologic formation. By quantitatively comparing T_2^* data obtained with SNMR measurements to T_2 data obtained with BNMR measurements collected with both the MR Scanner and the Javelin, Knight et al. were able to ground truth the SNMR data. As shown in Fig. 15a, clear differences were observed when comparing the SNMR mean log T_2^* ($T_{2\mathrm{ML}}^*$; black line) and BNMR mean log T_2 data ($T_{2\mathrm{ML}}$; magenta line) from both tools. Two main factors were considered to explain the differences. The first was the instrument dead time. For the SNMR measurements, the instrument dead time was approximately 10 ms, whereas the echo time for the BNMR measurements was 1.0 ms for the MR Scanner and 2.5 ms for the Javelin. Therefore, in the presence of geologic units with T_2 values less than $\sim$10 ms (like the top part of the left panel in Fig. 15a), the SNMR T_2^* values can be greater than T_2 values measured by BNMR due to the lack of information from the early-time data. In order to account for the instrument dead time, the early part of the BNMR data was clipped. The second factor was the effect of inhomogeneities in the static magnetic field (discussed in Sect. 2.1) on SNMR relaxation time. When the $T_{2\mathrm{IH}}^{-1}$ term is significant relative to the $T_{2\mathrm{S}}^{-1}$ term in Eq. (5), T_2^* will decrease relative to T_2 in geologic units like the sand/gravel section in Fig. 15. To account for this second difference, magnetic field variations with depth in the borehole were measured using a magnetometer from which the $T_{2\mathrm{IH}}^{-1}$ term was obtained using Eq. (16). The BNMR data were then transformed to so-called pseudo-T_2^* data. After these considerations, the difference between SNMR T_2^* and BNMR pseudo-T_2^* data was considerably reduced (see Fig. 15b). The authors concluded that the two identified factors are primarily responsible for determining the relation between SNMR T_2^* and BMR T_2.

7 Conclusions and Outlook

In this paper, the principles and applications of the NMR technique for characterizing near-surface materials and environments were reviewed. The basic theory of NMR in porous media and its applications using the laboratory, borehole, and field technologies are described. The breakthrough developments in lab-NMR, BNMR, and SNMR were presented, and the challenges faced at each measurement scale were highlighted. To the best of the authors' knowledge, this paper covers the most current and advanced NMR research studies.

The high-level research activities carried out in the near-surface NMR community during the past two decades have moved the method from being a tool that shows promise

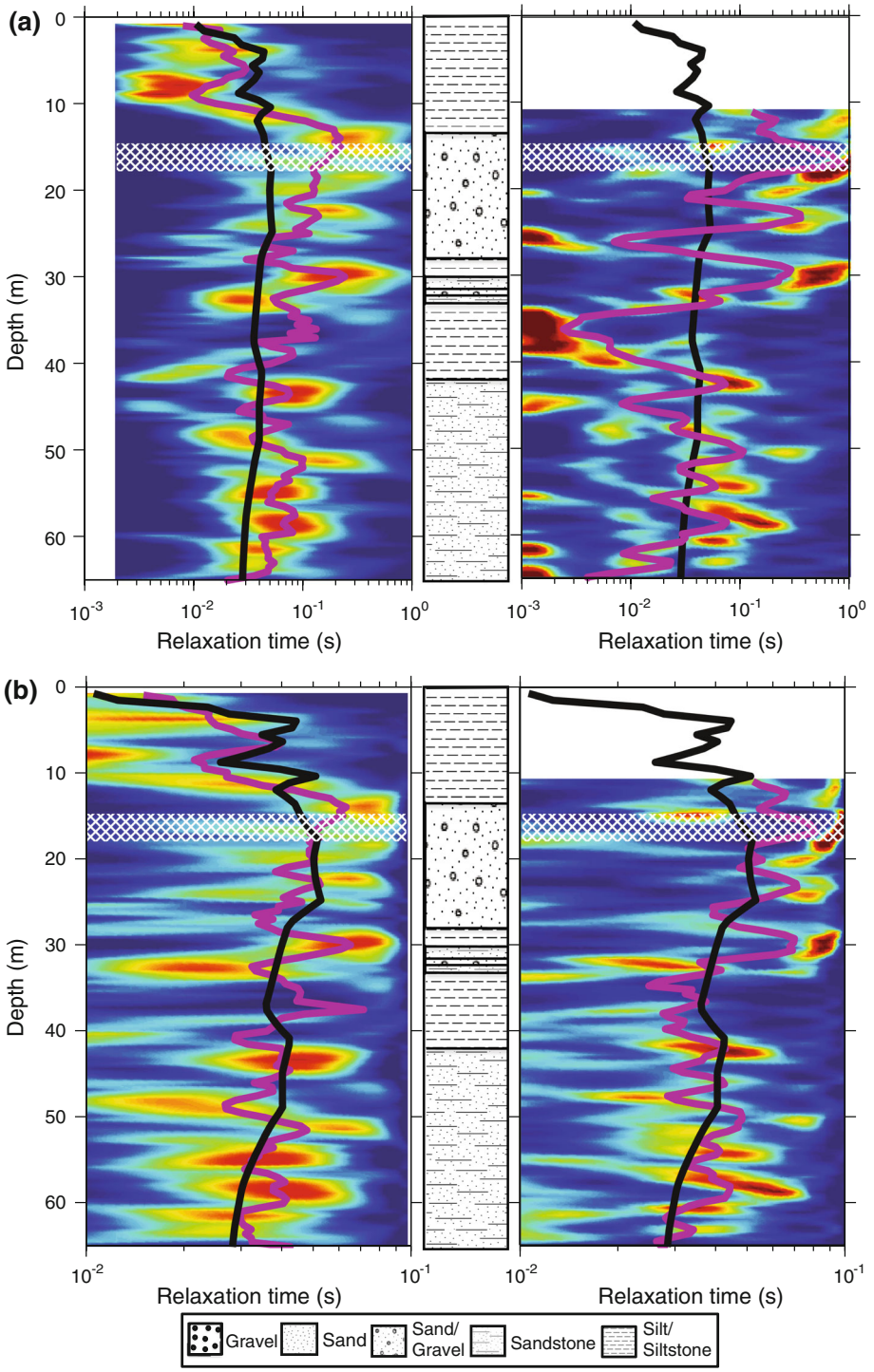
(a)
Depth (m)
0
10
20
30
40
50
60
10^{-3}
10^{-2}
10^{-1}
10^{0}
Relaxation time (s)
10^{-3}
10^{-2}
10^{-1}
10^{0}
Relaxation time (s)
(b)
Depth (m)
0
10
20
30
40
50
60
10^{-2}
10^{-1}
Relaxation time (s)
10^{-2}
10^{-1}
Relaxation time (s)
Gravel
Sand
Sand/ Gravel
Sandstone
Silt/ Siltstone

◀**Fig. 15** **a** Javelin (*left*) and MR scanner (*right*) T_2 measurements and the lithologic log (*middle*). *Colors* represent the T_2 distribution at each depth interval with warm colors corresponding to high amplitudes. The *magenta* and *black lines* represent SNMR T^*_{2ML} and BNMR T_{2ML}, respectively. Due to some restrictions, the MRS scanner data in the upper 12 m were not obtained. **b** Javelin (*left*) and MR scanner (*right*) pseudo-T^*_2 values and the lithologic log (*middle*). Again, warm colors correspond to high amplitudes. The *magenta* and *black lines* represent SNMR T^*_{2ML} and BNMR pseudo-T^*_{2ML}, respectively. *Note* the difference in the time axis. This figure was reproduced with permission from Knight et al. (2012)

as a method for characterizing near-surface environments to a proven and accepted method in near-surface geophysics. However, there is still a need for research to overcome the current limitations of NMR experiments and to expand the current use of NMR. Here, key research topics that need to be investigated are highlighted.

Recommendations for lab-NMR and to improve petrophysical relations:

1. *Improve NMR estimates of hydraulic conductivity*. As discussed in Sect. 3.4, even in case when T_1 or T_2 measurements are collected in a homogeneous static magnetic field, uncertainty associated with the value of $\rho_{1,2}$ can lead to inaccurate estimates of the hydraulic conductivity. Additionally, in aquifer material where large pores would be expected, relaxation can occur outside the fast diffusion regime leading to incorrect hydraulic conductivity models. Recent research has focused on including relaxation outside the fast diffusion regime in hydraulic conductivity models and on determining a robust hydraulic conductivity model that does not need calibration, more work is clearly needed to improve our current understanding of the link between NMR relaxation times and the hydraulic conductivity.
2. *Improve NMR estimates of vadose zone parameters*. While it is well known that NMR measurements can be used to determine the water content of unsaturated soils, only recently have studies focused on understanding the link between vadose zone parameters, i.e., the water retention curve, the matrix potential, and the unsaturated hydraulic conductivity, and NMR relaxation times. The development of new equipment that is sensitive to the low signals in the vadose zone and capable of high-resolution measurements in the top 1–5 m of the subsurface has made this a crucial time to develop these models. As with NMR estimates of hydraulic conductivity, in developing robust models for estimating vadose zone parameters, it will be paramount to understand the role of $\rho_{1,2}$ and the relaxation regime.

Recommendations for improving BNMR measurements:

1. *Reduce the minimum echo time*. As with the dead time, long echo times used by near-surface BNMR instruments can mean that fast decaying signals are not captured with the instrument. This in turn can mean that signals from fine materials, i.e., clays, are not captured in the measurement. Although the echo times of the BNMR measurements (on the order of 1–2 ms) are much shorter than the dead time of the SNMR instruments (on the order of 5–40 ms), they are still much longer than those of laboratory instruments (on the order of 0.05–0.1 ms).
2. *Develop NMR relaxation time measurements to monitor contaminant remediation*. Recent laboratory studies have demonstrated that NMR relaxation times are sensitive to changes in the iron redox conditions associated with contaminant remediation and are sensitive to changes in the redox state of contaminants such as uranium. The link between NMR measurements and mineralogy indicates that NMR has the potential to monitor in situ contaminant remediation. However, what is not yet known is whether these measurements can be directly transferred to the field and extensive field testing is

still needed before NMR can be fully realized as a tool for monitoring in situ contaminant remediation.

Recommendations for improving SNMR measurements:

1. *Enhance the signal-to-noise ratio*. The weak signal-to-noise ratio often encountered in SNMR measurements, due to low signal and/or high noise has been one of the main obstacles preventing the widespread use of SNMR measurements because it makes measurements in many places of interest unobtainable. Collecting data using a figure-eight loop configuration is a common approach that reduces noise, but is a technique that, as mentioned in the text, limits the depth of investigation. Recent studies have shown promising breakthroughs in signal processing that may enable SNMR data to be collected in more places of interest using the square or circular loop configurations with higher depths of investigation. Continuous development of signal processing schemes will help to expand the use and applicability of SNMR.
2. *Reduce the effective measurement dead time*. One of the main limitations of SNMR measurements, when compared to either lab-NMR or BNMR measurements, is the long effective dead time, which makes it difficult, and in some places impossible, to record a SNMR signal from fine geologic units. Great efforts have been made in instrument development to reduce the effective dead time by reducing both the instrument dead time (currently less than or equal to 5 ms for the GMR and 20 ms for the NUMIS system) and the duration of energizing pulse. The latter requires stronger current emission in order to maintain the same pulse moment values. A shorter effective dead time will improve parameter estimation and enable the recording of fast decaying signals. One area currently undergoing research is the idea of building separate transmitter and receiver units, which will further help to reduce the instrument dead time.
3. *Reduce the effects of magnetic field inhomogeneities*. The sensitivity of SNMR to background magnetic field inhomogeneities limits the reliable use of petrophysical relations between the most common SNMR parameter, T_2^*, and K, especially in case of large-pore structures. Recent studies have considered this matter by introducing new pulse sequences for reducing the effect of background magnetic field inhomogeneities and obtaining direct estimates of T_2, i.e., spin echo pulse sequences or CPMG pulse sequences. Another approach is to directly collect measurements of T_1, which is not affected by inhomogeneities in the magnetic field. In areas with large magnetic field inhomogeneities, measurements of either T_2 or T_1 should complement the FID measurement when collecting SNMR data.
4. *Include the complex signal in SNMR inversion algorithms*. Various studies have shown the advantage of including complex data, rather than the amplitude of data, in the inversion of SNMR data. Including the complex signal is especially important in the presence of deep conductive layers where the imaginary part of the data contains much more information than the real part. However, information on the phase component of the signal is not yet fully understood. A full knowledge of different sources of the phase data (e.g., instrument phase) will allow inversion algorithms to be developed that account for the imaginary component arising from conductive subsurface structures and thereby improve parameter estimation.
5. *More efficient instruments and measurement techniques to improve the production rate*. SNMR has a much lower production rate than other geophysical measurements; a typical study will consist of one sounding per day. One way to improve the production rate is to use an array loop configuration (Müller-Petke 2013). By choosing appropriate transmitter and receiver loop configurations, i.e., with high resolution below the entire array loop, one can

obtain 2D investigation of the subsurface in one measurement step rather than individual sounding measurements. Another method to improve the production rate is to use an array of receivers that are distributed throughout the study area and wirelessly connected to a separate SNMR receiver system; this setup would speed up both the processing and collection of the data and consequently reduce measurement time.

Finally, it is recommended that more research be done to understand the scale dependence of NMR properties and their relation to hydrogeological parameters of interest. While SNMR has been used to provide the key property of the reservoirs, *K,* this estimate is achieved using the literature-based empirical relations developed at the laboratory scale. However, what is not yet available is a complete understanding of how the NMR and hydrogeological properties of laboratory samples, which are often collected on samples volumes of 10–100 mL, compare to SNMR measurement, which are collected on volumes of approximately 10^7 m^3. Therefore, integrating the scale of the measurement into the petrophysical relation used to predict *K* with SNMR, BNMR, and lab-NMR data are an important direction for future research.

Acknowledgments This work was carried out as part of the Danish Council of Strategic Research Project titled 'HyGEM—Integrating geophysics, geology, and hydrology for improved groundwater and environmental management'. The authors would like to thank Lee Slater for his review of an early version of the manuscript, as well as the editor and Rosemary Knight for their fruitful comments and thorough review of the manuscript. Use of product names does not indicate endorsement.

Appendix 1

See Table 3.

Table 3 Summary of acronyms

Term	Definition
NMR	Nuclear magnetic resonance
MRI	Magnetic resonance imaging
SNMR	Surface nuclear magnetic resonance; surface NMR
BNMR	Borehole nuclear magnetic resonance; borehole NMR
Lab-NMR	Laboratory NMR
EM	Electromagnetic
FID	Free induction decay
WRC	Water retention curve
MRS	Magnetic resonance sounding
RDP	Relaxation processes during the pulse
IAI	Initial amplitude inversion
TSI	Time step inversion
QTI	QT inversion
PSR	Pseudosaturation recovery measurement scheme
pcPSR	Phase-cycled pseudosaturation recovery measurement scheme
CPMG	Carr–Purcell–Meiboom–Gill pulse sequence
thk	Layer thickness (inversion model parameter)
rho	Electrical resistivity (inversion model parameter)

Appendix 2

See Table 4.

Table 4 Definition of main mathematical symbols

Symbol	Definition
f_{L}	Larmor frequency
ω_{L}	Larmor angular frequency
γ	Proton gyromagnetic ratio
$\boldsymbol{B}_0$	Static magnetic field
$\boldsymbol{B}_{\mathrm{E}}$	Earth's magnetic field
n	Number of protons per unit volume
$\hbar$	Reduced Plank's constant
T	Absolute temperature in units of Kelvin
K_{B}	Boltzmann's constant
$\boldsymbol{M}_0$	Net magnetization vector
M_0	Value of net magnetization vector
D	Self-diffusion coefficient of water
T_2	Transverse relaxation time
T_2^*	Effective transverse relaxation time
T_1	Longitudinal relaxation time
ρ_2	Transverse surface relaxivity
ρ_1	Longitudinal surface relaxivity
$T_{1,2\mathrm{B}}$	Longitudinal or transverse bulk fluid relaxation time
$T_{1,2\mathrm{S}}$	Longitudinal or transverse surface relaxation time
$T_{2\mathrm{D}}$	Diffusion relaxation time
$\boldsymbol{B}_1(t)$	Energizing magnetic field
t_{dead}	Measurement dead time
τ_{d}	Delay time, in T_1 data
τ_{p}	Energizing pulse duration
k	Permeability
K	Hydraulic conductivity
ϕ	Porosity
q	Energizing pulse moment
$\boldsymbol{r}$	Subsurface position
$\theta_T(q,\boldsymbol{r})$	Spin tip angle, dependent on pulse moment and position
$\boldsymbol{B}_{\mathrm{T}}^{\perp}$	Component of the energizing magnetic field perpendicular to the Earth's field
$\boldsymbol{B}_{\mathrm{T}}^{+}$	Corotating component of $\boldsymbol{B}_{\mathrm{T}}^{\perp}$
$\boldsymbol{B}_T^{-}$	Counter-rotating component of $\boldsymbol{B}_{\mathrm{T}}^{\perp}$
$V(q, t)$	Measured SNMR QT signal, dependent on pulse moment and time
$V(q, t_n)$	Measured SNMR TS signal, dependent on pulse moment at different time steps t_n
$W(\boldsymbol{r}, T_2^*)$	Partial water content, dependent on position and effective transverse relaxation time

Table 4 continued

Symbol	Definition
$K(q,\boldsymbol{r})$	SNMR kernel function, dependent on pulse moment and position
$E_0(q)$	SNMR sounding curve
E_0	FID initial amplitude
c	Stretching exponent (in stretched exponential model)
W	Water content

References

Allen DF et al (2000) Trends in NMR Logging. Oilfield Rev 12(3):2–19

Apitz D, Johansen PM (2005) Limitations of the stretched exponential function for describing dynamics in disordered solid materials. J Appl Phys 97:1–4

Arns CH (2004) A comparison of pore size distributions derived by NMR and X-ray-CT techniques. Phys A 339:159–165

Atekwana EA, Slater LD (2009) Biogeophysics: a new frontier in Earth science research. Rev Geophys 47:RG4004

Auken E, Pellerin L, Christensen NB, Sørensen KI (2006) A survey of current trends in near-surface electrical and electromagnetic methods. Geophysics 71:G249–G260

Auken E, Christiansen, AV, Kirkegaard C, Fiandaca G, Schamper C, Behroozmand AA, Binley A, Nielsen E, Effersø F, Christensen, NB, Sørensen KI, Foged N, Vignoli G (2014) An overview of a highly versatile forward and stable inverse algorithm for airborne, ground-based and borehole electromagnetic and electric data. Explor Geophys 1−13. doi:10.1071/EG13097

Baofeng T, Tingting L, Xiaofeng Y, Chuandong J, Jun L (2012) Joint use of adaptive notch filter and empirical mode decomposition for noise cancellation applied to MRS. 5th international meeting on magnetic resonance, Hanover

Behroozmand AA, Auken E, Fiandaca G, Christiansen AV (2012a) Improvement in MRS parameter estimation by joint and laterally constrained inversion of MRS and TEM data. Geophysics 74:WB191–WB200

Behroozmand AA, Auken E, Fiandaca G, Christiansen AV, Christensen NB (2012b) Efficient full decay inversion of MRS data with a stretched-exponential approximation of the T2* distribution. Geophys J Int 190:900–912

Behroozmand AA, Auken E, Fiandaca G (2013a) On the sensitivity analysis of separated-loop MRS data. AGU fall meeting 2013, San Francisco

Behroozmand AA, Dalgaard E, Christiansen AV, Auken E (2013b) A comprehensive study of the parameter determination in a joint MRS and TEM data analysis scheme. Near Surf Geophys 11:557–567

Bernard J (2007) Instruments and field work to measure a magnetic resonance sounding. Boletin Geologico y Minero 118:459–472

Bird NRA, Preston AR, Randall EW, Whalley WR, Whitmore AP (2005) Measurement of the size distribution of water-filled pores at different matric potentials by stray field nuclear magnetic resonance. Eur J Soil Sci 56:135–143

Bloch F (1946) Nuclear induction. Phys Rev 70:460–474

Bloembergen N, Purcell EM, Pound RV (1948) Relaxation effects in nuclear magnetic resonance absorption. Phys Rev 73:679–712

Boucher M, Favreau G, Vouillamoz JM, Nazoumou Y, Legchenko A (2009) Estimating specific yield and transmissivity with magnetic resonance sounding in an unconfined sandstone aquifer (Niger). Hydrogeol J 17:1805–1815

Braun M, Hertrich M, Yaramanci U (2005) Study on complex inversion of magnetic resonance sounding signals. Near Surf Geophys 3:155–163

Braun M, Kamm J, Yaramanci U (2009) Simultaneous inversion of magnetic resonance sounding in terms of water content, resistivity and decay times. Near Surf Geophys 7:589–598

Bray CL, Schaller NC, Iannopollo SL, Bostick MD, Ferrante G, Fleming A, Hornak JP (2006) A study of 1H NMR signal from hydrated synthetic sands. J Environ Eng Geophys 11:1–8

Brown RJS, Gamson BW (1960) Nuclear magnetism logging. Trans Am Inst Min Metall Petrol Eng 219:199–207
Brownstein KR, Tarr CE (1979) Importance of classical diffusion in NMR studies of water in biological cells. Phys Rev A 19:2446–2453
Bryar TR, Knight RJ (2002) Sensitivity of nuclear magnetic resonance relaxation measurements to changing soil redox conditions. Geophys Res Lett 29:2197–2200
Bryar TR, Knight RJ (2003) Laboratory studies of the effect of sorbed oil on proton nuclear magnetic resonance. Geophysics 68:942–948
Bryar TR, Daughney CJ, Knight RJ (2000) Paramagnetic effects of iron(III) species on nuclear magnetic relaxation of fluid protons in porous media. J Magn Reson 142:74–85
Callaghan PT, Dykstra R, Eccles CD, Haskell TG, Seymour JD (1999) A nuclear magnetic resonance study of Antarctic sea ice brine diffusivity. Cold Reg Sci Technol 29:153–171
Carr HY, Purcell EM (1954) Effects of diffusion on free precession in nuclear magnetic resonance experiments. Phys Rev 94:630–638
Chalikakis K, Nielsen MR, Legchenko A (2008) MRS applicability for a study of glacial sedimentary aquifers in Central Jutland, Denmark. J Appl Geophys 66:176–187
Chalikakis K, Nielsen MR, Legchenko A, Hagensen TF (2009) Investigation of sedimentary aquifers in Denmark using the magnetic resonance sounding method (MRS). Comptes Rendus Geosci 341:918–927
Chalikakis K, Plagnes V, Guerin R, Valois R, Bosch FP (2011) Contribution of geophysical methods to karst-system exploration: an overview. Hydrogeol J 19:1169–1180
Chang D, Ioannidis MA (2002) Magnetization evolution in network models of porous rock under conditions of drainage and imbibition. J Colloid Interface Sci 253:159–170
Chen RS, Stallworth PE, Greenbaum SG, Kleinberg RL (1994) Effects of hydrostatic pressure on proton and deuteron magnetic resonance of water in natural rock and artificial porous media. J Magn Reson, Ser A 110:77–81
Chen Q, Marble AE, Colpitts BG, Balcom BJ (2005) The internal magnetic field distribution, and single exponential magnetic resonance free induction decay, in rocks. J Magn Reson 175:300–308
Chevalier AC, Legchenko A, Descloitres M, Guyard H, Vincent C, Garambois S (2011) 3D Monte Carlo inversion of surface magnetic resonance measurements EAGE 2011, Leicester
Coates GR, Dumanoir JL (1974) New approach to improved log-derived permeability. Log Anal 15:17–31
Coates GR, Xiao L, Prammer G (1999) NMR logging principles and applications. Haliburton Energy Services, Houston
Codd SL, Vogt SJ, Hornemann JA, Phillips AJ, Maneval JE, Romanenko KR, Hansen L, Cunningham AB, Seymour JD (2011) NMR relaxation measurements of biofouling in model and geological porous media. Org Geochem 42:965–971
Costabel S (2011) Nuclear magnetic resonance on laboratory and field scale for estimating hydraulic parameters in the vadose zone. Technical University of Berlin, Berlin
Costabel S, Günther T (2012) Direct inversion for water retention parameters from MRS measurements in the saturated/unsaturated zone—a sensitivity study 5th international meeting on magnetic resonance. Hannover
Costabel S, Müller-Petke M (2012a) Identification and elimination of spiky noise features in MRS data 5th international meeting on magnetic resonance, Hanover
Costabel S, Müller-Petke M (2012b) MRS noise investigations with focus on optimizing the measurement setup in the field 5th international meeting on magnetic resonance. Hanover
Costabel S, Müller-Petke M (2014) Despiking of magnetic resonance signals in time and wavelet domains. Near Surf Geophys 12:185–197
Costabel S, Yaramanci U (2011a) Relative hydraulic conductivity and effective saturation from Earth's field nuclear magnetic resonance a method for assessing the vadose zone. Near Surf Geophys 9:155–167
Costabel S, Yaramanci U (2011b) Relative hydraulic conductivity in the vadose zone from magnetic resonance sounding—Brooks–Corey parameterization of the capillary fringe. Geophysics 76:G61–G71
Dalgaard E, Auken E, Larsen JJ (2012) Adaptive noise cancelling of multichannel magnetic resonance sounding signals. Geophys J Int 191:88–100
Dalgaard E, Auken E, Müller-Petke M (2013) Optimized distribution Of SNMR pulse moments and field efficiency evaluated using a model uncertainty analysis symposium on the application of geophysics to engineering and environmental problems. SAGEEP, Denver
Daughney CJ, Bryar TR, Knight RJ (2000) Detecting sorbed hydrocarbons in a porous medium using proton nuclear magnetic resonance. Environ Sci Technol 34:332–337
Davis A, Macnae J (2012) Modelling NMR signal for compact sensors 5th international meeting on magnetic resonance. Hannover

Davis AC, Dlugosch R, Queitsch M, Macnae JC, Stolz R, Müller-Petke M (2014) First evidence of detecting surface nuclear magnetic resonance signals using a compact B-field sensor. Geophys Res Lett 41:4222–4229

Dlubac K, Knight R, Song YQ, Bachman N, Grau B, Cannia J, Williams J (2013) Use of NMR logging to obtain estimates of hydraulic conductivity in the high plains aquifer, Nebraska, USA. Water Resour Res 49:1871–1886

Dlubac K, Knight R, Keating K (2014) A numerical study of the relationship between NMR relaxation and permeability in sands and gravels. Near Surf Geophys 12:219–230

Dlugosch R, Müller-Petke M, Günther T, Costabel S, Yaramanci U (2011) Assessment of the potential of a new generation of surface nuclear magnetic resonance instruments. Near Surf Geophys 9:89–102

Dlugosch R, Günther T, Müller-Petke M, Yaramanci U (2012) A general model for predicting hydraulic conductivity of unconsolidated material using nuclear magnetic resonance 5th international meeting on magnetic resonance. Hannover

Dlugosch R, Günther T, Müller-Petke M, Yaramanci U (2013) 2D Qt-inversion to investigate spatial variations of hydraulic conductivity using SNMR symposium on the application of geophyics to engineering and environmental problems. SAGEEP, Denver

Dlugosch R, Günther T, Müller-Petke M, Yaramanci U (2014) Two-dimensional distribution of relaxation time and water content from surface nuclear magnetic resonance. Near Surf Geophys 12:231–241

D'Orazio F, Bhattacharja S, Halperin WP, Eguchi K, Mizusaki T (1990) Molecular diffusion and nuclear-magnetic-resonance relaxation of water in unsaturated porous silica glass. Phys Rev B 42:9810–9818

Dunn KJ, Bergman DJ, Latorraca GA (2002a) Nuclear magnetic resonance—petrophysical and logging applications. Elsevier, Amsterdam

Dunn KJ, Bergman DJ, Latorraca GA (2002b) Nuclear magnetic resonance—petrophysical and logging applications. Elsevier Science, Kidligton, pp 1–30

Everett ME (2012) Theoretical developments in electromagnetic induction geophysics with selected applications in the near surface. Surv Geophys 33:29–63

Fantazzini P, Brown RJS (2005) Initially linear echo-spacing dependence of 1/T2 measurements in many porous media with pore-scale inhomogeneous fields. J Magn Reson 177:228–235

Fleury M, Kohler E, Norrant F, Gautier S, M'Hamdi J, Barre L (2013) Characterization and quantification of water in smectites with low-field NMR. J Phys Chem C 117:4551–4560

Foley I, Farooqui SA, Kleinberg RL (1996) Effect of paramagnetic ions on nmr relaxation of fluids at solid surfaces. J Magn Reson, Ser A 123:95–104

Freedman R (2006) Advances in NMR logging. J Petrol Technol 58:60–66

Gev I, Goldman M, Rabinovich B, Rabinovich M, Issar A (1996) Detection of the water level in fractured phreatic aquifers using nuclear magnetic resonance (NMR) geophysical measurements. J Appl Geophys 34:277–282

Girard JF, Legchenko A, Boucher M (2005) Stability of MRS signal and estimation of data quality. Near Surf Geophys 3:187–194

Godefroy S, Korb JP, Fleury M, Bryant RG (2001) Surface nuclear magnetic relaxation and dynamics of water and oil in macroporous media. Phys Rev E Stat Nonlinear Soft Matter Phys 64:216051–2160513

Goldman M, Rabinovich B, Rabinovich M, Gilad D, Gev I, Schirov M (1994) Application of the integrated NMR-TDEM method in groundwater exploration in Israel. J Appl Geophys 31:27–52

Grombacher D, Walbrecker JO, Knight R (2012) Quantifying background magnetic field inhomogeneity using composite pulses: estimating T2 from T2* by correcting for static dephasing 5th international meeting on magnetic resonance. Hannover

Grunewald E, Knight R (2009) A laboratory study of NMR relaxation times and pore coupling in heterogeneous media. Geophysics 74:E215–E221

Grunewald E, Knight R (2011a) A laboratory study of NMR relaxation times in unconsolidated heterogeneous sediments. Geophysics 76:G73–G83

Grunewald E, Knight R (2011b) The effect of pore size and magnetic susceptibility on the surface NMR relaxation parameter T*2. Near Surf Geophys 9:169–178

Grunewald E, Knight R (2012) Nonexponential decay of the surface-NMR signal and implications for water content estimation. Geophysics 77:EN1–EN9

Grunewald E, Walsh D (2012) Novel surface-NMR pulse sequences for improved estimation of relaxation times and hydrogeologic properties 5th international meeting on magnetic resonance. Hannover

Grunewald E, Walsh D (2013) Multiecho scheme advances surface NMR for aquifer characterization. Geophys Res Lett 40:GL057607

Grunewald E, Knight R, Walsh D (2014) Advancement and validation of surface NMR spin echo measurements of T2 . Geophysics 79:EN15–EN23

Guillen A, Legchenko A (2002) Application of linear programming techniques to the inversion of proton magnetic resonance measurements for water prospecting from the surface. J Appl Geophys 50:149–162
Günther T, Müller-Petke M (2012) Hydraulic properties at the North Sea island Borkum derived from joint inversion of magnetic resonance and electrical resistivity soundings. Hydrol Earth Syst Sci Discuss 9:2797–2829
Hahn EL (1950) Spin echoes. Phys Rev 80:580–594
Hedberg SA, Knight RJ, MacKay AL, Whittall KP (1993) The use of nuclear magnetic resonance for studying and detecting hydrocarbon contaminants in porous rocks. Water Resour Res 29:1163–1170
Hertrich M (2008) Imaging of groundwater with nuclear magnetic resonance. Prog Nucl Magn Reson Spectrosc 53:227–248
Hertrich M, Braun M, Yaramanci U (2005) Magnetic resonance soundings with separated transmitter and receiver loops. Near Surf Geophys 3:141–154
Hertrich M, Braun M, Günther T, Green AG, Yaramanci U (2007) Surface nuclear magnetic resonance tomography. IEEE Trans Geosci Remote Sens 45:3752–3759
Hinedi ZR, Kabala ZJ, Skaggs TH, Borchardt DB, Lee RWK, Chang AC (1993) Probing soil and aquifer material porosity with nuclear magnetic resonance. Water Resour Res 29:3861–3866
Hinedi ZR, Chang AC, Anderson MA, Borchardt DB (1997) Quantification of microporosity by nuclear magnetic resonance relaxation of water imbibed in porous media. Water Resour Res 33:2697–2704
Hunter D, Kepic A (2005) Surface nuclear magnetic resonance signal contribution in conductive terrains. Explor Geophys 36:73–77
Ioannidis MA, Chatzis I, Lemaire C, Perunarkilli R (2006) Unsaturated hydraulic conductivity from nuclear magnetic resonance measurements. Water Resour Res 42. doi:10.1029/2006WR004955
Irons T, Yaoguo L, McKenna JR (2010) Frequency domain surface nuclear magnetic resonance forward modeling on an adaptive octree mesh 2010 SEG annual meeting. Denver, Colorado
Irons T, Li Y, Abraham J, McKenna JR (2012) The case for comprehensive frequency-domain inversion of surface NMR data 5th international meeting on magnetic resonance. Hannover
Irons T, Martin K, Finn C, Bloss B, Horton R (2014) Using nuclear magnetic resonance and transient electromagnetics to characterise water distribution beneath an ice covered volcanic crater: the case of Sherman Crater Mt. Baker, Washington. Near Surf Geophys 12:285–296
Istratov AA, Vyvenko OF (1999) Exponential analysis in physical phenomena. Rev Sci Instrum 70:1233
Jaeger F, Grohmann E, Schaumann G (2006) 1H NMR relaxometry in natural humous soil samples: insights in microbial effects on relaxation time distributions. Plant Soil 280:209–222
Jaeger F, Rudolph N, Lang F, Schaumann G (2008) Effects of soil solution's constituents on proton NMR relaxometry of soil samples. Soil Sci Soc Am J 72:1694–1707
Jaeger F, Bowe S, Van As H, Schaumann GE (2009) Evaluation of 1H NMR relaxometry for the assessment of pore-size distribution in soil samples. Eur J Soil Sci 60:1052–1064
Jiang C, Lin J, Duan Q, Sun S, Tian B (2011) Statistical stacking and adaptive notch filter to remove high-level electromagnetic noise from MRS measurements. Near Surf Geophys 9:459–468
Johnson CD, Keating K, Walsh DO, Lane JW, Falzone S (2012) Use of borehole and surface nuclear magnetic resonance methods at Haddam Meadows State Park, Connecticut symposium on the application of geophysics to engineering and environmental problems. Tucson, Arizona
Katz AJ, Thompson AH (1986) Quantitative prediction of permeability in porous rock. Phys Rev B 34:8179–8181
Keating K, Falzone S (2013) Relating nuclear magnetic resonance relaxation time distributions to void-size distributions for unconsolidated sand packs. Geophysics 78:D461–D472
Keating K, Knight R (2007) A laboratory study to determine the effect of iron oxides on proton NMR measurements. Geophysics 72:E27–E32
Keating K, Knight R (2008) A laboratory study of the effect of magnetite on NMR relaxation rates. J Appl Geophys 66:188–196
Keating K, Knight R (2010) A laboratory study of the effect of Fe(II)-bearing minerals on nuclear magnetic resonance (NMR) relaxation measurements. Geophysics 75:XF71–XF82
Keating K, Knight R (2012) The effect of spatial variation in surface relaxivity on nuclear magnetic resonance relaxation rates. Geophysics 77:E365–E377
Keating K, Knight R, Tufano KJ (2008) Nuclear magnetic resonance relaxation measurements as a means of monitoring iron mineralization processes. Geophys Res Lett 35. doi:10.1029/2008GL035225
Kenyon WE, Day PI, Straley C, Willemsen JF (1988) Three-part study of NMR longitudinal relaxation properties of water-saturated sandstones. SPE Form Eval 3:622–636
Kleinberg RL, Griffin DD (2005) NMR measurements of permafrost: unfrozen water assay, pore-scale distribution of ice, and hydraulic permeability of sediments. Cold Reg Sci Technol 42:63–77

Kleinberg RL, Horsfield MA (1990) Transverse relaxation processes in porous sedimentary rock (1969). J Magn Reson 88:9–19
Kleinberg RL, Jackson JA (2001) An introduction to the history of NMR well logging. Concepts Magn Reson 13:340–342
Kleinberg RL, Kenyon WE, Mitra PP (1994) Mechanism of NMR relaxation of fluids in rock. J Magn Reson, Ser A 108:206–214
Knight R, Grunewald E, Irons T, Dlubac K, Song Y, Bachman HN, Grau B, Walsh DO, Abraham J, Cannia JC (2012) Field experiment provides ground truth for surface nuclear magnetic resonance measurement. Geophys Res Lett 39. doi:10.1029/2011GL050167
Lachassagne P, Baltassat JM, Legchenko A, de Gramont HM (2005) The links between MRS parameters and the hydrogeological parameters. Near Surf Geophys 3:259–265
Lange G, Yaramanci U, Meyer R (2007) Surface nuclear magnetic resonance in environmental geology. Springer, Berlin
Larsen JJ, Dalgaard E, Auken E (2014) Noise cancelling of MRS signals combining model-based removal of powerline harmonics and multichannel Wiener filtering. Geophys J Int 196:828–836. doi:10.1093/gji/ggt422
Legchenko A (2004) Magnetic resonance sounding: Enhanced modeling of a phase shift. Appl Magn Reson 25:621–636
Legchenko AV, Shushakov OA (1998) Inversion of surface NMR data. Geophysics 63:75–84
Legchenko A, Valla P (1998) Processing of surface proton magnetic resonance signals using non-linear fitting. J Appl Geophys 39:77–83
Legchenko A, Valla P (2002) A review of the basic principles for proton magnetic resonance sounding measurements. J Appl Geophys 50:3–19
Legchenko A, Valla P (2003) Removal of power-line harmonics from proton magnetic resonance measurements. J Appl Geophys 53:103–120
Legchenko A, Baltassat JM, Beauce A, Bernard J (2002) Nuclear magnetic resonance as a geophysical tool for hydrogeologists. J Appl Geophys 50:21–46
Legchenko A, Baltassat JM, Bobachev A, Martin C, Robain H, Vouillamoz JM (2004) Magnetic resonance sounding applied to aquifer characterization. Ground Water 42:363–373
Legchenko A, Descloitres M, Bost A, Ruiz L, Reddy M, Girard JF, Sekhar M, Kumar MSM, Braun JJ (2006) Resolution of MRS applied to the characterization of hard-rock aquifers. Ground Water 44:547–554
Legchenko A, Ezersky M, Girard JF, Baltassat JM, Boucher M, Camerlynck C, Al-Zoubi A (2008) Interpretation of magnetic resonance soundings in rocks with high electrical conductivity. J Appl Geophys 66:118–127
Legchenko A, Vouillamoz J, Roy J (2010) Application of the magnetic resonance sounding method to the investigation of aquifers in the presence of magnetic materials. Geophysics 75:L91–L100
Legchenko A, Descloitres M, Vincent C, Guyard H, Garambois S, Chalikakis K, Ezersky M (2011) Three-dimensional magnetic resonance imaging for groundwater. New J Phys 13. doi:10.1088/1367-2630/13/2/025022
Lehmann-Horn JA, Hertrich M, Greenhalgh SA, Green AG (2011a) Three-dimensional magnetic field and nmr sensitivity computations incorporating conductivity anomalies and variable-surface topography. IEEE Trans Geosci Remote Sens 49:3878–3891
Lehmann-Horn JA, Walbrecker JO, Hertrich M, Langston G, McClymont AF, Green AG (2011b) Imaging groundwater beneath a rugged proglacial moraine. Geophysics 76:B165–B172
Lehmann-Horn JA, Hertrich M, Greenhalgh SA, Green AG (2012) On the sensitivity of surface NMR in the presence of electrical conductivity anomalies. Geophys J Int 189:331–342
Levitt MH (2006) Spin dynamics: basics of nuclear magnetic resonance. Wiley, Chichester
Lubczynski M, Roy J (2003) Hydrogeological interpretation and potential of the new magnetic resonance sounding (MRS) method. J Hydrol 283:19–40
Maliva R, Clayton E, Missimer T (2009) Application of advanced borehole geophysical logging to managed aquifer recharge investigations. Hydrogeol J 17:1547–1556
Mattea C, Kimmich R, Ardelean I, Wonorahardjo S, Farrher G (2004) Molecular exchange dynamics in partially filled microscale and nanoscale pores of silica glasses studied by field-cycling nuclear magnetic resonance relaxometry. J Chem Phys 121:10648–10656
Megawati M, Madland MV, Hiorth A (2012) Probing pore characteristics of deformed chalk by NMR relaxation. J Petrol Sci Eng 100:123–130
Meiboom S, Gill D (1958) Modified spin-echo method for measuring nuclear relaxation times. Rev Sci Instrum 29:688–691

Meju MA, Denton P, Fenning P (2002) Surface NMR sounding and inversion to detect groundwater in key aquifers in England: comparisons with VES-TEM methods. J Appl Geophys 50:95–111
Minsley BJ, Abraham JD, Smith BD, Cannia JC, Voss CI, Jorgenson MT, Walvoord MA, Wylie BK, Anderson L, Ball LB, Szcz-Pan M, Wellman TP, Ager TA (2012) Airborne electromagnetic imaging of discontinuous permafrost. Geophys Res Lett 39:2503
Mitreiter I, Oswald SE, Stallmach F (2010) Investigation of iron(III)-release in the pore water of natural sands by NMR relaxometry. Open Magn Reson J 3:46–51
Mohnke O, Yaramanci U (2002) Smooth and block inversion of surface NMR amplitudes and decay times using simulated annealing. J Appl Geophys 50:163–177
Mohnke O, Yaramanci U (2005) Forward modeling and inversion of MRS relaxation signals using multi-exponential decomposition. Near Surf Geophys 3:165–185
Mohnke O, Yaramanci U (2008) Pore size distributions and hydraulic conductivities of rocks derived from magnetic resonance sounding relaxation data using multi-exponential decay time inversion. J Appl Geophys 66:73–81
Müller M, Kooman S, Yaramanci U (2005) Nuclear magnetic resonance (NMR) properties of unconsolidated sediments in field and laboratory. Near Surf Geophys 3:275–285
Müller-Petke M (2013) Resolution studies for 2D magnetic resonance tomography (MRT) using array loop configuration symposium on the application of geophyics to engineering and environmental problems. SAGEEP, Denver
Müller-Petke M, Costabel S (2012) A comparison of harmonic noise cancellation concepts 5th international meeting on magnetic resonance. Hanover
Müller-Petke M, Costabel S (2014) Comparison and optimal parameter setting of reference-based harmonic noise cancellation in time and frequency domain for surface-NMR. Near Surf Geophys 12:199–210
Müller-Petke M, Walbrecker JO (2012) Inversion of T1 relaxation times based on pcPSR measurements—synthetic examples 5th international meeting on magnetic resonance. Hanover
Müller-Petke M, Yaramanci U (2008) Resolution studies for magnetic resonance sounding (MRS) using the singular value decomposition. J Appl Geophys 66:165–175
Müller-Petke M, Yaramanci U (2010a) Improving the signal-to-noise ratio of surface-NMR measurements by reference channel based noise cancellation 16th European meeting of environmental and engineering geophysics. Zürich
Müller-Petke M, Yaramanci U (2010b) QT inversion—comprehensive use of the complete surface NMR data set. Geophysics 75:WA199–WA209
Müller-Petke M, Yaramanci U (2011) Noise cancellation for surface NMR—application of time and frequency domain approaches 17th European meeting of environmental and engineering geophysics. Leicester
Müller-Petke M, Dlugosch R, Yaramanci U (2011a) Evaluation of surface nuclear magnetic resonance-estimated subsurface water content. New J Phys 13. doi:10.1088/1367-2630/13/9/095002
Müller-Petke M, Hiller T, Herrmann R, Yaramanci U (2011b) Reliability and limitations of surface NMR assessed by comparison to borehole NMR. Near Surf Geophys 9:123–124
Müller-Petke M, Walbrecker JO, Knight R (2013) The inversion of surface-NMR T1 data for improved aquifer characterization. Geophysics 78:EN83–EN94
Naudet V, Revil A, Bottero JY, Be'gassat P (2003) Relationship between self-potential (SP) signals and redox conditions in contaminated groundwater. Geophys Res Lett 30:2091
Neyer FM (2010) Processing of full time series, multichannel surface NMR signals master thesis. ETH Zurich
Neyer FM, Hertrich M, Greenhalgh SA (2010) Innovative surface NMR signal processing to significantly improve data quality, AGU fall meeting. San Fransisco, USA
Nishimura D (2010) Principles of magnetic resonance imaging. Stanford University, Stanford
Parsekian AD, Grosse G, Walbrecker JO, Müller-Petke M, Keating K, Liu L, Jones BM, Knight R (2013) Detecting unfrozen sediments below thermokarst lakes with surface nuclear magnetic resonance. Geophys Res Lett 40:535–540
Parsekian AD, Dlubac K, Grunewald E, Knight R, Walsh DO (2014) Bootstrap calibration of downhole nuclear magnetic resonance hydraulic conductivity estimates in an unconsolidated aquifer. Ground Water. doi:10.1111/gwat.12165
Perlo J, Danieli E, Perlo J, Blümich B, Casanova F (2013) Optimized slim-line logging NMR tool to measure soil moisture in situ. J Magn Reson 233:74–79
Perttu N, Wattanasen K, Phommasone K, Elming SÅ (2011) Characterization of aquifers in the Vientiane Basin, Laos, using magnetic resonance sounding and vertical electrical sounding. J Appl Geophys 73:207–220

Peyron M, Pierens GK, Lucas AJ, Hall LD, Stewart RC (1996) The modified stretched-exponential model for characterization of NMR relaxation in porous media. J Magn Reson, Ser A 118:214–220
Plata JL, Rubio FM (2008) The use of MRS in the determination of hydraulic transmissivity: the case of alluvial aquifers. J Appl Geophys 66:128–139
Pohlmeier A, Haber-Pohlmeier S, Stapf S (2009) A fast field cycling nuclear magnetic resonance relaxometry study of natural soils. Vadose Zone J 8:735–742
Radic T (2005) Mobile instrument for NMR measurements on samples in the earth's magnetic field. In: Proceedings of the 11th annual meeting, environmental and engineering geophysics, pp P034
Ramakrishnan TS, Schwartz LM, Fordham E (1999) Forward models for nuclear magnetic resonance in carbonate rocks: log analyst
Roy J, Lubczynski M (2005) MRS multi-exponential decay analysis: aquifer pore-size distribution and vadose zone characterization. Near Surf Geophys 3:287–298
Roy J, Rouleau A, Chouteau M, Bureau M (2008) Widespread occurrence of aquifers currently undetectable with the MRS technique in the Grenville geological province, Canada. J Appl Geophys 66:82–93
Ryu S (2009) Effect of inhomogeneous surface relaxivity, pore geometry and internal field gradients on NMR logging: exact and perturbative theories and numerical investigations society of petrophysicists and well log analysts 50th annual logging symposium
Sanderlin AB, Vogt SJ, Grunewald E, Bergin A, Codd SL (2013) Biofilm detection in natural unconsolidated porous media using a low-field magnetic resonance system. Environ Sci Technol 47:987–992
Schirov MD, Rojkowski AD (2002a) On the accuracy of parameters determination from SNMR measurements. J Appl Geophys 50:207–216
Schirov MD, Rojkowski AD (2002b) On the accuracy of parameters determination from SNMR measurements. J Appl Geophys 50:207–216
Schirov MD, Legchenko A, Creer G (1991) A new non-invasive groundwater detection technology for Australia. Explor Geophys 22:333–338
Schirov M, Gjulumjanz O, Rojkowski AD (1999) AQUATOM equipment for mapping underground waters from the terrigenous carbonaceous reservoirs of the Republic of Tatarstan 1st workshop on surface nuclear magnetic resonance (SNMR)—What is possible? Berlin
Seevers DO (1966) A nuclear magnetic method for determining the permeability of sandstones: 33rd annual logging symposium, society of professional well log analysts, transactions, paper L
Semenov AG (1987) NMR Hydroscope for water prospecting. In: Proceedings of the seminar on geotomography. Indian Geophysical Union, Hyderabad, pp 66−67
Semenov AG, Pusep AJ, Schirov MD (1982) Hydroscope—an installation for prospecting without drilling (in Russian). USSR Academic Science, Novosibirsk, pp 1−26
Semenov AG, Burshtein AI, Pusep AJ, Schirov MD (1988) A device for measurement of underground mineral prospecting. USSR patent 1079063
Sen PN, Straley C, Kenyon WE, Whittingham MS (1990) Surface-to-volume ratio, charge density, nuclear magnetic relaxation, and permeability in clay-bearing sandstones. Geophysics 55:61–69
Senturia SD, Robinson JD (1970) Nuclear spin-lattice relaxation of liquids confined in porous solids. Soc Petrol Eng J 10:237–244
Shushakov OA (1996) Surface NMR measurement of proton relaxation times in medium to coarse-grained sand aquifer. Magn Reson Imaging 14:959–960
Shushakov OA, Legchenko AV (1994) Groundwater proton magnetic resonance in the horizontally stratified media of different electrical conductivity. Geol Geophys 35:140–145
Simpson JH, Carr HY (1958) Diffusion and nuclear spin relaxation in water. Phys Rev 111:1201–1202
Slater L (2007) Near surface electrical characterization of hydraulic conductivity: from petrophysical properties to aquifer geometries—a review. Surv Geophys 28:169–197
Soltani R, Xiao L (2012) Higher-order statistical signal processing for surface-NMR electronic instruments 5th international meeting on magnetic resonance. Hanover
Song YQ (2013) Magnetic resonance of porous media (MRPM): a perspective. J Magn Reson 229:12–24
Stork H, Gädke A, Nestle N (2006) Single-sided and semisingle-sided NMR sensors for highly diffusive samples: application to bottled beverages. J Agric Food Chem 54:5247–5252
Straley C, Matteson A, Feng S, Schwartz LM, Kenyon WE, Banavar JR (1987) Magnetic resonance, digital image analysis, and permeability of porous media. Appl Phys Lett 51:1146–1148
Straley C, Rossini D, Vinegar H, Tutunjian P, Morriss C (1997) Core analysis by low-field NMR. Log Anal 38:84–93
Strehl S (2006) Development of strategies for improved filtering and fitting of SNMR-signals master thesis. Technical University of Berlin

Stingaciu LR, Pohlmeier A, Blümler P, Weihermüller L, Van Dusschoten D, Stapf S, Vereecken H (2009) Characterization of unsaturated porous media by high-field and low-field NMR relaxometry. Water Resour Res 45. doi:10.1029/2008WR007459
Sucre O, Casanova F, Pohlmeier A, Blümich B (2010) Low-field NMR of water in model soils. Open Magn Reson J 3:63–68
Sucre O, Pohlmeier A, Miniere A, Blümich B (2011) Low-field NMR logging sensor for measuring hydraulic parameters of model soils. J Hydrol 406:30–38
Swanson RD, Singha K, Day L, Binley A, Keating K, Haggerty R (2012) Direct geoelectrical evidence of mass transfer at the laboratory scale. Water Resour Res 48. doi:10.1029/2012WR012431
Thompson AH, Katz AJ, Krohn CE (1987) Microgeometry and transport properties of sedimentary rock. Adv Phys 36:625–694
Timur A (1969) Producible porosity and permeability of sandstones investigated through nuclear magnetic resonance principles. Long Anal 10:3−11
Tingting L, Ling W, Xin-lei S, Wenlong S, Jun L (2012) Development of a novel MRS-TEM combined instrument for improving MRS capacity in groundwater investigations 5th international meeting on magnetic resonance. Hannover
Torrey HC (1956) Bloch equations with diffusion terms. Phys Rev 104:563–565
Trushkin DV, Shushakov OA, Legchenko AV (1993) Modulation effects in non-drilling NMR in the Earth's field. Appl Magn Reson 5:399–406
Trushkin DV, Shushakov OA, Legchenko AV (1994) The potential of a noise-reducing antenna for surface NMR groundwater surveys in the Earth's magnetic field. Geophys Prospect 42:855–862
Turu V (2012) Surface NMR survey on Hansbreen Glacier, Hornsund, SW Spitsbergen. Landf Anal 21:57–74
Valckenborg R, Pel L, Kopinga K (2001) Cryoporometry and relaxometry of water in silica-gels. Magn Reson Imaging 19:489–491
Vilhelmsen TN, Behroozmand AA, Christensen S, Nielsen TH (2014) Joint inversion of aquifer test, MRS and TEM data. Water Resour Res 50(5):3956–3975
Vincent C, Descloitres M, Garambois S, Legchenko A, Guyard H, Gilbert A (2012) Detection of a subglacial lake in Glacier de Tête Rousse (Mont Blanc area, France). J Glaciol 58:866–878
Vogt C, Galvosas P, Klitzsch N, Stallmach F (2002) Self-diffusion studies of pore fluids in unconsolidated sediments by PFG NMR. J Appl Geophys 50:455–467
Vogt SJ, Stewart BD, Seymour JD, Peyton BM, Codd SL (2012) Detection of biological uranium reduction using magnetic resonance. Biotechnol Bioeng 109:877–883
Vouillamoz JM, Legchenko A, Albouy Y, Bakalowicz M, Baltassat JM, Al-Fares W (2003) Localization of saturated karst aquifer with magnetic resonance sounding and resistivity imagery. Ground Water 41:578–586
Vouillamoz JM, Favreau G, Massuel S, Boucher M, Nazoumou Y, Legchenko A (2008) Contribution of magnetic resonance sounding to aquifer characterization and recharge estimate in semiarid Niger. J Appl Geophys 64:99–108
Vouillamoz JM, Legchenko A, Nandagiri L (2011) Characterizing aquifers when using magnetic resonance sounding in a heterogeneous geomagnetic field. Near Surf Geophys 9:135–144
Walbrecker JO, Behroozmand AA (2012) Surface-NMR measurements of the longitudinal relaxation time T1 in a homogeneous sand aquifer in Skive, Denmark. J Appl Geophys 87:46–52
Walbrecker JO, Hertrich M, Green AG (2009) Accounting for relaxation processes during the pulse in surface NMR data. Geophysics 74:G27–G34
Walbrecker JO, Hertrich M, Green AG (2011a) Off-resonance effects in surface nuclear magnetic resonance. Geophysics 76:G1–G12
Walbrecker JO, Hertrich M, Lehmann-Horn JA, Green AG (2011b) Estimating the longitudinal relaxation time T1 in surface NMR. Geophysics 76:F111–F122
Walbrecker JO, Müller-Petke M, Knight R, Yaramanci U (2012) Inversion of surface-NMR T1 data: results from two field sites with reference to borehole logging 5th international meeting on magnetic resonance. Hanover
Walsh DO (2006) Multi-channel MRS instrumentation and software for enhanced noise mitigation and 2D/3D imaging. In: Proceedings of the 3rd magnetic resonance sounding international workshop, October 2006, pp 73−76
Walsh DO (2008) Multi-channel surface NMR instrumentation and software for 1D/2D groundwater investigations. J Appl Geophys 66:140–150
Walsh DO, Grunewald E, Turner P, Hinnell A, Ferre P (2011) Practical limitations and applications of short dead time surface NMR. Near Surf Geophys 9:103–111

Walsh D, Grunewald E, Zhang H, Ferre P, Hinnell A (2012) Recent advancements in NMR for characterizing the vadose zone 5th international meeting on magnetic resonance. Hannover
Walsh D, Turner P, Grunewald E, Zhang H, Butler JJ, Reboulet E, Knobbe S, Christy T, Lane JW, Johnson CD, Munday T, Fitzpatrick A (2013) A small-diameter NMR logging tool for groundwater investigations
Walsh DO, Grunewald ED, Turner P, Hinnell A, Ferre TPA (2014) Surface NMR instrumentation and methods for detecting and characterizing water in the vadose zone. Near Surf Geophys 12:271–284
Watanabe K, Wake T (2009) Measurement of unfrozen water content and relative permittivity of frozen unsaturated soil using NMR and TDR. Cold Reg Sci Technol 59:34–41
Wattanasen K, Elming S (2008) Direct and indirect methods for groundwater investigations: a case-study of MRS and VES in the southern part of Sweden. J Appl Geophys 66:104–117
Weichman PB, Lavely EM, Ritzwoller MH (2000) Theory of surface nuclear magnetic resonance with applications to geophysical imaging problems. Phys Rev E Stat Phys Plasmas Fluids Relat Interdiscip Top 62:1290–1312
Weller A, Nordsiek S, Debschütz W (2010) Estimating permeability of sandstone samples by nuclear magnetic resonance and spectral-induced polarization. Geophysics 75:E215–E226
Whittall KP, MacKay AL (1989) Quantitative interpretation of NMR relaxation data. J Magn Reson (1969) 84:134–152
Whittall KP, Bronskill MJ, Henkelman RM (1991) Investigation of analysis techniques for complicated NMR relaxation data. J Magn Reson (1969) 95:221–234
Yaramanci U, Hertrich M (2006) Magnetic resonance sounding. In: Kirsch R (ed) Groundwater geophysics: a tool for hydrogeology. Springer, Berlin
Yaramanci U, Lange G, Knödel K (1999) Surface NMR within a geophysical study of an aquifer at Haldensleben (Germany). Geophys Prospect 47:923–943
Yaramanci U, Lange G, Hertrich M (2002) Aquifer characterisation using surface NMR jointly with other geophysical techniques at the Nauen/Berlin test site. J Appl Geophys 50:47–65
Yoshikawa K, Leuschen C, Ikeda A, Harada K, Gogineni P, Hoekstra P, Hinzman L, Sawada Y, Matsuoka N (2006) Comparison of geophysical investigations for detection of massive ground ice (pingo ice). J Geophys Res E Planets 111. doi:10.1029/2005JE002573